Volume 69A
Number 4
July–Aug. 1965

Physics and Chemistry

U.S. DEPARTMENT OF COMMERCE

SECTION A

JOURNAL OF RESEARCH

NATIONAL BUREAU OF STANDARDS

Journal of Research

of the

National Bureau of Standards

A. Physics and Chemistry

July–Aug. • 1965

VOLUME • 69A

NUMBER • 4

Editor: C. W. Beckett

Associate Editors: D. D. Wagman
J. M. Richardson

Publication dates:
Feb. 1, Apr. 1, June 1, Aug. 1, Oct. 1, Dec. 1, 1965

JOURNAL OF RESEARCH

The National Bureau of Standards Journal of Research reports research and development in the fields of activity shown at right. Also included from time to time are survey articles on topics closely related to the Bureau's scientific and technical program.

The Journal is published in four separate sections as follows:

A. Physics and Chemistry

Contains papers of interest primarily to scientists working in these fields. Issued six times a year. Annual subscription: domestic, $4.00; foreign, $4.75. Single copy, 70c.

B. Mathematics and Mathematical Physics

Presents studies and compilations designed mainly for the mathematician and the theoretical physicist. Issued quarterly. Annual subscription: domestic, $2.25; foreign, $2.75. Single copy, 75c.

C. Engineering and Instrumentation

Reports research and development results of interest chiefly to the engineer and the applied scientist. Issued quarterly. Annual subscription: domestic, $2.25; foreign, $2.75. Single copy, 75c.

D. Radio Science (formerly Radio Propagation)

Published in cooperation with U.S. National Committee of URSI. Presents papers in radio propagation, communications, and radio science generally. Issued monthly. Annual subscription: domestic, $9.00; foreign, $11.50. Single copy, $1.00.

The National Bureau of Standards is a principal focal point in the Federal Government for assuring maximum application of the physical and engineering sciences to the advancement of technology in industry and commerce. Its responsibilities include development and maintenance of the national standards of measurement, and the provision of means for making measurements consistent with those standards; determination of physical constants and properties of materials; development of methods for testing materials, mechanisms, and structures, and making such tests as may be necessary, particularly for government agencies; cooperation in the establishment of standard practices for incorporation in codes and specifications; advisory service to government agencies on scientific and technical problems; invention and development of devices to serve special needs of the Government; assistance to industry, business and consumers in the development and acceptance of commercial standards and simplified trade practice recommendations; administration of programs in cooperation with United States business groups and standards organizations for the development of international standards of practice; and maintenance of a clearinghouse for the collection and dissemination of scientific, technical and engineering information.

Institute for Basic Standards. Applied Mathematics. Electricity. Metrology. Mechanics. Heat. Atomic Physics. Physical Chemistry. Laboratory Astrophysics.* Radiation Physics. Radio Standards Laboratory:* Radio Standards Physics & Radio Standards Engineering. Office of Standard Reference Data.

Institute for Materials Research. Analytical Chemistry. Polymers. Metallurgy. Inorganic Materials. Reactor Radiations. Cryogenics.* Materials Evaluation Laboratory. Office of Standard Reference Materials.

Institute for Applied Technology. Building Research. Information Technology. Performance Test Development. Electronic Instrumentation. Textile and Apparel Technology Center. Technical Analysis. Office of Weights and Measures. Office of Engineering Standards. Office of Invention and Innovation. Office of Technical Resources. Clearinghouse for Federal Scientific and Technical Information.**

Central Radio Propagation Laboratory.* Ionospheric Telecommunications, Tropospheric Telecommunications. Space Environment Forecasting. Aeronomy.

*Located at Boulder, Colo., 80301.
**Located at 5285 Port Royal Road, Springfield, Va., 22171.

U.S. DEPARTMENT OF COMMERCE
John T. Connor, Secretary

NATIONAL BUREAU OF STANDARDS
A. V. Astin, Director

Order all publications from the Superintendent of Documents
U.S. Government Printing Office, Washington, D.C., 20402

Use of funds for printing this publication approved by the Director of the Bureau of the Budget (June 19, 1961).

JOURNAL OF RESEARCH of the National Bureau of Standards—A. Physics and Chemistry
Vol. 69A, No. 4, July–August 1965

Correlation of Successive Atomic Steps in Crystals by Relaxation Mode Analysis

A. D. Franklin*

(March 5, 1965)

The relaxation mode analysis is used to compute the average value of the cosine of the angle between successive steps of an ion diffusing by a vacancy mechanism on a lattice. The technique is applicable to tracers (self-diffusion) or impurities, on any lattice. The result, given in terms of the eigenvalues and eigenvectors of a secular equation, is suitable for machine computation. Sample computations for self-diffusion on an fcc lattice illustrate the method. It is necessary, in order to do the calculations, to have a lattice of finite size, the boundary of which is chosen either totally reflecting or completely transparent to vacancies. For self-diffusion, the boundary can be centered on the vacancy, and convergence of the computed value with boundary radius is rapid. For impurity diffusion, the boundary must be centered on the impurity, and convergence is much slower.

1. Introduction

Diffusion of atoms or ions through a crystal by the vacancy or interstitialcy mechanisms proceeds not by random-walk steps but by steps that are to some extent correlated with each other [1].[1] The degree of correlation between successive steps can be represented by $\overline{\cos\theta_\alpha}$, where θ_α is the angle between the paths of the αth step and the $(\alpha+1)$th step. If the term "tracer" is defined to mean any moving particle in the crystal, then where the tracer is a host ion moving upon its own sublattice, as in self-diffusion, $\overline{\cos\theta_\alpha}$ depends only upon the geometry of the lattice. If the tracer is an impurity, $\overline{\cos\theta_\alpha}$ depends as well upon the way in which the impurity influences the motion of the vacancy in its vicinity.

A number of methods have been developed for computing $\overline{\cos\theta_\alpha}$ [2–6]. As shown by Compaan and Haven [3], the computations are very much simplified if use is made of the crystal symmetry. It is the purpose of this paper to show how maximum use can be made of the symmetry by employing the technique of relaxation mode analysis [7–10] to calculate $\overline{\cos\theta_\alpha}$. The method given is perfectly general, applying to both self-diffusion and impurity diffusion in any crystal lattice by the vacancy mechanism. With minor modification it could be applied to the interstitialcy mechanism as well. It is cast in a form that is extremely convenient for machine computation.

*Work done while on a training assignment to the Theoretical Physics Division, UKAERE, Harwell, England. Permanent address: National Bureau of Standards, Washington, D.C.

[1] Figures in brackets indicate the literature references at the end of this paper.

2. Theory

The development of the method will be given for any lattice, but the fcc lattice will be used to illustrate the development and the method itself. The problem can be visualized with the aid of figure 1. This shows the tracer at the center of a cube, with the nearest neighbor sites in the fcc lattice in the middle

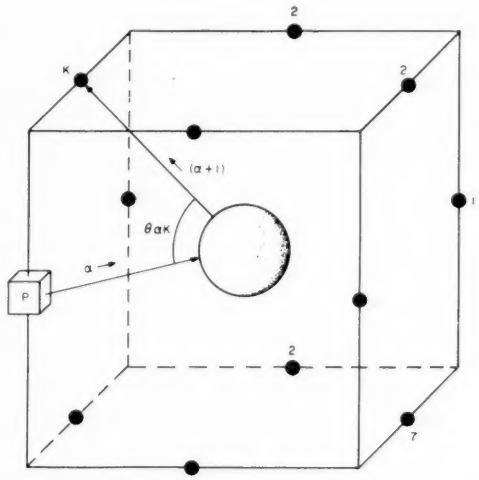

FIGURE 1. *Successive tracer steps in the fcc lattice.*

The tracer is at the center, after the αth step which has left the vacancy at P. A possible $(\alpha+1)$ step is shown, to one of the twelve nearest neighbor sites, making an angle $\theta_{\alpha k}$ with the αth step. For self-diffusion, only two kinds of nearest neighbor sites, here marked 1 and 2, need be considered. (Eq 12.)

of the edges of the cube. The tracer has just completed the step shown by the arrow labeled α, leaving the vacancy in the position labeled p. In addition, one of the twelve possibilities for the $(\alpha+1)$th step is shown. After the αth step, the vacancy will move in some fashion. It may immediately reexchange with the tracer, or it may first move directly or indirectly to one of the eleven other positions next to the tracer and then reexchange with the tracer. Or it may move away altogether and not return, so that the next step of the tracer is an exchange with a different vacancy. A different vacancy will approach the tracer in a random manner, provided the original vacancy is far away when the new one approaches, so that successive steps in which different vacancies figure are not correlated. Only steps involving the same tracer need be considered in calculating $\overline{\cos\theta_\alpha}$ for low vacancy concentrations. The problem is solved when the probability of each one of the twelve candidates for the $(\alpha+1)$th step is calculated. Although figure 1 shows only one set of lattice sites from which the vacancy can make a direct exchange with the tracer, in general there may be several, the sites in each set being crystallographically equivalent in the presence of the tracer. The solution of the problem can be found either by considering the average behavior of a large number of identical systems, or by thinking in terms of the probability of finding the vacancy on a given site for one system, as done by Bardeen and Herring [1] and others. This latter view will be taken here.

Let the probability that the vacancy occupies the kth site at a time t after the αth step be $P_k(t)$. Also, let w_{k0} be the frequency with which a vacancy occupying the kth site will change places with the tracer at the origin. Then

$$\overline{\cos\theta_\alpha}=\sum_k w_{k0}\cos\theta_{\alpha k}\int_0^\infty P_k(t)dt. \tag{1a}$$

In the relaxation mode analysis, eq (1a) can be written as a vector equation, involving vectors in site-space, to be defined below. One vector contains all of the time-dependence of the probabilities $P_k(t)$, the other the geometrical quantities $\cos\theta_{\alpha k}$. When the basis for these vectors is properly chosen, the time dependence becomes a simple series of exponential decay functions, for which the integrations are readily performed, and eq (1a) reduces to a rather simple form.

Site space may be defined by considering each site to correspond to a vector in a basis set that spans the space. Any set of scalars assigned to the sites can be represented by a vector in this space, with the scalars for coordinates. If there are N accessible lattice sites, then the site space is N-dimensional. Equation (1a) may then be written rather compactly in terms of two vectors

$$\overline{\cos\theta_\alpha}=\int_0^\infty \boldsymbol{\tau}'\cdot\mathbf{P}(t)dt, \tag{1b}$$

where the coordinates of $\boldsymbol{\tau}'$ are $w_{k0}\cos\theta_{\alpha k}$ and the coordinates of $\mathbf{P}(t)$ are the time-dependent probabilities of finding the vacancy on the various sites.

The process of identifying the proper basis can be started by dividing the lattice sites into shells, the sites in each shell being equivalent to each other under the site-group, which is the group of rotational (proper and improper) symmetry operations of the crystal about the tracer as origin. Each shell defines a subspace of the whole site-space, each subspace being orthogonal to all the subspaces defined by the other shells. A vacancy on any site in one of the first few shells, counting outward from the origin, can make a direct exchange with the tracer. For a vacancy on a site in the nth such shell, the frequency w_{n0} with which the vacancy would change places with the tracer is the same for all sites. Hence τ' can be written

$$\boldsymbol{\tau}'=\sum_n w_{n0}\boldsymbol{\tau}'_n$$

where the summation is over all shells from which direct exchange of the vacancy with the tracer can occur, and $\boldsymbol{\tau}'_n$ is the vector whose coordinates are $\cos\theta_{\alpha k}$ for all sites in the nth shell and zero for all others. Then eq (1b) becomes

$$\overline{\cos\theta_\alpha}=\sum_n w_{n0}\int_0^\infty \boldsymbol{\tau}'_n\cdot\mathbf{P}(t)dt. \tag{1c}$$

The vector $\mathbf{P}$(t). Since all of the time-dependence is contained in the vector $\mathbf{P}(t)$, only this need be considered in identifying the desired basis. The components of $\mathbf{P}(t)$, which are the probabilities $P_k(t)$, are governed by the set of N rate equations

$$\frac{dP_k}{dt}=-\sum_l^N (w_{kl}P_k-w_{lk}P_l) \tag{2}$$

where w_{kl} is the frequency with which a vacancy on the kth site will make a single, direct move to the lth site. In this problem, the tracer at the origin is treated as a sink for probability—the probability of a vacancy moving to the origin from an adjacent site is positive, but the probability of the return step is taken as zero. Equation (2) can be written in terms of the vector $\mathbf{P}(t)$ in site space:

$$\frac{d\mathbf{P}}{dt}=C\mathbf{P}(t) \tag{3}$$

where C is the matrix of the w_{kl} in eq (2). The solutions to eq (3) are

$$\mathbf{P}(t)=\sum_q\sum_s f_{qs}\mathbf{u}_{qs}\ \exp(-\lambda_{qs}t) \tag{4}$$

where the f_{qs} are defined by the initial distribution of probability, at $t=0$, the $\mathbf{u}_{qs}$ are the eigenvectors of the matrix C, and the λ_{qs} are the corresponding eigenvalues, which are also the inverse relaxation times. The subscripts q and s are defined below.

Use is made of the irreducible representations of the site-group in finding the eigenvectors and eigen-

values. The subscript s denotes the various irreducible representations, some of which may be of dimension greater than one. For these, several values of s, one for each dimension, will be required. The subscript q denotes one of the several eigenvectors (and eigenvalues) belonging to one dimension of a given irreducible representation. To each dimension of an irreducible representation of the site-group, there corresponds a subspace of the whole site-space, spanned by a set of basis vectors $\mathbf{V}_{ms}$. Each eigenvector $\mathbf{u}_{qs}$ can be written as a linear combination of the basis vectors in one set:

$$\mathbf{u}_{qs}=\sum_m a_{mqs}\mathbf{V}_{ms}. \tag{5}$$

Any basis vector $\mathbf{V}_{ms}$ lies wholly within the subspace defined by one shell of sites, although several basis vectors in a set may be drawn from the subspace of the same shell. In this case, the shell has been divided into subshells by the irreducible representation, and the indices n in eq (1c) and m in eq (5) specify the subshell.

The constants f_{qs}, etc., can be found from the initial position x_0, y_0, z_0 of the vacancy. At $t=0$

$$\mathbf{P}(0)=\sum_q\sum_s f_{qs}\mathbf{u}_{qs}$$

so that, since the eigenvectors are all mutually orthogonal, and using eq (5),

$$\mathbf{f}_{qs}=\mathbf{P}(0)\cdot\mathbf{u}_{qs}=\sum_m a_{mqs}\,\mathbf{P}(0)\cdot\mathbf{V}_{ms}.$$

But $\mathbf{P}(0)$ is a vector in site-space with unity assigned to the initial site of the vacancy, and zeros elsewhere. If this initial site is labeled the kth site in the pth subshell, then $\mathbf{P}(0)$ is orthogonal to all of the basis vectors except the $\mathbf{V}_{ps}$, and

$$f_{qs}=a_{pqs}(V_{ps})_k \tag{6}$$

where $(V_{ps})_k$ is the kth component of the basis vector $\mathbf{V}_{ps}$. Combining (4), (5), and (6) the probability vector $\mathbf{P}(t)$ may be written

$$\mathbf{P}(t)=\sum_q\sum_s\sum_m a_{pqs}a_{mqs}(V_{ps})_k\,\mathbf{V}_{ms}\exp(-\lambda_{qs}t). \tag{7}$$

To recapitulate the subscripts, s specifies the irreducible representation, or specifies one of the dimensions of a multidimensional irreducible representation, and m both denotes a basis vector within the set belonging to the sth irreducible representation and also identifies a subshell of lattice sites. Together, these subscripts cover the whole dimensionality of the site space. The subscript q indicates one of the eigenvectors belonging to the sth representation—it runs parallel with but is independent of m. The initial position of the vacancy is indicated by p (one of the set of subshells identified by the running index m) and k, which gives the site within the subshell.

The vector $\boldsymbol{\tau}'_n$. The vectors $\boldsymbol{\tau}'_n$ may also be expressed in terms of the same basis. Each set of basis vectors reflects the symmetry associated with the corresponding irreducible representation. In particular, there will always exist 3 sets, reflecting x, y, and z symmetry in real space, although they may not necessarily all correspond to the same irreducible representation as they do for cubic crystals. Any function with vector symmetry in real space will, when evaluated at each lattice site, generate a vector in site space that can be expressed as a linear combination of the basis vectors drawn only from the x, y, and z sets. For these vectors the subscript s will be replaced by x, y, or z.

Using column vectors in site space, the x, y, and z basis vectors for the nth subshell may be written

$$\mathbf{V}_{nx}=L_{nx}^{-1}\begin{bmatrix}x_{n1}\\x_{n2}\\x_{n3}\\\vdots\\\vdots\end{bmatrix},\ \text{etc.}$$

where the x_{nk}, y_{nk}, and z_{nk} are the coordinates in real space of the kth site in the nth subshell, and the L_{nx}, etc., are the normalization constants $\left(\sum_k x_{nk}^2\right)^{1/2}$, etc. Now the vectors $\boldsymbol{\tau}'_n$ in site space are generated by the function $\cos\theta_{\alpha k}$ evaluated at the lattice sites of the nth subshell in real space. This function can also be written

$$\cos\theta_{\alpha k}=-\frac{\mathbf{r}_0\cdot\mathbf{r}_k}{|\mathbf{r}_0|\,|\mathbf{r}_k|}$$

where $\mathbf{r}_0$ is the vector in real space with coordinates x_0, y_0, and z_0 from the origin to the site from which the tracer made the αth step (the initial site of the vacancy at $t=0$), and $\mathbf{r}_k$ is the vector to the kth site. Then the vector $\boldsymbol{\tau}'_n$, in site space, can be written

$$\boldsymbol{\tau}'_n=-\frac{1}{|r_0||r_n|}\{x_0L_{nx}\mathbf{V}_{nx}+y_0L_{ny}\mathbf{V}_{ny}+z_0L_{nz}\mathbf{V}_{nz}\}. \tag{8}$$

$\overline{Cos\ \theta_\alpha}$. With eq (7) for $\mathbf{P}(t)$ and eq (8) for $\boldsymbol{\tau}'_n$, the scalar product of these two vectors can be written

$$\boldsymbol{\tau}'_n\cdot\mathbf{P}(t)=-\frac{1}{|r_0||r_n|}\left\{\frac{x_0^2L_{nx}}{L_{px}}\sum_q a_{pqx}a_{nqx}\exp(-\lambda_{nx}t)\right.$$
$$+\frac{y_0^2L_{ny}}{L_{py}}\sum_q a_{pqy}a_{nqy}\exp(-\lambda_{ny}t)$$
$$\left.+\frac{z_0^2L_{nz}}{L_{pz}}\sum_q a_{pqz}a_{nqz}\exp(-\lambda_{nz}t)\right\}$$

where use has been made of the mutual orthogonality of the basis vectors $\mathbf{V}_{ms}$. When this is inserted into eq (1c) for $\overline{\cos\theta_\alpha}$ and the integration performed,

the result is

$$\overline{\cos\theta_\alpha}=\sum_n \frac{w_{n0}}{|r_0||r_n|}\left\{\frac{x_0^2 L_{nx}}{L_{px}}\sum_q \frac{a_{pqx}a_{nqx}}{\lambda_{qx}} + \frac{y_0^2 L_{ny}}{L_{py}}\sum_q \frac{a_{pqy}a_{nqy}}{\lambda_{qy}} + \frac{z_0^2 L_{nz}}{L_{pz}}\sum_q \frac{a_{pqz}a_{nqz}}{\lambda_{qz}}\right\}. \quad (9)$$

This equation is in a form that is quite suitable for machine computation. To the irreducible representations denoted by x, y, and z, there correspond secular equations which can be derived by standard methods. The qth solution to these secular equations provides values for λ_{qx}, etc. Each solution also gives a set of coefficients, a_{nqx}, etc., which are the contributions from the basis vectors $\mathbf{V}_{nx}$ to the qth eigenvector $\mathbf{u}_{qx}$. The vacancy is initially in the pth subshell with coordinates x_0, y_0, and z_0 in real space. The summation denoted by n is taken over all subshells from which the vacancy can make direct exchanges with the tracer, and by q over all solutions to each secular equation.

Equation (9) may be used to obtain the quantities appearing in Mullen's [5] correlation functions for diffusion in anisotropic lattices. Mullen showed that the important quantities are of the form

$$\epsilon_1^\alpha(A,A)=\frac{\overline{x_\alpha^A x_{\alpha+1}^A}}{(x_\alpha^A)^2}$$

$$\epsilon_1^\alpha(A,B)=\frac{\overline{x_\alpha^A x_\alpha^B}}{(x_\alpha^A)^2}$$

where x_α^A is the projection of the αth tracer step on the x-principal diffusion axis, and the superscript A indicates that this step is of the A type. The distinction between the A, B, etc., types of steps is the same as the distinction among the subshells denoted in eq (9) by the index n. From eq (9) it follows that

$$\epsilon_1^\alpha(A,B)=\frac{w_{B0}}{r_A r_B}\frac{(x^A)^2 L_{Bx}}{L_{Ax}}\sum_q \frac{a_{Aqx}a_{Bqx}}{\lambda_{qx}}$$

where A, B as subscripts denote the subshells corresponding to the A, B types of step.

Boundary conditions. In performing the computations, it is necessary to restrict the vacancy to a finite number of sites around the tracer. This imposes a boundary and necessitates a choice of boundary conditions. A convenient choice is to take a symmetrical boundary by including all sites out to a certain number of steps from the origin. Possible jumps of the vacancy to sites beyond the boundary can then be treated in one of two simple ways. If these jumps are allowed, but the return jumps are not, then the boundary is "transparent" and acts as a perfect sink. This is the boundary condition used by Compaan and Haven [3] and by Mullen [5]. Use of the transparent boundary neglects reflection of the vacancy from the region beyond the boundary. Since the path of the reflected vacancy would, to some extent, be correlated with the initial step, the transparent boundary condition underestimates the value of $\overline{\cos\theta_\alpha}$. On the other hand, the jumps through the boundary can be omitted altogether from the matrix C, in which case the boundary is totally "reflecting" and the result overestimates $\overline{\cos\theta_\alpha}$. If the computations are performed for both conditions, then an upper and a lower limit are obtained for $\overline{\cos\theta_\alpha}$.

3. Self-Diffusion in the FCC Lattice

The method can be illustrated by calculating $\overline{\cos\theta_\alpha}$ for self-diffusion on a fcc lattice. Compaan and Haven [3], using a somewhat different technique to solve essentially the same equations, have given a value for $\overline{\cos\theta_\alpha}$ of -0.12268 for this case, to which the results of the present method may be compared.

For the cubic lattices, the x, y, and z irreducible representations form a degenerate set, with the same secular equations. For illustrative purposes, we may consider the particular case of the fcc lattice, and restrict direct exchanges to the nearest neighbor shell only, without subshells. Then $p=n=1$, $r_0=r_n=(x_0^2+y_0^2+z_0^2)^{1/2}$, and eq (9) reduces to the very simple form

$$\overline{\cos\theta_\alpha}=w_{10}\sum_q \frac{a_{1q}^2}{\lambda_q}. \quad (10)$$

Furthermore, a simple prescription can be given for the secular equation for the x, y, z irreducible representation (T_{1u} in the notation of Eyring, Walter, and Kimball [12]) in the fcc lattice. This equation is

$$C'\mathbf{u}_q=\lambda_q\mathbf{u}_q$$

where C' is a matrix whose entries are:

c'_{ii} = sum of the jump frequencies of all possible jumps of the vacancy out of a site included in the ith basis vector, into sites not included in the same vector.

$c'_{ij}=-g_{ij}(d_j/d_i)^{1/2}w_{ij}$,
where g_{ij} is the number of sites included in the ith basis vector from which jumps into any site included in the jth basis vector are made; d_j and d_i are the number of nonzero entries in the jth and ith basis vectors, respectively; and w_{ij} is the jump frequency for jumps of the vacancy from a site in the ith basis vector to one in the jth basis vector.

In performing the calculation, the boundary is chosen, thus limiting the number of lattice sites considered explicitly and therefore the dimension of the matrix C'. The prescription given above is used to write down the matrix, and its eigenvalues and eigenvectors found by numerical computation. The eigenvalues λ_q and the coefficients a_{1q} of the first basis vector (corresponding to the sites that are nearest neighbors to the tracer) in the eigenvectors are inserted into eq (10) to give $\overline{\cos\theta_\alpha}$.

There is a convergence problem in these calculations, arising from the presence of a boundary of

finite radius. For self-diffusion, there is no interaction between the tracer and the vacancy to bind them together, so that the vacancy may be expected to make long excursions away from the tracer, and the presence of the boundary may influence the computed value of $\overline{\cos\theta_\alpha}$ even for a boundary quite far from the origin. If the boundary be made spherical, an estimate of the rate of convergence of the calculated value of $\overline{\cos\theta_\alpha}$ as the radius R of the boundary increases may be made. For this estimate, use is made of the analogy pointed out by Ham [13] between the solutions to a steady-state diffusion problem and the solutions to an electrostatic problem of similar geometry. In the form given by Compaan and Haven [13] eq (2) can be integrated with respect to time from 0 to ∞ and written

$$\int_0^\infty \frac{dP_p}{dt}\,dt=1=w\sum_i (V_i-V_p);$$

$$\int_0^\infty \frac{dP_j}{dt}\,dt=0=w\sum_i (V_i-V_j), \quad j\neq p \qquad (11)$$

where w is the single jump frequency needed in the self-diffusion case, the subscript p denotes the initial position of the vacancy, and

$$V_i=\int_0^\infty P_i(t)dt.$$

Compaan and Haven noted that eqs (11) are identical to the equations governing current flow in a resistor network. However, these equations apply equally to the charge and potential distribution in a capacitor network. Let the lattice sites be connected by capacitors of capacitance w, and let the potential at the ith site be V_i. Then if a unit charge is placed on the pth site, and zero charge on all others, the potentials on the lattice sites will conform to eqs (11). For the fcc lattice, as shown by Compaan and Haven, $\overline{\cos\theta_\alpha}$ is given by

$$\overline{\cos\theta_\alpha}=-w(V_1+2V_2) \qquad (12)$$

where V_1 and V_2 are the potentials at the sites marked 1 and 2 in figure 1, when a positive unit charge is at site p and a negative one at site 1.

An estimate of these potentials may be made when the radius of the boundary is large enough to allow replacing the discrete network by a homogeneous dielectric sphere, with a radius R and with a charge $-q$ placed at $\sqrt{2a}$ and another one q placed at $-\sqrt{2a}$, where a is the cation-anion separation (fig. 2). The origin is fixed at zero potential, and the boundary also taken as fixed at zero potential to reproduce the transparent boundary condition described above. The problem is then that of the potential due to fixed charges within a conducting spherical shell held at zero potential. As shown by Abraham and Becker [14], the same potential would be produced by image charges $\pm Q=\pm qR/\sqrt{2a}$, located at distances $\pm R^2/\sqrt{2a}$ from the origin as shown in figure 2. If $R\gg a$, then the potential at an arbitrary point within the sphere specified by spherical coordinates r and ϕ is

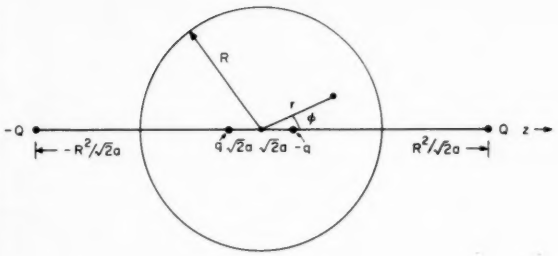

FIGURE 2. *Electrostatic model of the transparent boundary.*

R is the radius of the boundary; r and ϕ define the position of an arbitrary point within the boundary. Real charges $-q$ and q are placed at the initial vacancy site and the inversion-related position, a distance $\sqrt{2a}$ from the origin. Image charges Q and $-Q$ are placed on the Z axis $\pm R^2/\sqrt{2a}$ from the origin.

$$V=V_0+\frac{q}{R}\left\{\frac{4a^2}{R^2}\cos\phi+\frac{8a^6}{R^6}(5\cos^3\phi-3\cos\phi)\ldots\right\} \qquad (13)$$

in which the first term V_0 is due to the real charges within the sphere, and the second term is due to the image charges, and therefore represents the contribution of the boundary.

When potentials at sites 1 and 2 are evaluated using eq (13) and inserted in eq (12), the result is

$$\overline{\cos\theta_\alpha}=\overline{\cos\theta_{\alpha 0}}+\text{constant}\times\left[\left(\frac{a}{R}\right)^3-\frac{1}{4}\left(\frac{a}{R}\right)^7\ldots\right] \qquad (14)$$

This equation may be used as an extrapolation formula to obtain a value for $\overline{\cos\theta_{\alpha 0}}$ from the values of $\overline{\cos\theta_\alpha}$ computed for finite boundaries with eq (10). It suggests that the computed value, for large enough values of the radius R of the boundary sphere, should approach the true value as $1/R^3$. Values of $\overline{\cos\theta_\alpha}$, computed for both reflecting and transparent boundary, are plotted in figure 3 against $(R/a)^{-3}$, where R has been identified with the distance from the origin to the closest sites from which return jumps were not allowed (transparent boundary) or to which forward jumps were not allowed (reflecting boundary). The values for the transparent boundary show the expected R^{-3} behavior for large R. If eq (14) is used as an extrapolation formula, with arbitrary coefficients, the value of -0.12266 is obtained for $\overline{\cos\theta_{\alpha 0}}$, in essential agreement with the value computed by Compaan and Haven [3].

This R^{-3} convergence is independent of the specific lattice considered, and arises simply from the fact that the tracer position after the αth step is taken as

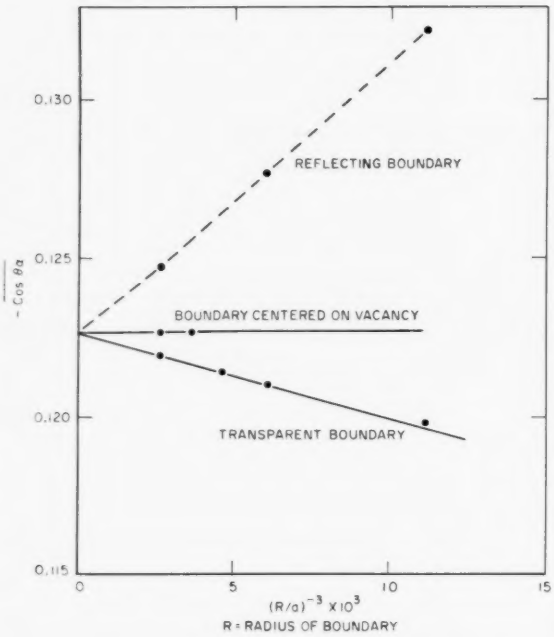

FIGURE 3. *Dependence of* $\overline{\cos\theta_\alpha}$ *upon* $(R/a)^{-3}$, *for both transparent and reflecting boundaries centered on the tracer, and for a transparent boundary centered on the vacancy.*

The solid line for the transparent boundary was drawn using eq (14) as an extrapolation formula, plotting only the term in R^{-3}.

the origin, around which a symmetrical boundary is placed. For impurity diffusion in which the impurity ion and the vacancy are bound together, the excursions of the vacancy out to the boundary will be less likely than in the case of self-diffusion, with no binding. Hence the convergence for impurity diffusion should be more rapid than given by R^{-3}.

It is possible to achieve more rapid convergence in the special case of self-diffusion by placing the position of the vacancy after the αth step at the origin, as done by Compaan and Haven [3] and by Mullen [5], although this cannot be done for impurity diffusion. For self-diffusion the tracer is exactly like all other atoms or ions in the crystal. Compaan and Haven showed that for crystals in which the tracer site is a center of symmetry or has a mirror plane, a two-fold, or a three-fold axis of rotation perpendicular to the direction of the αth step, the trajectories of the vacancy that cross the tracer need not be terminated at the tracer. In the electrostatic model, this is equivalent to removing the condition that the tracer site be held at zero potential, and in the language of the relaxation mode analysis, it is equivalent to including jumps of the vacancy out of, as well as into, the tracer site, so that the tracer no longer is a sink for the probability. Under these circumstances, the problem has the symmetry of the site-group at the initial position of the vacancy, and this position can be taken as the origin, with the boundary distributed symmetrically about it, rather than about the tracer. In the electrostatic model for the fcc lattice, the spherical boundary can be taken about the initial position of the vacancy as a center, and only at this point is there any charge within the sphere. Such a boundary simply adds a constant to the potential everywhere so that $\overline{\cos\theta_\alpha}$, which depends only upon differences in potential, is not affected by the presence of the boundary in the continuum approximation. For a real lattice, there will be a dependence of $\overline{\cos\theta_\alpha}$ for boundary radii too small to allow a continuum approximation.

The rapid convergence that results when the boundary can be centered on the vacancy can be illustrated by direct calculation. In the relaxation mode analysis of this case, the initial distribution of probability is spherically symmetric, and the only modes excited will be the spherically symmetric ones, the A_{1g} for the fcc lattice. Equation (10) will be replaced by

$$\overline{\cos\theta_\alpha} = w \sum_q \frac{a_{1q}}{\lambda_q \sqrt{n_1}} \left\{ \frac{a_{1q}}{\sqrt{n_1}} + \frac{2a_{2q}}{\sqrt{n_2}} - \frac{2a_{4q}}{\sqrt{n_4}} - \frac{a_{5q}}{\sqrt{n_5}} \right\}$$

where a_{iq} are the coefficients of the ith basis vector in the qth eigenvector of the A_{1g} irreducible representation, λ_q are the corresponding eigenvalues, and n_i is the number of sites in the ith shell (there are no subshells for the spherically symmetric modes). Using this equation, and setting a transparent boundary at $R/a=\sqrt{42}$ and $R/a=\sqrt{52}$, we obtained -0.12268 for $\overline{\cos\theta_\alpha}$ in both cases (fig. 3). The value had converged even for the smaller boundary, and agrees exactly with Compaan and Haven's value.

It should be noted that the boundary used in this calculation was not exactly identical to that used either by Compaan and Haven [3] or by Mullen [5]. In the present calculations, the boundary was taken as spherical. The *distance* from the origin to any point on the boundary was the same in all directions, but the number of steps required for the vacancy to reach the boundary was not the same. If, as done by Compaan and Haven, and Mullen, the boundary was taken as a certain number of steps from the origin in all directions, the secular equation could have been somewhat smaller in size and the problem somewhat simpler, without affecting the convergence significantly.

The present method of calculating $\overline{\cos\theta_\alpha}$, using the relaxation mode analysis, is basically similar to Mullen's [5] method. Equation (4) of the present paper, giving the probability vector $P(t)$, can be made equivalent to Mullen's eq (10) by an integration over t from zero to infinity and multiplication of each component by the sum of the frequencies of all jumps out of the corresponding site. Mullen treats only the case of self-diffusion, with the boundary centered on the vacancy. Simplification of the equations is brought about by introducing only sites not symmetry-related to each other under the crystallographic point group. This is equivalent to

the choice of the A_{1g} mode as described above. The two treatments lead to matrices of the same dimensionality. In Mullen's formulation, it is necessary to invert the matrix; here, the eigenvalues and eigenvectors must be calculated.

For impurity diffusion, the relaxation mode analysis simplifies the equations by expressing the probability vector $\mathbf{P}(t)$ as a sum of eigenvectors of the matrix C, each multiplied by its relaxation function. Equation (1b) then selects only those eigenvectors not orthogonal to $\boldsymbol{\tau}'$. The same procedure could be applied to Mullen's eq (10). The initial probability distribution, $\boldsymbol{\tau}(0)$, would be expressed as a sum, each term of which would be equivalent to an eigenvector of Mullen's T matrix. The choice of the eigenvectors as a basis would reduce T to its irreducible representations, of which only the vector representation would have to be kept, thus achieving the same reduction in the size of the matrix to be handled as obtained in the relaxation mode analysis. In addition, the boundary would have to be centered on the site of the impurity, since this is the only center of symmetry in the presence of the impurity.

4. Summary

Correlation between successive steps of an impurity or tracer as it diffuses through a crystal by the vacancy mechanism can often be expressed in terms of $\overline{\cos\theta_\alpha}$, the average of the value of the cosine of the angle between the αth and $(\alpha+1)$th steps. $\overline{\cos\theta_\alpha}$ can be computed for any lattice using the methods of relaxation mode analysis, resulting in eq (9) of this paper, and reducing the problem to a form well suited to machine computation. A symmetrical boundary is taken about the impurity or tracer. When the boundary is transparent, so that the vacancy does not return once it has penetrated the boundary, the computation gives a lower limit to the magnitude of $\overline{\cos\theta_\alpha}$. An upper limit is produced when the boundary is totally reflecting. The computed values of $\overline{\cos\theta_\alpha}$ for self-diffusion with the transparent boundary converge as $1/R^3$, where R is the distance from the origin to sites just beyond the boundary. For impurity diffusion in which the vacancy and impurity are attracted to each other, the convergence should be somewhat more rapid. The method has been illustrated by computing $\overline{\cos\theta_\alpha}$ for self-diffusion in the fcc lattice. The $1/R^3$ convergence was demonstrated, and an extrapolated value of 0.12266 obtained, in essential agreement with the value of 0.12268 given by Compaan and Haven [3]. For the special case of self-diffusion, Compaan and Haven showed that for sufficiently symmetric crystals, the origin can be placed at the initial position of the vacancy and a symmetrical boundary placed around it, producing much more rapid convergence. Computations for this model were also made for the fcc lattice, with two sizes of boundary, and both gave values in exact agreement with Compaan and Haven's value.

The author is indebted to A. B. Lidiard for the original suggestion that the relaxation mode analysis could be used to calculate $\overline{\cos\theta_\alpha}$, and to R. C. F. McLatchie for performing the computations.

5. References

[1] J. Bardeen and C. Herring in Imperfections in Nearly Perfect Crystals p. 261 (John Wiley & Sons, New York, 1952).
[2] A. D. LeClaire and A. B. Lidiard, Phil. Mag **1,** 518 (1956).
[3] K. Compaan and Y. Haven, Trans. Far. Soc. **52,** 786 (1956); **54,** 1498 (1958).
[4] J. R. Manning, Phys. Rev. **116,** 819 (1959); **128,** 2169 (1962).
[5] J. G. Mullen, Phys. Rev. **124,** 1723 (1961).
[6] H. B. Huntington and P. B. Ghate, Phys. Rev. Letters **8,** 421 (1962).
[7] Y. Haven and J. H. Van Santen, J. Chem. Phys. **22,** 1146 (1954); Nuovo Cimento **7,** 605 (1958).
[8] J. B. Wachtman, Jr., Phys. Rev. **131,** 517 (1963)
[9] A. D. Franklin, J. Res. NBS **67A,** (Phys. and Chem.) No. 4, 291 (1963).
[10] S. Bhagavantam and P. V. Pantulu, Proc. Indian Acad. Sci. **58,** 183 (1963).
[11] A. D. Franklin, A. Shorb, and J. B. Wachtman, Jr., J. Res. NBS **68A,** (Phys. and Chem.) No. 5, 425 (1964).
[12] H. Eyring, J. Walter, and G. E. Kimball, Quantum Chemistry (John Wiley & Sons, New York, 1944).
[13] F. S. Ham, J. Phys. Chem. Solids **6,** 335 (1958).
[14] M. Abraham and R. Becker, The Classical Theory of Electricity and Magnetism, p. 68, translated into English by J. Dougall (Blackie and Son, Ltd., Glasgow, 1937).

(Paper 69A4–350)

JOURNAL OF RESEARCH of the National Bureau of Standards—A. Physics and Chemistry
Vol. 69A, No. 4, July–August 1965

Reduction of Crystallographic Point Groups to Subgroups by Homogeneous Stress

H. S. Peiser and J. B. Wachtman, Jr.

(February 23, 1965)

It is assumed that the symmetry operations possessed by a homogeneously stressed crystal will be those common to the crystal and to the stress. Application of stress either leaves a point group unaltered or lowers it to a subgroup. Any stress-induced minimum step of symmetry lowering can be caused by unaxial stress but three of the possible stress-induced compound steps of symmetry lowering require biaxial stress. The uniaxial or biaxial stress required for any stress-induced symmetry lowering is tabulated and stereograms are given for each of the minimum steps showing the relation of the remaining symmetry operations to the initial symmetry and showing the splitting of a set of initially equivalent general directions into inequivalent subsets. These stereograms provide a direct representation of the splitting of a general position in a crystal into inequivalent subsets for the symmorphic space groups and the latter are listed; the effect of glide planes and screw axes must be considered in the remaining space groups yet the stereograms still provide the correct pattern of splitting. Uses of the stereograms, for instance, to obtain the splitting of a special position, are described.

1. Introduction

The response of crystals to stress has been studied for many years; the conditions on elastic constants and piezoelectric constants imposed by crystal symmetry are given, for example, by Nye [1].[1] He has also discussed second order effects including those arising when a crystal is stressed and simultaneously subjected to a second influence such as a beam of light. The treatment proceeds by considering that the stressed crystal has only the symmetry elements common to the stress and to the unstressed crystal; the electro-optical coefficients permitted by symmetry are those appropriate to the point group of the stressed crystal. If this is of lower order than the point group of the unstressed crystal, finite values are permitted for some of the electro-optical coefficients which were previously zero. In an actual experiment it is easier to apply a uniaxial stress than one which is biaxial or triaxial. The subgroups which can be reached by any homogeneous stress have been classified [2] and organized into a successive subgroup scheme [3]; we shall show by tabulating appropriate tensile stresses that all but three of these symmetry reductions can be induced by uniaxial stress. The other three symmetry reductions require biaxial stress.

The effect of stress on symmetry restrictions of a tensor property can thus be determined if the tensor property is one previously classified in terms of symmetry of unstressed crystals. There are, however, other properties which are influenced by the molecular symmetry of the crystal and which reflect only the state of a particular set of atoms of one type rather than an average over all atoms of this type; such properties may require more detailed consideration of the symmetry lowering caused by stress. For example, the excitation spectra of donors in a semiconductor such as silicon depend on the site symmetry of the donor. In the case of silicon the usual donor atoms occupy substitutional sites with the full point-group symmetry of the crystal; application of homogeneous stress changes the symmetry of all sites equally and leads to a single pattern of splitting of excitation spectra for a given stress [4]. The point symmetry of initially equivalent sites in a crystal may, however, change unequally under a given stress and more complex patterns of splitting of spectra should then occur. For example, sites with symmetry m in a crystal of symmetry $\bar{3}$m can be affected by uniaxial stress so that two out of every three sites lose all symmetry while the third retains the symmetry m. The possibility of such unequal symmetry lowering and the circumstances under which it should occur can be seen from stereograms showing the original symmetry operations and the symmetry retained under stress. These considerations of unequal symmetry lowering should also apply to the observation of magnetic resonance in crystals under homogeneous stress [5]. A minimum step of stress-induced lowering of symmetry has previously been defined for space groups as one which leaves no stress-induced subgroup of the initial group which is also a supergroup of the final group and which is distinct from both [6]. The same definition is taken for point groups. One might suppose that such a minimum step might leave a distinct subgroup not reachable by stress which is a distinct supergroup of the final group. Detailed examination shows that no such crystallographic point groups occur. A complete set of stereograms for all crystal symmetries and all possible minimum steps of symmetry lowering is given here.

[1] Figures in brackets indicate the literature references at the end of this paper.

772-343—65——2

These stereograms also show the inequivalences introduced into a set of general sites; the results for special sites follow from these. Any nonminimum step of symmetry lowering by stress can be analyzed in terms of successive minimum steps.

The stereograms and stress tables given here should also be useful in other fields such as internal friction and the morphology of crystals [3, 7, 8, 9].

The splitting of a set of sites in a crystal into inequivalent subsets under stress has also been treated in the context of space groups [10], the relation of the present point-group considerations to the space-group treatment will be covered in the discussion.

2. Description of Stereograms

Stereograms representing each of the 32 crystallographic point groups and their conventional symbols are given in the *International Tables for X-ray Crystallography* [11]. These tables also list all of the subgroups of each point group; only certain of these subgroups can be reached by the action of homogeneous stress. They have been listed [3] and a systematic method of deriving this list is now presented in the appendix. It is useful to show the symmetry operations retained in a stress-induced subgroup and the original symmetry operations on the same stereogram. The latter can be shown by the conventional symbols used by the International Tables [11] but the former require new symbols. Both the conventional symbols and the new symbols are illustrated and defined in figure 1.

The stereograms are also shown in figure 1; those for centrosymmetric point groups are given first, beginning with those of highest order. The crystallographic axes are not marked, but the z-axis of the initial point group is taken to be at the center (north pole) of the stereogram. For all crystal systems (other than triclinic for which no stereogram is shown because no proper stress-induced subgroup exists) the angle between z and y is 90°. Therefore, in all cases the y-axis must fall on the primitive (equator) so according to accepted convention we have chosen the horizontal axis with positive y towards the right.

In some stereograms a second heading, inclined at an angle to the first, is given. When using these, as explained subsequently, "horizontal" is with respect to the heading used. A given point group sometimes occurs in more than one orientation as a stress-induced subgroup of an initial point group. Alternative settings may be equivalent (i.e., one is generated from another by symmetry operations of the initial point group) or inequivalent. A second, nonequivalent setting is indicated by a second heading placed at an angle so that positive y of the initial group is to the right when the heading is horizontal. Such inequivalent settings occur for 6 of the 37 minimum steps of stress-induced symmetry lowering: 4/mmm to mmm, mmm to 2/m, 4mm to mm2, 422 to 222, mm2 to m, and 222 to 2. In the case of 4/mmm to mmm the two headings are written as $4/\overset{|\ |\ |}{\text{mmm}} \rightarrow \overset{\downarrow\ \downarrow\ \downarrow}{\text{mmm}}$ to indicate that the

FIGURE 1.

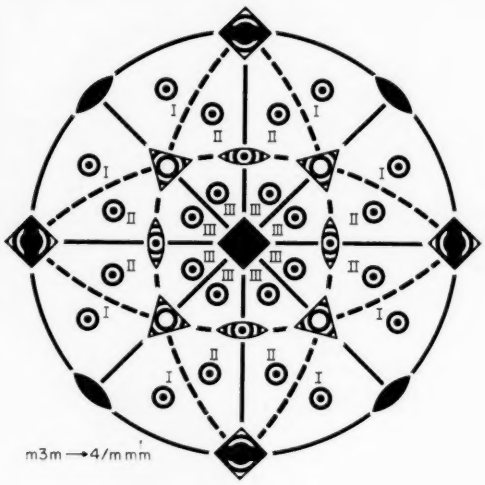

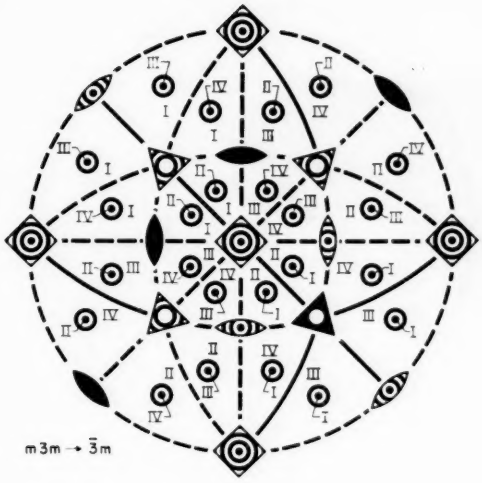

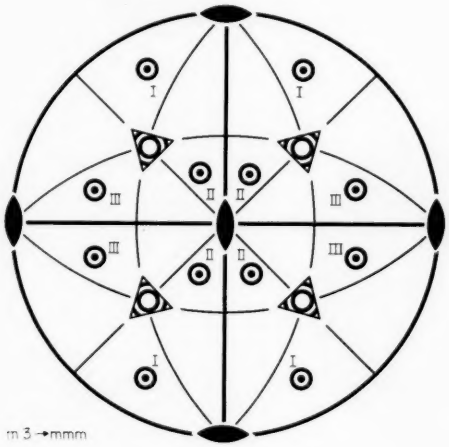

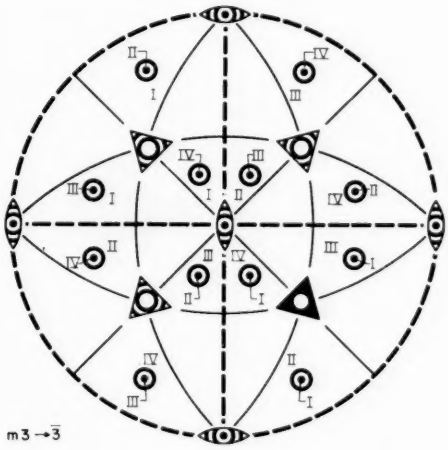

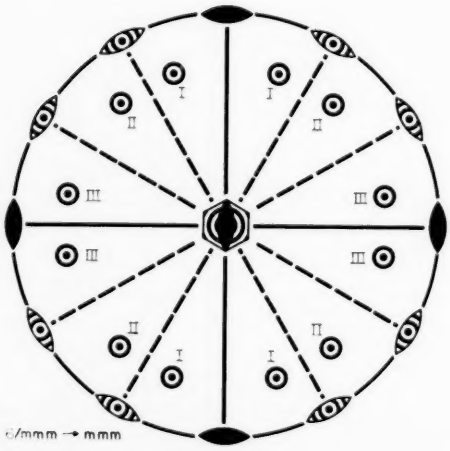

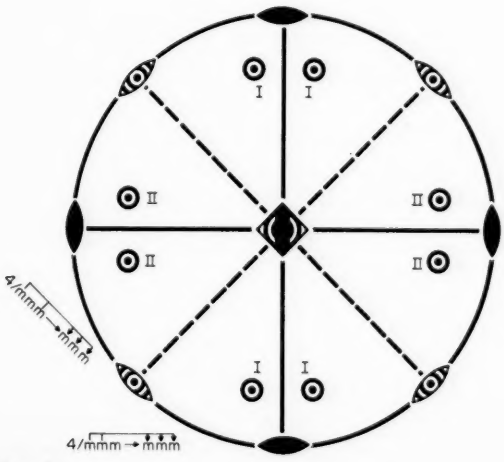

FIGURE 1—*Continued*

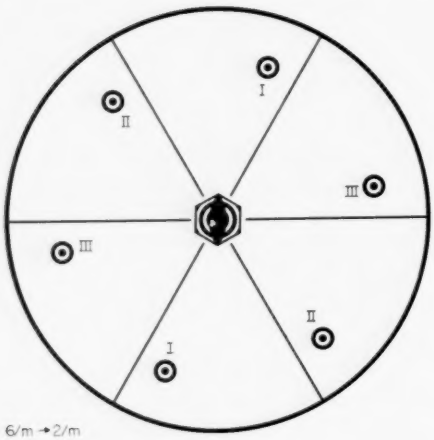

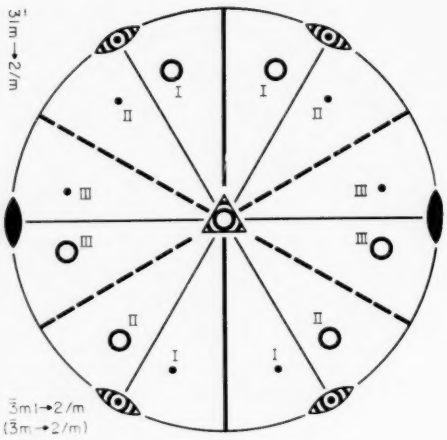

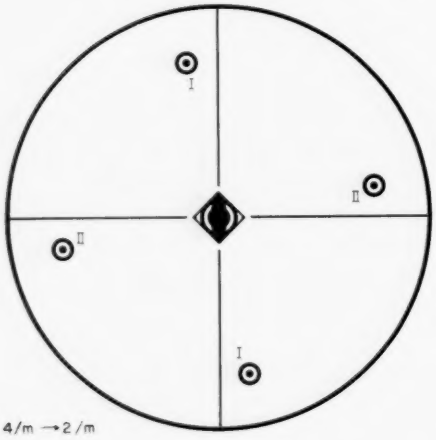

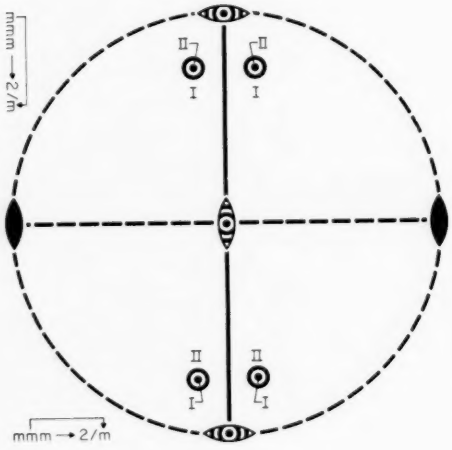

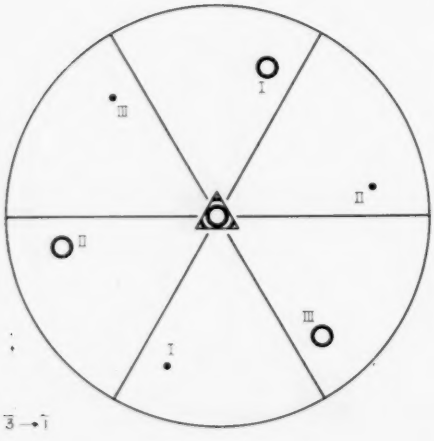

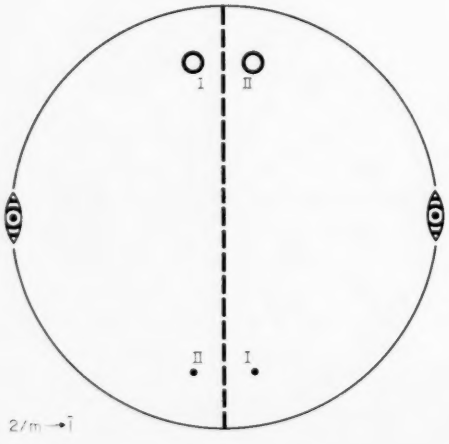

FIGURE 1—*Continued*

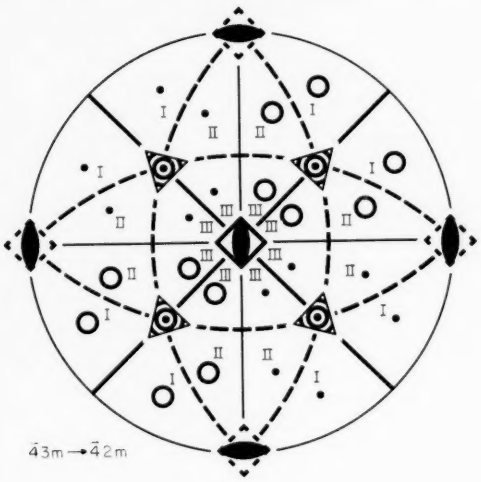

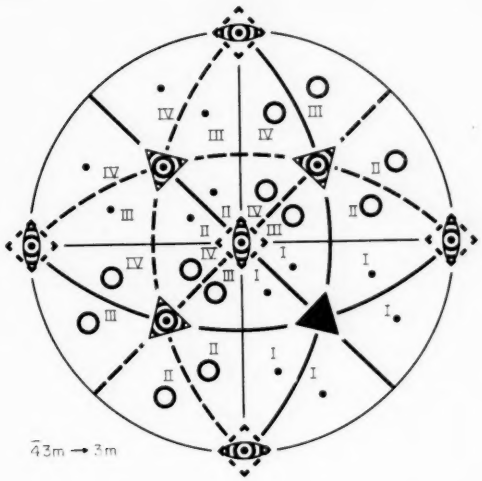

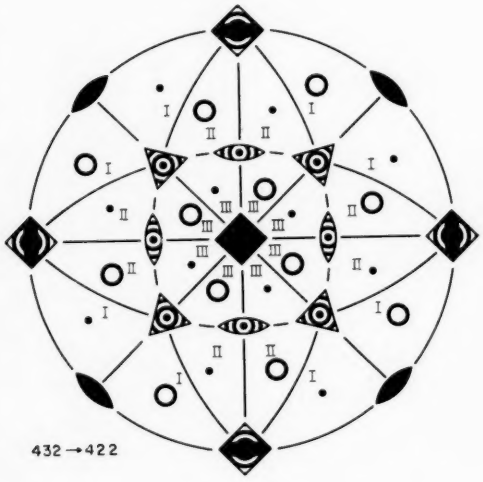

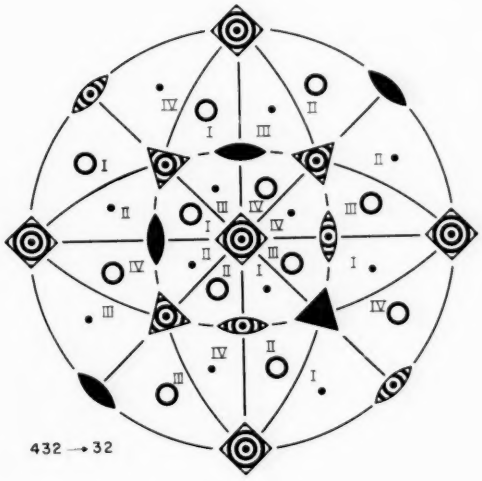

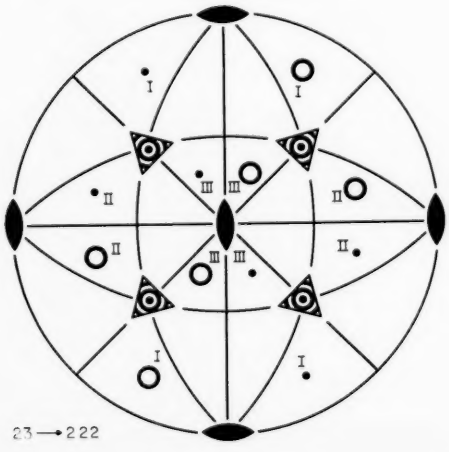

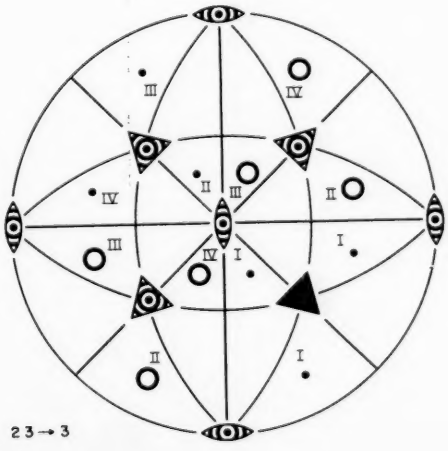

FIGURE 1—*Continued*

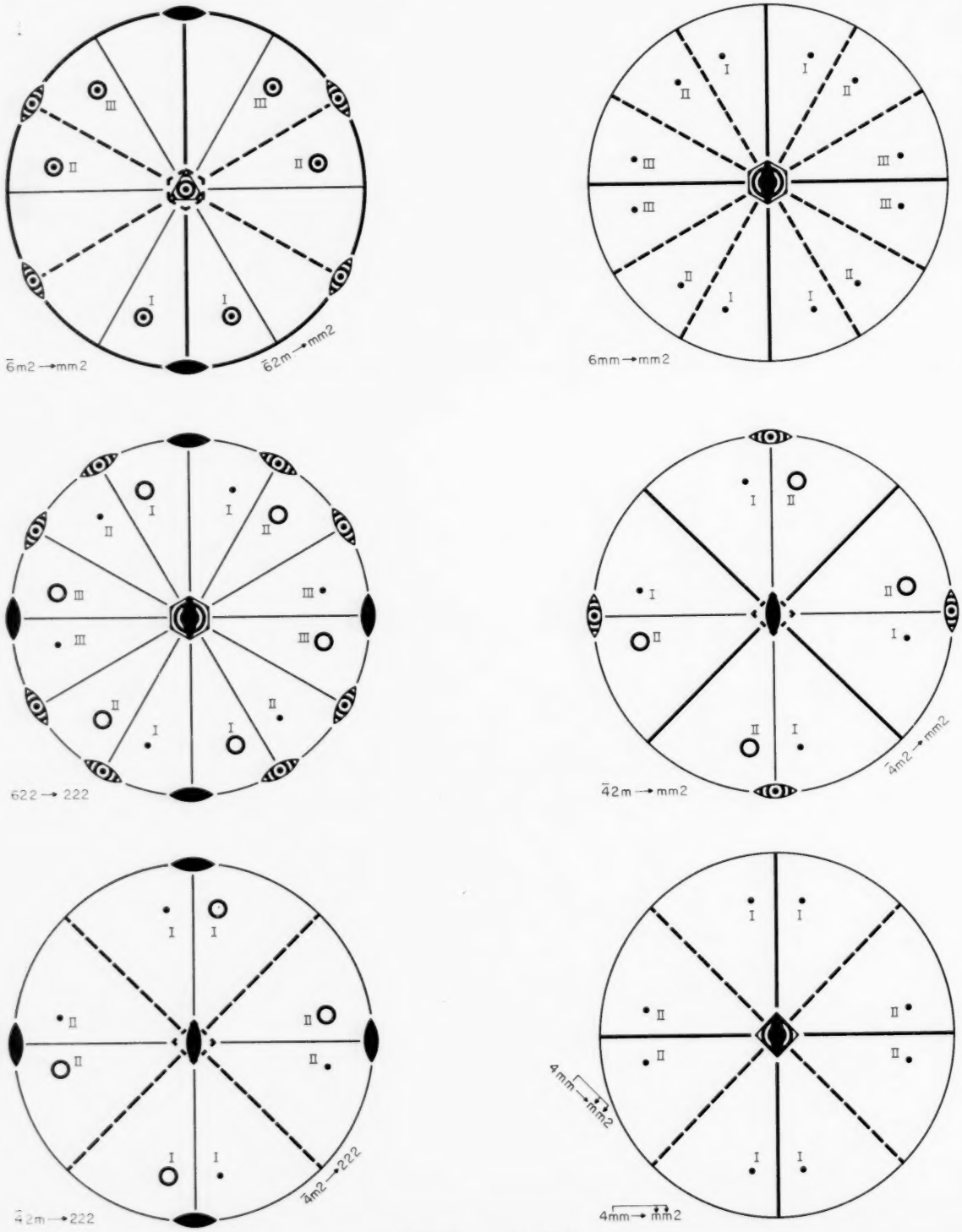

FIGURE 1—*Continued*

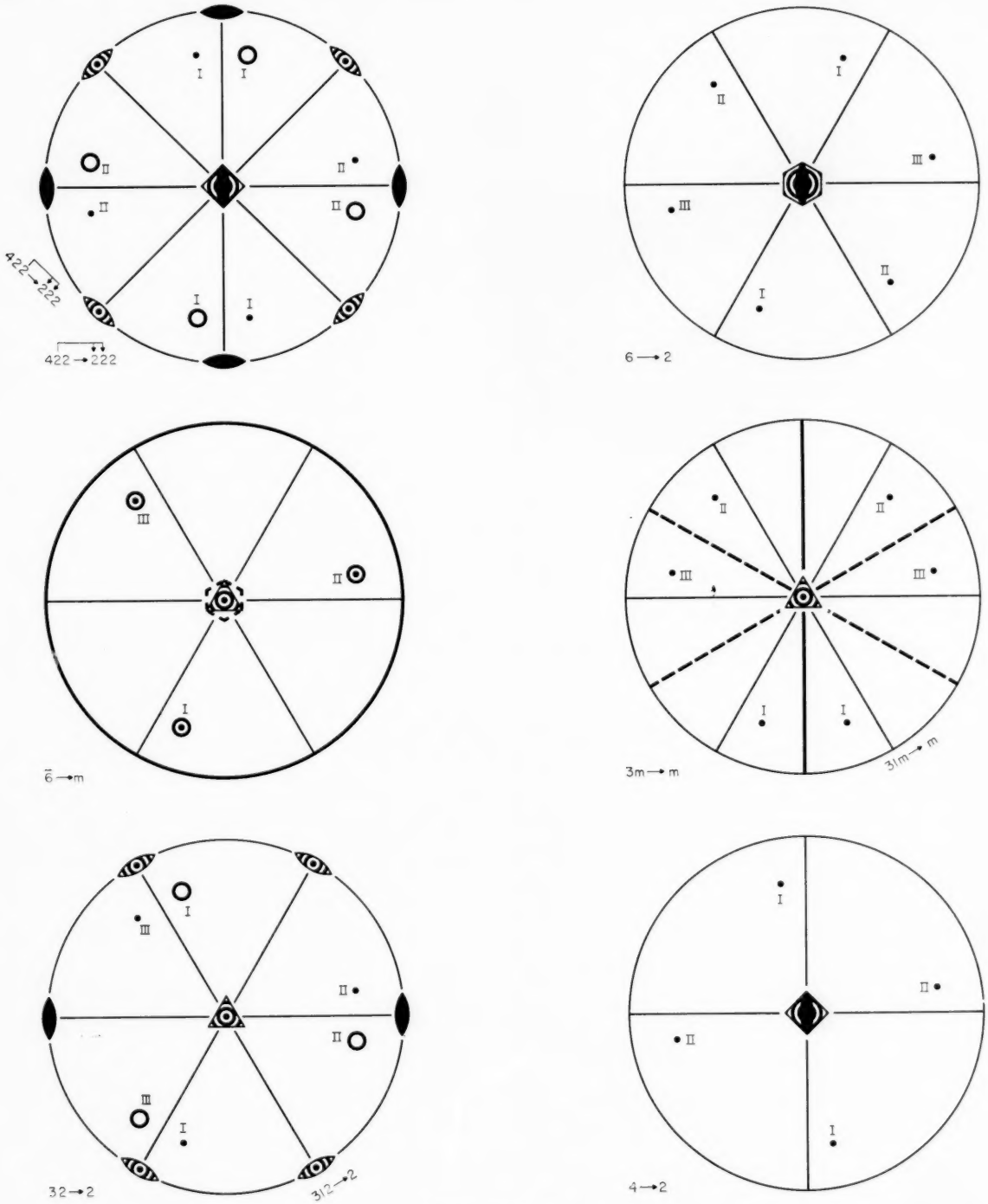

FIGURE 1—*Continued*

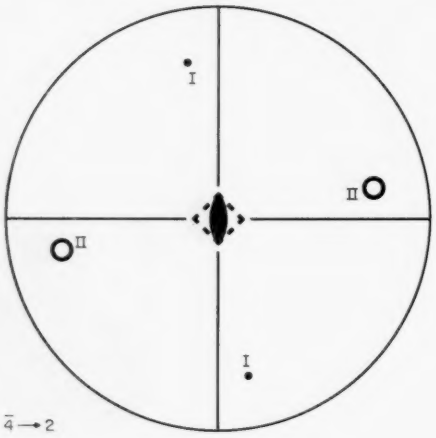

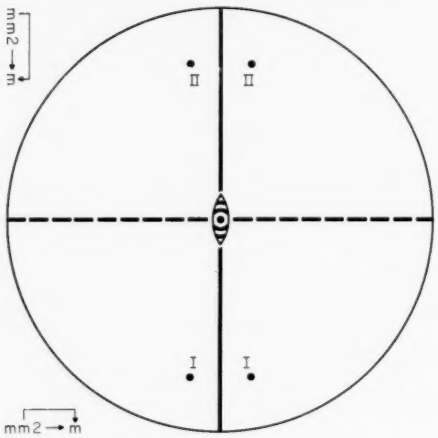

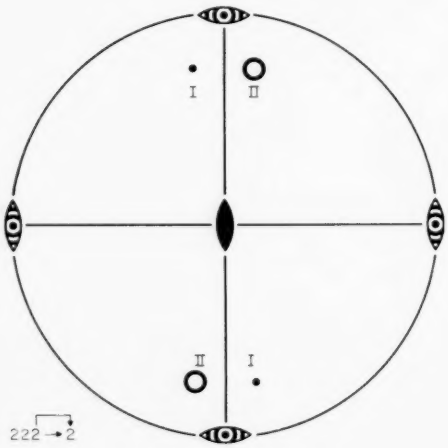

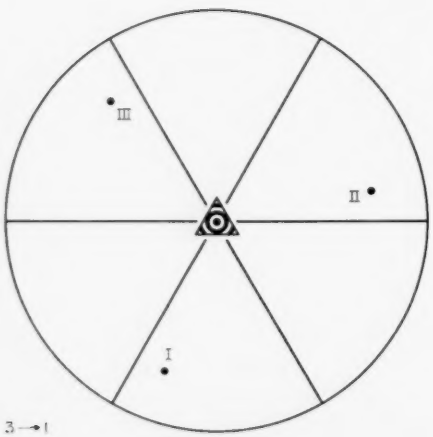

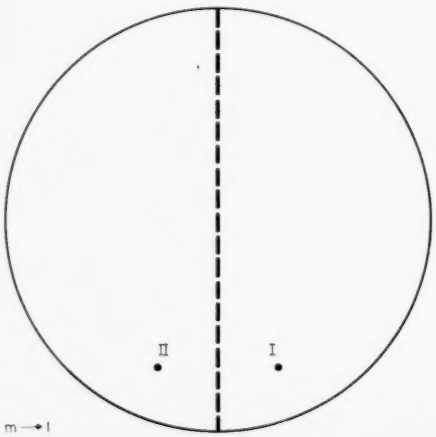

FIGURE 1—*Continued*

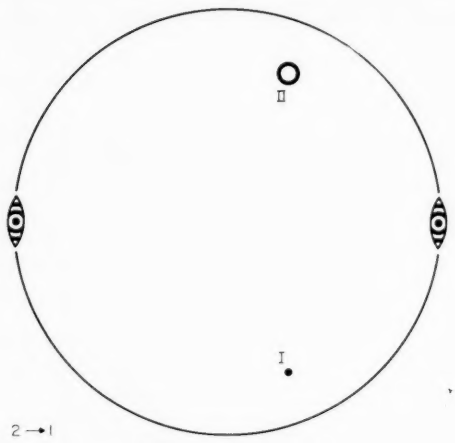

FIGURE 1—*Continued*

mirror planes perpendicular to z, x, and y are preserved and as $4/\overset{|}{m}\overset{|}{m}\overset{|}{m} \rightarrow \overset{\downarrow}{m}\overset{\downarrow}{m}\overset{\downarrow}{m}$ to indicate that the mirror planes perpendicular to z, $[1\bar{1}0]$, and $[110]$ are preserved. Similar headings are given for the other cases but this scheme does not permit three labels for the three inequivalent ways for mmm to 2/m and 222 to 2.

Two headings are given on some of the other stereograms even though the subgroup does not occur in inequivalent ways. This is done for $\bar{3}$m to 2/m, $\bar{6}$m2 to mm2, $\bar{4}2$m to mm2, $\bar{4}2$m to 222, 32 to 2, and 3m to m to draw attention to the fact that an alternative setting is used sometimes for diverse reasons such as in describing crystals which in the morphologically conventional setting would have cells with a larger than minimum number of lattice points per cell.

A general direction (one not carried into itself by any of the operations of a point group under consideration) will give rise to a set of $n(\mathrm{PG}_0)$ equivalent directions where $n(\mathrm{PG}_0)$ is the order of the initial point group PG_0. This set splits into $\dfrac{n(\mathrm{PG}_0)}{n(\mathrm{PG}_1)}$ subsets of $n(\mathrm{PG}_1)$ directions each, when the original point group is lowered to a subgroup PG_1 of order $n(\mathrm{PG}_1)$. Each stereogram shows a set of $n(\mathrm{PG}_0)$ general directions for the initial point group; directions intersecting the reference sphere (from which the stereogram is derived) on the upper hemisphere (projector through the south pole) are represented by points and those intersecting the lower hemisphere (projector through the north pole) by circles. The directions which belong to the same subset under the operations of the subgroup for the stereogram are given the same Roman number.

When directions are shown in pairs (upper and lower hemispheres) one Roman numeral indicates that those two directions belong to the same subset. Otherwise, two separate Roman numerals are given; the one on the upper hemisphere has a connecting line to the center.

3. Description of Stress Tables

The symmetry elements of uniaxial stress are those of an ellipsoid of revolution [3,5]; i.e., an ∞-fold axis perpendicular to a mirror plane with every plane containing the ∞-fold axis also being a mirror plane. Tables 1 and 2 list the orientation of the ∞-fold axis suitable for each of the minimum steps of symmetry lowering. Each of the entries in the tables can be checked by superposing the above named symmetry elements on the stereogram of the initial point group with the ∞-fold axis oriented as specified. The tables also list appropriate orientations for all but three of the compound steps of symmetry lowering: m3m to mmm in one setting, $\bar{4}3$m to 222, and 432 to 222 in one setting; none of these three can be accomplished by uniaxial stress. For example, consider the reduction of m3m to mmm with the mirror planes of the latter perpendicular to the x, y, and z axes of the former. To retain a mirror plane under uniaxial stress, the axis of the stress must be either parallel or perpendicular to the plane. For the present setting of mmm this requires the stress axis parallel to x, y, or z; these orientations result in the preservation of a four-fold axis and the reduction is to 4/mmm rather than mmm. The other setting of mmm as a subgroup of m3m can, however, be reached by tensile stress directed along [110].

4. Discussion

4.1 Splitting of a General Position in a Space Group Into Subsets of Sites

There is a close correspondence between equivalence of directions under point-group operations and equivalence of sites in a crystal associated with one lattice point under space-group operations. There are as many equivalent general sites per lattice point of a crystal as there are equivalent general directions for the point group of the crystal. The symmetry operation connecting two sites associated with the same lattice point of a crystal must be the same as far as general rotations (i.e., proper rotation, reflection, or inversion) are concerned as the point-group operation connecting the isomorphic directions for the point group. A space-group operation in addition to a general rotation may also produce a translation which is a simple integral fraction of a lattice vector. In 73 of the space groups, termed the symmorphic space groups [12], the full point group is contained in the space group and a set of general positions associated with one lattice point must lie on a sphere surrounding that lattice point. The points representing directions in the stereograms of the present paper may be regarded as points on the surface of the reference sphere of the stereogram and so directly represent a set of general sites for a symmorphic space group [13] with the same point group. The symmorphic space groups, associated with each point group are listed in the last columns of tables 3 and 4. For a nonsymmorphic space group one can begin with a general site and produce a set of equivalent

TABLE 1. *General orientation of homogeneous tensile stress (or biaxial stress if required) causing symmetry reduction*

Initial group	Subgroup ← Minimum: m3m	m3	6/mmm	6/m	4/mmm	4/m	$\bar{3}$m	$\bar{3}$	Compound → mmm	2/m	$\bar{1}$
m3m	None	------	------	------	[100]	------	[111]	------	[110] biax.[100]	[11u] [1u0]	Any
m3	None	------	------	------	------	------	------	[111]	[100]	[1u0]	Any
6/mmm (hex-axes)	[001]	------	------	------	------	------	------	------	[100] [1$\bar{1}$0]	[1u0] [10u] [1$\bar{1}$u]	Any
6/m (hex.axes)	[001]	------	------	------	------	------	------	------	------	[1u0]	Any
4/mmm	[001]	------	------	------	------	------	------	------	[100] [110]	[1u0] [10u] [11u]	Any
4/m	[001]	------	------	------	------	------	------	------	------	[1u0]	Any
$\bar{3}$m (hex.axes)	[0$\bar{1}$1]	------	------	------	------	------	------	------	------	For $\bar{3}$m1: [1$\bar{1}$u] For $\bar{3}$1m: [11u]	Any
$\bar{3}$ (hex.axes)	[001]	------	------	------	------	------	------	------	------	------	Any
mmm	[100] [010] [001]	------	------	------	------	------	------	------	------	[1u0] [10u] [01u]	Any
2/m (2||y)	[010] [10u]	------	------	------	------	------	------	------	------	------	Any
$\bar{1}$	Any	------	------	------	------	------	------	------	------	------	Any

[10u] or similar symbol here signifies a direction of given u (any real number) or another direction related to it by the symmetry of the initial group; and biax. (for biaxial) indicates two unequal stresses along nonparallel directions of the type specified. Any directional specification is understood to exclude a more specialized direction if and only if it is appropriate to a higher order subgroup of the initial point group. Large square brackets indicate equivalent subgroups from alternative settings of axes.

sites by using first the purely rotational operations and then the operations having fractional translation also. The former produce points on a sphere and the latter may be looked upon as first rotating to produce a point also on the sphere and then translating the point off the sphere. The points on the stereograms of the present paper can still be used as a representation of a set of general sites if it is recognized that the stereogram describes only the rotational part of the symmetry operation and that for a nonsymmorphic space group some of the points would be displaced from the surface of the reference sphere by translation of an integral fraction of a lattice vector. The pattern of splitting of a general position into subsets under stress is, however, the same for all space groups, symmorphic or nonsymmorphic. That pattern is associated with a given point-group-to-point-group reduction because the operations in the space group which are lost under stress are always isomorphic to the same operations in the point group.

All of the possible space-group-to-space-group reductions associated with each of the point-group-to-point-group transitions induced by stress have been tabulated [10]. For any symmorphic space-group-to-space-group reduction in this tabulation one can collect the coordinates of a set of equivalent general sites into subsets using the present stereograms to determine the permutations and changes of sign of x, y, and z coordinates which produce equivalent sites in the subgroup. The same permutations and sign changes must also hold for any nonsymmorphic space group associated with the same point-group-to-point-group reduction; any additional translation can then be taken from the International Tables [11] because the permutations and sign of the xyz coordinates uniquely identify each site of a set of equivalent sites as given there. This has been done for the general position in each of the 230 space groups, and tables of the splitting of a set of equivalent general sites into subsets are available [6, 14] for all minimum steps of symmetry lowering.

4.2. Splitting of a Special Postion in a Space Group Into Subsets of Sites

One can specialize a direction in a point group so that it is carried into itself by some of the operations of the point group other than the identity. All such operations together with the identity must form a group; let PGS_0 represent this group and $n(PGS_0)$ represent its order. Then there will be $n(PG_0)/n(PGS_0)$ distinct directions making up a set of equivalent specialized directions of this type. The process of specialization can be visualized by picturing the motion of one of the points on any of the stereograms of figure 1. All of the other points on the same stereogram must move simultaneously to remain symmetry related. Specialization requires movement to make two or more points coincide so that the specialized direction is invariant under the opera-

TABLE 2. *General orientation of homogeneous tensile stress (or biaxial stress if required) causing symmetry reduction.*

(Symbols and notation as for table 1.)

Initial group	Subgroup ←Minimum / Compound→										
	Self subgroup	$\bar{4}2m$	422	3m	32	3	mm2	222	m	2	1
$\bar{4}3m$	None	[100]	-----	[111]	-----	-----	[110]	biax. [100]	[11u]	[10u]	Any
432	None	-----	[100]	-----	[111]	-----	-----	[110] biax. [100]	-----	[10u] [11u]	Any
23	None	-----	-----	-----	-----	[111]	-----	[100]	-----	[01u]	Any

	Subgroup					
	Self subgroup	mm2	222	m	2	1
$\bar{6}m2$ (hex. axes)	[001]	For $\bar{6}m2$: [1$\bar{1}$0] For $\bar{6}2m$: [110]	-----	[1u0] For $\bar{6}m2$: [1$\bar{1}$u] For $\bar{6}2m$: [11u]	For $\bar{6}m2$: [11u] For $\bar{6}2m$: [1$\bar{1}$u]	Any
6mm (hex. axes)	[001]	[110] [1$\bar{1}$0]	-----	[11u] [1$\bar{1}$u]	[1u0]	Any
622 (hex. axes)	[001]	-----	[110] [1$\bar{1}$0]	-----	[1u0] [11u] [1$\bar{1}$u]	Any
6 (hex. axes)	[001]	-----	-----	-----	[1u0]	Any
$\bar{6}$ (hex. axes)	[001]	-----	-----	[1u0]	-----	Any
$\bar{4}2m$	[001]	For $\bar{4}2m$: [110] For $\bar{4}m2$: [100]	For $\bar{4}2m$: [100] For $\bar{4}m2$: [110]	For $\bar{4}2m$: [11u] For $\bar{4}m2$: [10u]	[1u0] For $\bar{4}2m$: [10u] For $\bar{4}m2$: [11u]	Any
4mm	[001]	[100] [110]	-----	[10u] [11u]	[1u0]	Any
422	[001]	-----	[100] [110]	-----	[1u0] [10u] [11u]	Any
4	[001]	-----	-----	-----	[1u0]	Any
$\bar{4}$	[001]	-----	-----	-----	[1u0]	Any
3m (hex. axes)	[001]	-----	-----	For 3m1: [1$\bar{1}$u] For 31m: [11u]	-----	Any
32 (hex. axes)	[001]	-----	-----	-----	For 321: [11u] For 312: [1$\bar{1}$u]	Any
3 (hex. axes)	[001]	-----	-----	-----	-----	Any
mm2	[100] [010] [001]	-----	-----	[10u] [01u]	[1u0]	Any
222	[100] [010] [001]	-----	-----	-----	[1u0] [10u] [01u]	Any
m(⊥y)	[010]	-----	-----	-----	-----	Any
2(∥y)	[010]	-----	-----	-----	-----	Any
1	Any	-----	-----	-----	-----	-----

tions which related the now coincident directions. Several types of behavior occur separately or at the same time (in exact correspondence to the treatment of special positions in space groups [10]):

(1) Two points belonging to different subsets may be brought into coincidence on symmetry lost so that the number of sets into which the set of specialized direction splits under stress is fewer than the number of subsets resulting from the set of general directions. For example, in the stereogram for 432 to 422 the motion of a point labeled I nearest [111] onto the threefold axis along [111] causes points I, II, and III to coincide. Thus, in the unstressed crystal of point group 432 a direction of symmetry $PGS_0=3$ gives

rise to a total of $n(432)/n(3)=24/3=8$ equivalent directions. In the stressed crystal the direction [111] has $PGS_1=1$ so $n(PG_1)/n(PGS_1)=n(422)/n(1)=8/1=8$ and the specialization has changed a set of 24 splitting into 3 subsets of 8 each into a set of 8 that does not split under this stress. Unequal splitting can be demonstrated, for example, for $\bar{3}$m to 2/m, as mentioned in the introduction. Let the points labeled II and III be brought into coincidence by moving them onto the dashed lines representing lost mirror planes: this requires the points labeled I to move onto the mirror plane which is retained. In the unstressed crystal all directions have $PGS_0=m$ with $n(\bar{3}m)/n(m)=12/2=6$. In the stressed crystal one subset has $PGS_1^{(1)}=m$ with a number in the set of $n(2/m)/n(m)=4/2=2$; the other subset has $PGS_1^{(2)}=1$ and 4 directions in the set.

(2) Directions in the same subset may become identical in clusters of two or more each on symmetry retained. The specialized directions in this subset are necessarily specialized with respect to the reduced point group. In the above example of $\bar{3}$m to 2/m the coincident points labeled I were still specialized with respect to 2/m.

(3) The number of degrees of freedom in a subset may exceed the number in the original set of special directions because of loss of a constraint resulting from loss of symmetry. In the above example of $\bar{3}$m to 2/m the points of subsets resulting from coincidence of II and III were specialized to lie on mirror planes of $\bar{3}$m and so had only one degree of freedom; these planes are lost in going to 2/m as shown in the stereogram so that the points have two degrees of freedom with respect to 2/m.

The fourth columns of tables 3 and 4 list the possible specializations to PGS_0 which can be accomplished by moving the general direction on the stereogram for each point group. Sites having position point symmetry, PPS_0, equal to each possible PGS_0 must occur in each of the symmorphic space groups. The latter are listed in the last columns of tables 3 and 4. There are, however, sites of different point symmetry which can occur even in some of the symmorphic point groups because of symmetry operations which are interwoven between the lattice points when the latter are chosen to have the full point symmetry. Thus, in Fmm2 sites of symmetry 2 occur halfway between lattice points but the general direction of the stereogram for mm2 can not be specialized just to 2 but becomes mm2. Many such cases occur; columns 5–7 of tables 3 and 4 list all of the additional position point symmetries (which must be a subgroup of the initial point group) occurring in the symmorphic or nonsymmorphic space groups associated with each point group and not already listed in columns 4. One might suppose that all of the subgroups of PG_0 would occur as position point symmetries in some space group associated with PG_0, but column 8 of table 3 shows that a few exceptions exist.

The behavior of a special position of symmetry PPS_0 which is not a possible PGS_0 of the point group can be visualized by using two or more of the stereograms together. Under a stress which causes a minimum step of symmetry lowering of PG_0 to PG_1 the group PPS_0 must either remain unchanged or undergo a step of symmetry lowering but the latter need not be a minimum step. For example, $PPS_0=$

TABLE 3. *Point symmetries reached by specializing general directions for each centrosymmetric point group as applicable to stereograms; point symmetries occurring in symmorphic and nonsymmorphic space groups but not on stereograms; and point symmetries which, while forming a subgroup of the initial point group, are not found in any associated space group*

Initial group			Subgroups (other than 1)					24 centrosymmetric space-groups with full point symmetry of initial point group
Int. tables [11]	Schoenflies [11]	Shubnikov [16]	occurring on the stereogram and in at least one space group associated with the initial point group	not occurring on stereogram but in at least one			not on stereogram nor in any associated space group	
				symmorphic, but not in associated nonsymmorphic space groups	symmorphic and at least one associated nonsymmorphic space groups	nonsymmorphic but not in associated symmorphic space groups		
m3m	O_h	6/4	4mm, 3m, mm2, m	m3m, 4/mmm	$\bar{4}$3m, $\bar{3}$m, $\bar{4}$2m, mm2, 2	m3, 432, 23, 4/m, 422, $\bar{3}$, 32, 4, $\bar{4}$, 222, 3	2/m, $\bar{1}$	Pm3m, Fm3m, Im3m
m3	T_h	6/2	mm2, 3, m	m3, mmm, 2/m	23, $\bar{3}$	222, 2	$\bar{1}$	Pm3, Fm3, Im3
6/mmm	D_{6h}	m·6:m	6mm, mm2, m	6/mmm, mmm	6m2, 3m	6/m, 622, 3m, 32, 6, $\bar{6}$, 222, 2/m, 3, 2	3, $\bar{1}$	P6/mmm
4/mmm	D_{4h}	m·4:m	4mm, mm2, m	4/mmm	$\bar{4}$2m, mmm, 2/m, 2	4/m, 422, 4, $\bar{4}$, 222, $\bar{1}$	.....	P4/mmm, I4/mmm
6/m	C_{6h}	6:m	6, m	6/m, 2/m, 2	6, $\bar{3}$	$\bar{3}$, $\bar{1}$	.....	P6/m
$\bar{3}$m	D_{3d}	$\bar{6}$·m	3m, m, 2	$\bar{3}$m, 2/m	32, $\bar{3}$	$\bar{3}$, $\bar{1}$	.....	P$\bar{3}$1m, P$\bar{3}$m1, R$\bar{3}$m
4/m	C_{4h}	4:m	4, m	4/m	$\bar{4}$, 2/m, 2, $\bar{1}$	.....	.....	P4/m, I4/m
mmm	$D_{2h}(V_h)$	m·2:m	mm2, m	mmm	222, 2/m, 2, $\bar{1}$	.....	.....	Pmmm, Cmmm, Immm, Fmmm
$\bar{3}$	$C_{3i}(S_6)$	$\bar{6}$	3	$\bar{3}$, $\bar{1}$	.....	.....	.....	P$\bar{3}$, R$\bar{3}$
2/m	C_{2h}	2:m	m, 2	2/m	$\bar{1}$	.....	.....	P2/m, C2/m
$\bar{1}$	$C_i(S_2)$	$\bar{2}$	.....	$\bar{1}$	.....	.....	.....	P$\bar{1}$

TABLE 4. *Point symmetries reached by specializing general directions for each noncentrosymmetric point group as applicable to stereograms; and point symmetries occurring in symmorphic and nonsymmorphic space groups but not on stereograms*

(Point symmetries forming a subgroup of any initial noncentrosymmetric point group are found in at least one associated space group.)

Initial group			Subgroups (other than 1)				49 noncentrosymmetric space groups with full point symmetry of initial point group
			occurring on the stereogram and in at least one space group associated with the initial point group	not occurring on stereogram but in at least one			
Int. tables [11]	Schoenflies [11]	Shubnikov [16]		symmorphic but not in associated nonsymmorphic space groups	symmorphic and at least one associated nonsymmorphic space groups	nonsymmorphic but not in associated symmorphic space groups	
$\bar{4}3m$	T_d	$3/\bar{4}$	3m, mm2, m	43m, 42m	4,2	23, 222, 3	$P\bar{4}3m$, $F\bar{4}3m$, $I\bar{4}3m$
432	O	3/4	4, 3, 2	432, 422	23, 32, 222		P432, F432, I432
23	T	3/2	3, 2	23, 222			P23, F23, I23
$\bar{6}m2$	D_{3h}	m-3:m	3m, mm2, m	6m2	6, 3	32, 2	$P\bar{6}m2$, $P\bar{6}2m$
6mm	C_{6v}	6-m	6mm, m	mm2	3m	6, 3, 2	P6mm
622	D_6	6:2	6, 2	622	32, 222, 3		P622
$\bar{4}2m$	$D_{2d}(V_d)$	$\bar{4}$-m	mm2, m, 2	42mm	4, 222		$P\bar{4}2m$, $P\bar{4}m2$, $I\bar{4}m2$, $I\bar{4}2m$
4mm	C_{4v}	4-m	4mm, m		mm2	4, 2	P4mm, I4mm
422	D_4	4:2	4, 2	422	222		P422, I422
6	C_6	6	6		3, 2		P6
$\bar{6}$	C_{3h}	3:m	3, m	6			$P\bar{6}$
3m	C_{3v}	3-m	3m, m		3		P3m1, P31m, R3m
32	D_3	3:2	3, 2	32			P312, P321, R32
4	C_4	4	4		2		P4, I4
$\bar{4}$	S_4	$\bar{4}$	2	4			$P\bar{4}$, $I\bar{4}$
mm2	C_{2v}	2-m	mm2, m		2		Fmm2, Imm2, Pmm2, Cmm2, Amm2
222	$D_2(V)$	2:2	2	222			P222, C222, I222, F222
3	C_3	3	3				P3, R3
m	$C_s(C_{1h})$	1-m	m				Pm, Cm
2	C_2	2	2				P2, C2
1	C_1	1					P1

4/m occurs in some space groups associated with PG_0=m3m; tensile stress along [111] causes the minimum step m3m to $\bar{3}$m but also causes the compound step in position point symmetry 4/m to $\bar{1}$. These results can be visualized from the stereograms for m3m to $\bar{3}$m and 4/m to 2/m. The latter shows the only minimum step for 4/m and shows that m perpendicular 4 must be preserved; the former shows that all mirror planes perpendicular to 4-axes are lost. The combination of a minimum step of symmetry lowering of PG_0 with a compound step for PGS_0 on a stereogram can also occur as the example of m3m to $\bar{3}$m accompanied by 4/mmm to m shows.

This type of visualization can be applied to any PPS_0 of PG_0 but it should be noted that the orientation of PPS_0 is fixed by PG_0 so that a stereogram of PPS_0 as initial group may require reorientation to correspond to the setting in PG_0.

4.3. Effect of Homogeneous Stress on Morphology of Crystals

The identity of the 32 morphological crystal classes with the 32 three-dimensional point groups is well understood (Phillips [15]). A straight forward application therefore of the stereograms here presented would appear to be that concerned with changes in homogeneously strained crystals. From the practical experimental viewpoint, however, the application of homogeneous stress (other than isostatic) to a polyhedrally shaped object is difficult to visualize and more difficult to achieve. Apart from general mathematical treatment there seems so far to have been little interest by practical crystallographers in the homogeneous distortion of crystal shapes. For general forms minimum step degradations can be directly read from the figures as conversions to general forms of the subgroup. The number of now independent but co-existing forms in the subgroup is simply $\frac{n(PG_0)}{n(PG_1)}$ the ratio of the order of the initial to that of the final subgroup, the splitting factor sometimes called the index of the subgroup. It can simply be read off the stereograms given as the highest Roman figure designation of a direction on the stereogram of the parent group.

In this way for example a compressive stress

$\|[111]$ for a crystal belonging to m3m will convert one $\{hkl\}$ hex(akis)octahedron to four hexagonal bipyramids.

A randomly oriented stress will convert any general form into unrelated triclinic $\{hkl\}$ pedia (for noncentrosymmetric crystals) or $\{hkl\}$ pinacoids (for centrosymmetric crystals). The number of forms being simply the order (for noncentrosymmetric) or half the order (for centrosymmetric crystals) of the initial point group.

All possible intermediate compound steps can be read off tables 1 and 2. The forms produced from general forms in PG_0 are always general forms $\{hkl\}$ in the ultimate subgroup and their number again equals the ratio of the order of the initial to that of the final point group.

When special forms are involved the procedure follows that outlined above for cell site co-ordinates; the only possible special forms being those listed in the fourth column of tables 3 and 4.

Faces will belong to special forms in the subgroup if any one of the original symmetry operations, the stereographic representation of which is parallel to the pole of the face, is retained in the degradation.

When an initial point group has a number of equivalent symmetry operations, stress may lead to the loss of one or more of these operations, yet leave one or more of them in the subgroup. Directions specialized with respect to these initially equivalent symmetry operations will split unequally. For example, in the transformation m3m to 4/mmm, a $\{100\}$ cube, with six faces, will split into a tetragonal basal pinacoid $\{001\}$ with two faces and a tetragonal (first order) prism $\{100\}$ with four faces.

No splitting of the special form will result if special-form poles can be regarded as having arisen from the superposition, on symmetry operations, of poles including at least one with each Roman-figure designation. The shape of the solid figure naturally will change. For example, as m3m transforms to 4/mmm, $\{111\}$ changes from a regular octahedron to a (2d order) tetragonal bypyramid. As 4/mmm transforms further to mmm in one orientation $\{111\}$ becomes a rhombic bipyramid, the general form of that class. In the 45° position, however, it would split into two unrelated rhombic domes. Further symmetry degradation must also split the rhombic bipyramid, because it is the general form. In other words: the faces of the original octahedron $\{111\}$ number eight, its faces cannot remain all equivalent when degradation proceeds to a subgroup of order less than eight.

In this way it is easy to deduce which crystallographic forms can be transformed by homogeneous stress into which others. Conversely, if there is no simple or compound subgroup relationship that will transform any one given form in any of the point groups in which it occurs into another form with an appropriate subgroup symmetry then there exists no homogeneous stress that can effect that transformation. For example—as is well known to geometers—a tetrahedron, $\{111\}$ in $\bar{4}3m$, can be homogeneously deformed to a tetragonal sphenoid $\{111\}$ in $\bar{4}2m$, and to a rhombic bisphenoid, $\{111\}$ in 222, but not to a rhombic dome, which also has four faces.

However, some care is necessary in deducing that a given transformation is impossible, because the special forms of some classes are indistinguishable from some special and, in one or two instances, even general forms (taken singly) of other classes.

There are a number of other applications of this kind of morphological discussion of homogeneously strained crystals. Temperature, pressure, or composition changes may lead to phase transformations (displacive) in which no primary bonds are broken in the solid [16]. Such changes may or may not be consistent with changes that could arise by homogeneous deformation as here described. This will introduce a further meaningful subclassification of the transformations discussed by Buerger [16].

Another, completely different, consideration may prove to be fruitful. Crystal growth results in shapes that often depart considerably from ideal symmetry of the atomic structure. A number of causes for these departures are established, and relatively well understood:—

1. Accidental asymmetry of supply of solute or melt to equivalent faces;
2. Retardation of growth of some faces by substrate interference or competition for solute or liquid with neighboring crystals;
3. Accidental differences in the small number of growth step sources on otherwise equivalent faces; and
4. Geometric complications arising from twinning.

An additional effect suggests itself. Stress during growth may make faces inequivalent causing unequal growth rate on otherwise equivalent faces. On examination of the crystals after stress removal the equivalence of the faces demanded by structural symmetry is reestablished, yet the asymmetry of shape persists.

This effect to be discerned may need to be studied deliberately and carefully under laboratory conditions. Certainly two outstanding anomalies (some diamond and cuprite crystals) of known minerals with morphology suggestive of lower symmetry than their established structure [17] can not be explained by homogeneous strain during growth. These two anomalies are accompanied by anomolous etch figures. Any stress induced inequivalence of structure, that gives rise only to homogeneous elastic strain, should vanish when the stress is removed.

5. Appendix I

We here present a simple, systematic, and exhaustive scheme for deriving all possible subgroups that can be reached by the action of homogeneous stress on any point group.

Let us introduce a number of concepts and symbols. First, consider any stress ellipsoid, E_p, which in shape and orientation is least restricted yet still consistent with any original point group (cf. table 13, reference 5). Stress-induced symmetry lowering can be caused only by an imposed stress of which the ellipsoid representation, E_s, does not conform to all the re-

strictions in E_p. Point-group degradations for each initial point-group, PG_0 can now be regarded as associated with liberalizations, L, of these restrictions imposed on E_p.

We will distinguish L_S and L_0 liberalizing ellipsoid shape and orientation respectively. All PG degradations can be regarded as caused by one or both of these applied to E_p. We further classify into L_{SR}, L_{ST}, L_{01}, and L_{02}.

L_{SR} is a shape liberalization leading to an ellipsoid of revolution with unique axis parallel to a crystal axis [2] of order >2. As the only more restrictive stress ellipsoid is a sphere the operation L_{SR} need be considered only when PG_0 is cubic, for which the L_{SR} operation produces one or two symmetry degradations depending on whether there are one or two nonequivalent, nonparallel axes of order >2 in PG_0.

L_{ST} is a shape liberalization leading to a triaxial ellipsoid, the major axes of which are parallel to three mutually perpendicular crystal axes of even order, in PG_0. As E_p is more specialized only when PG_0 contains at least one axis of order >2, L_{ST} applies only to such PG_0's; and then only if PG_0 has either one or two inequivalent sets of three mutually perpendicular axes of even order. More than two such sets cannot occur in any PG_0, at least one such set must occur for all cubic PG_0's.

L_{01} we define as a liberalization to a triaxial ellipsoid (including L_S if PG_0 has axis of order >2) with one orientational degree of freedom. L_{01} must lead to one of the following subgroups: 2,m, or 2/m. From any PG_0 there will be as many distinct ways of applying the L_{01} operation as there are nonequivalent nonparallel axes of even order symmetry in PG_0. Cubic point-groups have at least one and never more than two such directions. Noncubic PG_0 may have none, one, two, or at most, three such directions. Nonequivalent L_{01} operations on any centrosymmetric PG_0 must all lead to 2/m, but for noncentrosymmetric PG_0's they may or may not lead to the same subgroup.

L_{02} is a liberalization to a triaxial ellipsoid with two orientational degrees of freedom; the operation is regarded as including an L_S operation from PG_0's with an axis of order >2. Application of L_{02} to centrosymmetric PG_0's always produces the subgroup $\bar{1}$ and none other, noncentrosymmetric PG_0's lead only to 1.

The aim of the treatment here given is to consider the symmetry and orientation of E_p; then to apply the liberalizations, L, until the symmetry and orientation of E_s is obtained. This process cannot always be accomplished because E_s may in some respects be more restricted than can be derived from E_p by L-type operations. We must therefore liberalize E_s to E_s' where E_s' is a more general ellipsoid which can be reached from E_p by operations L and which will produce the same symmetry lowering as E_s.

If E_s is a triaxial ellipsoid it is in an adequately general form because it can be obtained from any ellipsoid by operations L_{ST}, L_{01}, or L_{02}. If E_s is a biaxial stress, one need only add an arbitrary isostatic stress to obtain an acceptable E_s'. It has previously been pointed out [10] that the addition of such an isostatic stress can not affect the symmetry lowering. The only important case to be considered therefore is that of a stress E_s corresponding to an ellipsoid of revolution, or a uniaxial stress which by the addition of an arbitrary isostatic stress can be transformed to one corresponding to an ellipsoid of revolution. We must now distinguish two possible conditions as follows:

Condition 1: unique ellipsoid axis is parallel to a crystal axis (in PG_0) of order >2. The symmetry of E_s can not be further reduced without affecting the symmetry lowering. No further generalization of E_s is therefore possible.

Condition 2: unique ellipsoid axis is parallel to a crystal axis (in PG_0) of order ≤ 2. There is now necessarily a uniaxial stress which can be added perpendicular to the unique E_s ellipsoid axis which will leave the symmetry lowering unaffected. If in PG_0 there is no even order axis perpendicular to the unique ellipsoid axis the direction of the additional uniaxial stress is entirely arbitrary. If there are one or two perpendicular directions of axial even order ≥ 2 in the plane perpendicular to the unique ellipsoid axis the additional uniaxial stress must be added parallel to one axis in the plane.

Our general scheme of deriving all subgroups can now be stated.

All proper subgroups are developed by operations L_{SR}, L_{ST}, L_{01}, and L_{02}, each in turn considered as acting upon PG_0.

The number of proper subgroups obtained is:

	L_{SR}	L_{ST}	L_{01}	L_{02}	Maximum number possible	Example
PG_0 cubic	1 or 2	1 or 2	1 or 2	1	7	m3m
PG_0 one and only one axis order >3	0	0, 1, or 2	1, 2, or 3	1	6	4/mmm
PG_0 one and only one axis order $=3$ and none of higher order	0	0	0 or 1	1	2	$\bar{3}$m
PG_0 with axis order 2 and none of higher order	0	0	1 or 3	1	4	mmm

[2] In this discussion symmetry axes may be rotation or inversion axes.

The naming of the individual subgroups is trivial when we remember that a center in PG_0 is always retained; that for L_{SR} the first symbol is derived from the only axial direction parallel to the ellipsoid axis of revolution. The necessary and sufficient condition of 2-axes retention is then that they be parallel or perpendicular to that direction; that for L_{ST} only the crystal axes (order 2) parallel to the principal ellipsoid axes are retained; that for L_{01} only one axial symmetry direction (order 2) can be retained.

Minimum steps are produced by all L_{SR} operations; by all L_{ST} operations except when PG_0 is cubic and has three axes of order 4; by L_{01} operations when the operation L_{ST} on PG_0 is inapplicable; and by L_{02} operations only if PG_0 has only one axial direction of order two or three.

The authors are indebted to F. A. Munley and L. C. McCleary for help in the preparation of the manuscript as well as especially to W. F. Stancliff for the drawing of the stereograms.

6. References

[1] J. F. Nye, Physical properties of crystals, Oxford University Press (1957).

[2] V. A. Koptsik, Polymorphic Phase Transitions and Symmetry, Soviet Physics Crystallography **5,** 889 (1961). Translated from Kristallografiya **5,** 932 (1960).

[3] J. B. Wachtman, Jr., and H. S. Peiser, Symmetry conditions for internal friction caused by jumping of point defects in crystals, App. Phys. Letters **1,** 20 (1962)

[4] R. L. Aggorwal and A. K. Ramdas, Effect of uniaxial stress on the excitation spectra of donors in silicon, Phys. Rev. **137,** A 602 (1965).

[5] Elsa Rosenvasser Felker, Effect of uniaxial stress on the paramagnetic spectra of Mn^{3+} and Fe^{3+} in MgO, Phys. Rev. **136,** A 145 (1964).

[6] H. S. Peiser, J. B. Wachtman, Jr., and R. W. Dickson, Reduction of space groups to subgroups by homogeneous strain, J. Research NBS **67A,** 395 (1963).

[7] A. S. Nowick and W. R. Heller, Anelasticity and stress-induced ordering of point defects in crystals, Adv. in Phys. **12,** 251 (1963).

[8] J. B. Wachtman, Jr., H. S. Peiser, and E. P. Levine, Symmetry splitting of equivalent sites in oxide crystals and related mechanical effects, J. Res. NBS **67A,** 281 (1963).

[9] A. S. Nowick and W. R. Heller, Dielectric and anelastic relaxation of crystals containing point defects, Adv. in Phys. **14,** (1965).

[10] J. B. Wachtman, Jr. and H. S. Peiser, Splitting of a set of equivalent sites in centrosymmetric space groups into subsets under homogeneous stress, J. Res. NBS **69A,** No. 2, 193–207 (1965).

[11] N. F. M. Henry and Kathleen Lonsdale, editors, International tables for x-ray crystallography, Vol. I, Kynoch Press, Birmingham (1952).

[12] G. F. Koster, Space groups and their representations, Solid State Physics, Vol. 5, pages 173–256, Edited by F. Seitz and D. Turnbull, Academic Press, New York (1957).

[13] F. Seitz, A matrix-algebraic development of the crystallographic groups, Z. Krist. **88,** 433 (1934); **90,** 298 (1935); **91,** 336 (1935); **94,** 100 (1936).

[14] H. S. Peiser, J. B. Wachtman, Jr., F. Munley, and Linda C. McLeary, Splitting of a set of equivalent points in noncentrosymmetric space groups into subsets under homogeneous stress, J. Res. NBS **69A,** No. 5 (1965).

[15] F. C. Phillips, An Introduction to Crystallography (Wiley, N.Y., 1964).

[16] M. J. Buerger, Crystallographic aspects of phase transformations, pp. 183–211 in Phase Transformations in Solids, edited by R. Smoluchowski, J. E. Mayer, and W. A. Weyl (John Wiley & Sons, New York, N.Y., 1951).

[17] A. P. Honess, The Nature, Origin, and Interpretation of Etch Figures on Crystals (John Wiley, N.Y., 1927).

[18] A. V. Shubnikov, N. V. Belov, and others, "Colored Symmetry" Translated from the Russian by J. Itzkoff and J. Gollob; Edited by W. T. Holser, Pergamon Press (1964).

(Paper 69A4–351)

JOURNAL OF RESEARCH of the National Bureau of Standards—A. Physics and Chemistry
Vol. 69A, No. 4, July–August 1965

Effect of Hydrostatic Pressure on the Refractive Indices of Some Solids

R. M. Waxler and C. E. Weir

(March 3, 1965)

Measurements were made on refractive index changes with hydrostatic pressures between 1 bar and 1 kbar using the helium yellow line. The materials studies were: KBr NaCl, LiF, diamond, MgO, quartz, Al_2O_3, and three silicate glasses. All the materials increased in refractive index with pressure except diamond, MgO, and Al_2O_3 which decreased, and LiF which did not change. The results were compared with photoelastic measurements, and Pockel's geometric theory of photoelasticity was substantiated as well as Mueller's physical theory. The data show that the ratio of change of polarizability with density is greater for solids having stronger interatomic repulsive forces. Volume and temperature coefficients of polarizability were evaluated for the cubic crystals and glasses. The thermo-optic behavior of crystals and glasses is discussed.

1. Introduction

The relationship between index of refraction and density is of importance because of the effect of atomic interactions on the atomic polarizabilities. For transparent solids, values of $\rho d\mu/d\rho$, where μ is the index and ρ the density, have been obtained by calculation from the photoelastic constants [1].[1] For crystals as well as glasses values of $\rho d\mu/d\rho$ so calculated usually have been found to be less than the corresponding values calculated on theoretical grounds, i.e., from the Lorentz-Lorenz and the Drude relationships [1]. The most extreme example of this discrepancy is probably found in the case of diamond and MgO where $\rho d\mu/d\rho$ values calculated from photoelastic constants are negative, a result which is clearly impossible to reconcile with the assumption of constant polarizability involved in the initial derivation. The theory of photoelasticity due to Mueller [2, 3] recognizes the change in the intrinsic polarizability of an atom due to strain.

For glasses, data on $\rho d\mu/d\rho$ have been obtained by Ritland [4] (and others) in the annealing temperature range where both index and density change with time at constant temperature and on volumetric relaxation following removal of high hydrostatic pressures [5]. In the former case $\rho d\mu/d\rho$ is found to be somewhat less than theory predicts and in the latter case somewhat greater.

Direct experimental data on $\rho d\mu/d\rho$ are required to understand thermo-optic properties. Values of $d\mu/dT$, where T is the temperature, have been measured for many solids and it is known that the sign may be either positive or negative. For most crystals $d\mu/dT$ is found to be negative but in the case of diamond, MgO, and ZnS the reverse is true [6]. Recent work has shown that for Al_2O_3 $d\mu/dT$ is positive for both the ordinary and extraordinary rays [7]. Most optical glasses exhibit a minimum in the μ-T curve somewhat below room temperature so that at and above room temperature $d\mu/dT$ is positive but at some lower temperature the sign reverses [8]. Any attempt to explain such a complex thermo-optic behavior must of necessity require an understanding of the $\rho d\mu/d\rho$ effect because thermal dilatation is an important contributing factor to the value of $d\mu/dT$.

Finally, by reversal of the customary procedure, data on $\rho d\mu/d\rho$ may be used to evaluate photoelastic constants in certain instances. For glasses only two constants are required, so that knowledge of $\rho d\mu/d\rho$, plus information on the optical path difference produced by a unidirectional stress serves to determine completely the photoelastic constants.

For these several reasons it was considered of interest to obtain direct measurements of the density coefficient of refractive index, $\rho d\mu/d\rho$, in solids at constant temperature by the application of hydrostatic pressure. This is the first time that such an approach has been used. This report contains data on $\rho d\mu/d\rho$ obtained in the pressure interval between 1 bar and approximately 1000 bars for several crystals and glasses of interest. Data were obtained from specimens of the cubic ionic crystals, LiF, KBr, NaCl, and MgO; the covalent cubic crystal, diamond; and the birefracting crystals, Al_2O_3 and quartz where both the ordinary and extraordinary rays were studied. The glasses studied were fused silica, a commercial plate glass and a borosilicate crown glass, BSC 517/645. Measurements reported here were made only at 25 °C using the helium yellow line.

2. Experimental Method

In these experiments interference fringes were observed in a plate of the material having plane, polished, nearly parallel faces [9]. The fringes were viewed in reflection using collimated helium light of

[1] Figures in brackets indicate the literature references at the end of this paper.

λ=5875.62 Å at normal incidence. For a specimen of thickness, t, and index, μ, the fringe number N is given by the expression

$$N\lambda=2t\mu. \tag{1}$$

Application of hydrostatic pressure will produce a change in μ, a decrease in t, and a shift in the interference fringes. By differentiating (1) and rearranging it is found that

$$\Delta\mu=\frac{\Delta N\lambda}{2t}-\mu\frac{\Delta t}{t}. \tag{2}$$

A measurement of the number of fringes that pass a point of reference, and the thickness together with data on the initial index and the linear compression $\Delta t/t$ permits calculation of the change in index.

The experimental apparatus and method have been described earlier in detail and will only be outlined here [10]. Briefly, a plate of the test specimen is immersed in liquid in a pressure vessel equipped with glass windows. Hydrostatic pressure is generated by compressing the liquid and the number of interference fringes passing a reference line, i.e., the fringe count, was determined visually. Estimates of the number of fringes were made to the nearest tenth of a fringe.

The change in fringe number observed in approximately 1 kbar is not very large for these solids because of their rather low compressibilities compared to the liquids previously studied and because the decrease in thickness under pressure acts in such a direction as to decrease the fringe number (see eq (2)). In the most favorable case ΔN is known only to three significant figures. Extreme precision in the other quantities is not required. The most reliable values for the initial indices were used, however, and values for the index at the frequency of the He yellow line were generally obtained by interpolation of the dispersion data reported. The data on the indices of refraction of the solids may be found in references [11] through [20]. For BSC 517/645 the index was reported for the sodium D line only. However, from the low dispersion of such glasses and the small frequency separation of the sodium and helium yellow lines, the value reported was assumed to apply to the present measurements within the required precision.

Compression data for all materials except BSC 517/645 have been reported, usually in terms of volume compression ($\Delta V/V_0$). Volume compressions were converted to linear values for the isotropic materials through the relationship $\Delta t/t_0=\frac{\Delta V}{3V_0}$. For quartz and Al_2O_3, where data on linear compressions are available, $\Delta t/t_0$ was computed for the direction perpendicular to the optic axis. The data for determining the compression of the solids may be found in references [21] through [26]. (For BSC 517/645 the linear compression was calculated from elastic constant data measured at 1 bar [27].) It has been estimated that, at most, the uncertainty in values of $\Delta t/t_0$ lies in the third significant figure.

For the optically isotropic solids (cubic crystals and glasses) the measurements were straightforward but for the crystals of lower symmetry, Al_2O_3 and quartz, which are optically anisotropic the method was modified to permit measurements for both the ordinary and extraordinary ray. For these materials the specimen was oriented so that the optic axis was perpendicular to the direction of the light beam. In the measurements a large polarizer was inserted between the source and the window of the pressure vessel. On rotating the polarizer two distinct fringe systems could be seen depending on whether the electric vector of the plane polarized light transmitted by the polarizer was parallel or perpendicular to the optic axis of the specimen. (For the quartz crystal which is optically active, it should be noted that, since the fringes were obtained by reflection, the emergent polarized light was still plane polarized in the same plane at which it was incident [28]. This would not have been true if the fringes were observed in transmission [16].) On applying hydrostatic pressure the fringe shift for each separate fringe system was noted, giving data on both rays for the birefringent crystals.

3. Preparation of Specimens

Most specimens were prepared by sectioning or clearing larger samples of commercially available synthetic single crystals. However, both quartz and diamond were prepared from naturally occurring single crystals. The glasses were of commercial origin. Although the test specimen required was approximately 1 cm × 1 cm × 0.5 cm, it was found expedient to grind and polish larger specimens and then to cut the final specimen from the most perfectly ground portion of the large piece. Rough blanks of both Al_2O_3 and quartz were cut with the optic axes in approximately the correct orientation. The blanks were then oriented using the Laue back-reflection x-ray technique and ground so that the optic axis was in the surface of the specimen.

3.1. Grinding and Polishing

A brief account is given here of the preparation of the crystals because these techniques are not widely known. The specimens were first ground flat and with nearly parallel surfaces using a surface grinder for the harder materials and using hand grinding with fine abrasive for the alkali halides. The harder crystals were prepolished on a wood lap with 8μ–22μ diamond powder using olive oil lubricant and then given a final polish on cloth impregnated with 3μ diamond dust using an alcohol-water solution as a lubricant. The alkali halides were given only the latter of the two polishing steps. Al_2O_3 specimens were available only in small diameters and the grinding and polishing operation was conducted on an assemblage of five small disks, set in wax on a flat glass plate.

The diamond was a 2 carat brilliant cut gemstone and the table face was found to be satisfactory for one surface. The culet was ground down parallel to

the table face using a high speed steel lap impregnated with diamond powder to produce a surface approximately 1 mm in width. Satisfactory fringes could be observed through this small surface.

In all polishing operations it was necessary to check the fringe system at frequent intervals. If it was noted that the surfaces were deviating too much from parallelism adjustments were made in the polishing to reduce the angle between the surfaces.

3.2. Aluminizing

In order to improve the sharpness of the interference fringes the reflecting power of the surfaces of the specimens was increased by vacuum deposition of a layer of aluminum. The front surface of each specimen was covered with a partly reflecting film while the rear surface was made fully reflecting. Multiple reflection fringes were obtained in this manner but because of the large thickness to length ratio of the specimens the fringes were not extremely sharp. A series of depositions of different thicknesses were made on the front surface of plate glass specimens until the fringes appeared to reach a maximum intensity and sharpness. This film thickness was found to be satisfactory for all other specimens.

TABLE 1. *Pressure induced changes in refractive index as measured with helium yellow radiation of 5875.62 Å*

Material	Refractive index, μ_{He}	Specimen thickness, l_0	Pressure, P	Thickness change, $-\Delta l/l_0\times10^3$	Observed change in fringe number $-\Delta N$	Change in refractive index $\Delta\mu\times10^5$
		Cm	*bars*			
KBr	1.560	0.3210	966.1	2.118	11.3	227
NaCl	1.546	.6748	963.6	1.348	21.6	115
LiF	1.392	.5683	963.2	.349	9.4	0
MgO	1.738	.3970	960.8	.190	6.8	−17
Diamond	2.418	.4037	960.0	.058	3.4	−11
Quartz:						
ω	1.545	.5112	957.6	.944	6.9	103
ϵ	1.554	.5112	961.5	.948	7.5	107
Sapphire:						
ω	1.769	.5659	961.8	.105	6.2	−14
ϵ	1.760	.5659	957.6	.105	6.2	−14
Fused SiO_2	1.458	.4967	960.2	.865	7.3	83
BSC 517/645	1.517	.6093	960.1	.717	8.9	70
Plate glass	1.518	.6566	960.0	.723	9.1	69

4. Results

The results of the experiments are given in table 1 which shows the decrease in fringe number, the dimensional change calculated at the pressure given and the change in index of refraction. It should be noted that the change in fringe number is presented in table 1 for the direction of increasing pressure, i.e., between 1 bar and the pressure listed. For birefracting crystals the index for the ordinary and extraordinary rays are noted by ω and ϵ respectively. Each value of ΔN given in table 1 represents the average of at least two determinations. Such duplicate measurements agreed to within ±0.1 interference fringe. From the agreement between the duplicate measurements the limit of reproducibility in the index change is estimated to be $\pm2\times10^{-5}$.

From the tabular data it is seen that the change in index is quite small in absolute value, varying from 0 in LiF to 2 in the third decimal place for KBr. The index decreases for MgO, diamond and both the ordinary and extraordinary rays of Al_2O_3. All other materials show an increase in index except LiF for which the index is unchanged. For the birefracting crystals both the ordinary and extraordinary rays show the same change in index within the limits of error.

5. Discussion

5.1. Cubic Crystals

From the experimental values of $\Delta\mu$ and the compressibility data, it was possible to calculate values for the quantity $\rho\dfrac{\Delta\mu}{\Delta\rho}$ where ρ is the density. For the cubic crystals studied here the theory of photoelasticity shows that $\rho\dfrac{d\mu}{d\rho}$ can be calculated by the relationship

$$\rho\frac{d\mu}{d\rho}=\frac{\mu^3}{6}(p_{11}+2p_{12}), \tag{3}$$

where the elasto-optic constants, p_{ij}, relate the state of strain existing in a crystal to changes in the index ellipsoid [6]. These values have been calculated for a number of crystals [1, 6] and the results are given in table 2 together with the initial indices, μ. [The values of these experiments obtained over the pressure interval of approximately 1 kb are denoted $\rho\Delta\mu/\Delta\rho$ while those from the photoelastic theory are designated as $\rho d\mu/d\rho$]. It may be noted that the photoelastic data were obtained for the sodium D line and the present data for the helium yellow line. However, because of the small frequency difference between the two lines and the known low-frequency dependence of $\rho d\mu/d\rho$ [29, 30] any differences arising from dispersion effects can be taken to be negligible.

TABLE 2. *Values of* $\rho\left(\frac{\Delta\mu}{\Delta\rho}\right)$ *and* λ_0 *for cubic crystals and glasses*

Material	Refractive index, μ_0	$\rho\left(\frac{\Delta\mu}{\Delta\rho}\right)$	$\rho\left(\frac{d\mu}{d\rho}\right)$	L–L equation		Drude equation	
				$\rho\left(\frac{\partial\mu}{\partial\rho}\right)$	λ_0	$\rho\left(\frac{\partial\mu}{\partial\rho}\right)$	λ_0
KBr	1.559	0.35	0.35	0.68	0.48	0.46	0.24
NaCl	1.544	.28	.24	.66	.58	.45	.38
LiF	1.392	.00	.1	.44	1.00	.34	1.00
MgO	1.736	−.31	−.40	.97	1.32	.52	1.60
Diamond	2.417	−1.58	−.28	2.62	1.60	1.00	2.58
Fused SiO_2	1.458	.32	.29	.53	.40	.39	.17
BSC 517/645	1.517	.33		.62	.47	.43	.24
Plate glass	1.518	.32		.62	.49	.43	.26

A comparison of the figures in table 2 shows that there is essential agreement between the predictions of photoelastic theory developed by Pockels [31] and the actual measured values. Considering the errors inherent in the measurements of the photoelastic constants [6], i.e., small fringe shifts, nonuniformity of stress distribution in uniaxial compression, etc., it is considered that the agreement in table 2 is satisfactory except in the case of diamond. For this material, however, the errors in the photoelastic experiments and in the present work are likely to be particularly large because of the small specimens available and the small changes that are observed. There is no question as to the negative sign of $\rho\Delta\mu/\Delta\rho$ for diamond, and it is interesting to note that the results of the present experiments bear out the theoretical predictions of negative values of $\rho\Delta\mu/\Delta\rho$ for both MgO and diamond.

The data for diamond obtained in this study are in much better agreement with the results of Gibbs and Hill [32] on the change of the dielectric constant of diamond with pressure. Gibbs and Hill noted that the dielectric constant of diamond, $\epsilon=5.66$ at 27 °C at frequencies as high as 10 MHz is equal to the square of the optical index of refraction at infinite wavelength, μ_∞, reported by Peter [14]. Since ρ is proportional to $1/V$, $(\partial \ln \rho/\partial P)_T=-(\partial \ln V/\partial P)_T=\beta$, where P is the pressure and β the compressibility. It follows that

$$\rho\left(\frac{\partial\mu_\infty}{\partial\rho}\right)_T\equiv\left(\frac{\partial\mu_\infty}{\partial P}\frac{\partial P}{\partial \ln \rho}\right)_T=\frac{1}{\beta}\left(\frac{\partial\mu_\infty}{\partial P}\right)_T.^2 \qquad (4)$$

If $\epsilon=\mu_\infty^2$, it follows that

$$\frac{1}{\mu_\infty}\left(\frac{\partial\mu_\infty}{\partial P}\right)_T=\frac{1}{2\epsilon}\left(\frac{\partial\epsilon}{\partial P}\right)_T. \qquad (5)$$

If the value of $\rho\left(\frac{\Delta\mu}{\Delta\rho}\right)$ in the present study is used for $\rho(\partial\mu_\infty/\partial\rho)_T$ in eq (4), and employing the equivalence shown in eq (5), $(1/\epsilon)(\partial\epsilon/\partial P)_T$ for diamond has been found to have the value -2.28×10^{-7} bar $^{-1}$. The value obtained experimentally by Gibbs and Hill for a type I diamond is -2.40×10^{-7} bar^{-1}.

[2] The derivation leading to eq (4) was suggested by D. D. Wagman of NBS.

5.2. Glasses

Experimental values for $\rho\Delta\mu/\Delta\rho$ for the glasses are given in table 2. The values are very similar for all three glasses and probably reflect the fact that the data are determined largely by the SiO_4 tetrahedra common to all three glasses. Numerical comparisons with photoelastic theory can be made only for vitreous SiO_2 for which Jog [29] has reported the necessary photoelastic data. As seen in the table the value of $\rho d\mu/d\rho$ calculated from the photoelastic constants is in reasonably good agreement with the value obtained here by direct measurement. All three glasses show positive values for $\rho\Delta\mu/\Delta\rho$. Furthermore the photoelastic data on numerous optical glasses reported by Schaeffer and Nassenstein [33], Vedam [34], and Mueller [3] invariably indicate positive values for $\rho d\mu/d\rho$. This fact will be discussed later.

5.3. Noncubic Crystals

It is interesting to note that the increase in index for both rays in quartz is greater than observed in fused silica. The result can be explained only by the conclusion that interatomic interactions play an effective role in the index change with density and that those are different in the crystal and the glass because of the crystal structure and the higher initial density of the crystal. From the data of table 1 it appears that the extraordinary ray suffers the larger change in index but the difference is probably within the experimental error. Pockels [35] has measured the photoelastic constants of quartz and his results can be extrapolated linearly to the present pressure of 957 bars to permit calculation of $\Delta\mu$. Under these circumstances the photoelastic data yield calculated values for the change of index of 100×10^{-5} for the ordinary ray and 104×10^{-5} for the extraordinary ray. These values are in good agreement with the results of the present studies. In contrast to quartz both rays of sapphire show the same change in index but both are negative. There do not appear to be enough photoelastic data available to permit calculations of the index change for Al_2O_3 [7].

5.4 Photoelastic Constants of Glass

From the present data on $\Delta\mu/\Delta P$ and auxiliary data on the amount of double refraction introduced into glass by uniaxial compression it is possible to compute the constants q_{11} and q_{12}, where the piezooptic constants, q_{ij}, relate the state of stress which exists in a solid to changes in the index ellipsoid [6]. The relationships used [34] are as follows:

$$\Delta\mu/\Delta P=\mu^3[q_{11}+2q_{12}]/2 \qquad (6)$$

and

$$(\Delta\mu_2-\Delta\mu_1)/\Delta P=\mu^3[q_{12}-q_{11}]/2, \qquad (7)$$

where, in addition to the terms previously defined, $\Delta\mu_2$ and $\Delta\mu_1$ represent changes in index for light polarized respectively perpendicular and parallel to

the stress direction. (In eq (7), ΔP denotes a change in a compression applied in one direction only.) The quantity $(\Delta\mu_2-\Delta\mu_1)/\Delta P$ is defined as the relative stress optical coefficient and has been reported to be 2.81 brewsters for BSC 517/645 [36] and 2.62 brewsters for plate glass [37]. These data plus values of $\Delta\mu/\Delta P$ serve to determine values for q_{11} and q_{12} from eq (6) and eq (7). These values are given in table 3. Values of Neumann's photoelastic constants, p and q, are also given in table 3; the relationships used in evaluating them are given by Vedam [34].

The elasto-optic constants, p_{11} and p_{12} can also be calculated from the relationships given by Vedam [34]. Values of the elastic moduli needed in the calculations are given by Spinner for BSC 517/645 [27]. From measurements made on commercial plate glass [38], values for Young's modulus, the rigidity modulus and Poisson's ratio have been found to be 723.9 kbar, 297.9 kbar, and 0.215 respectively. These values were used to calculate the elasto-optic constants for plate glass shown in table 3.

TABLE 3. *The photoelastic constants of BSC 517/645 and plate glass*

Glass	p	q	p_{11}	p_{12}	$q_{11}\times10^{13}$	$q_{12}\times10^{13}$
					cm²/dyne	*cm²/dyne*
BSC 517/645	0.168	0.087	0.115	0.221	0.315	1.92
Plate glass	.154	.087	.114	.203	.369	1.87

5.5. Polarizability and Density

It seems self-evident that density changes must be accompanied by some change in molecular or atomic polarizability and it is useful to analyze the present data to ascertain what information can be obtained in this connection. The most comprehensive theory appears to be due to Mueller [2, 3] who considers the following factors involved in change of refractive index of a solid under applied stress: (1) change of density; (2) change of the Lorentz-Lorenz field; (3) change of the coulomb field; and (4) change in the intrinsic polarizabilities of the atoms. Mueller appears to be the first investigator to recognize the importance of the last factor. The theory has been applied so far only to cubic crystals and isotropic solids because in these cases the symmetry is such that the coulomb field can be taken to be zero. Under hydrostatic pressure the symmetry is unchanged and the coulomb field remains zero but the Lorentz-Lorenz field may change because of the change in density.

There are two principal theoretical relationships relating the index and density, the Lorentz-Lorenz,

$$\frac{\mu^2-1}{\mu^2+1}\left(\frac{1}{\rho}\right)=\alpha_1 \tag{8}$$

and the Drude,

$$(\mu^2-1)/\rho=\alpha_2 \tag{9}$$

where α_1 and α_2 are constants. In deriving the Lorentz-Lorenz equation the local field has been accounted for through the theoretical value $4/\pi 3\ \overline{P}$ where $\overline{P}$ is the polarization of the medium and the change in local field with density is accounted for in the equation. The change in the local field with density has been ignored in the Drude equation.[3]

If α_1 and α_2 are rigorously constants eq (8) and eq (9) may be differentiated to obtain the change of index with density. This was apparently first done by Pockels [39] who obtained the two expressions

$$\rho\frac{\partial\mu}{\partial\rho}=(\mu^2-1)(\mu^2+2)/6\mu \tag{10}$$

$$\rho\frac{\partial\mu}{\partial\rho}=(\mu^2-1)/2\mu \tag{11}$$

corresponding to the Lorentz-Lorenz and Drude formulations respectively. In eq (10) and eq (11) partial derivatives are used to indicate that there may be a change in atomic polarizability which is neglected. Mueller [2, 3] introduced the strain polarizability parameter, λ_0, to evaluate the change in polarizability by means of the relationship,

$$\rho d\mu/d\rho=(1-\lambda_0)\rho\partial\mu/\partial\rho. \tag{12}$$

This relationship follows from considering α_1 and α_2 to be dependent on the polarizability. By using eq (12) in conjunction with eqs (10) and (11) and the experimental values of $\rho\Delta\mu/\Delta\rho$ values of λ_0 have been calculated for both the Lorentz-Lorenz and the Drude formulations. These data are shown in table 2.

Burstein and Smith [1] have proposed that λ_0 is a measure of the degree of homopolar binding. According to Burstein and Smith λ_0 should attain a maximum value for intermediate bonding, i.e., bonding containing appreciable amounts of both ionic and homopolar bonding, and decrease as the bonding becomes either more ionic or more homopolar. The present studies do not agree with this conclusion, the value of λ_0 being largest for the most covalent crystal-diamond. It appears that the conclusions of Burstein and Smith were based upon erroneous data for diamond.

For the glasses, calculated values of λ_0 are also given in table 2. These values show little variation for the three glasses but it is noteworthy that λ_0 data calculated by both the Lorentz-Lorenz and the Drude equations are positive. Previous data on liquids show that λ_0 is positive when computed from the L–L equation but negative when computed from the Drude equation [30]. This behavior in liquids was explained as arising from the change in the local field brought about by compression of the liquids

[3] Krishan and Roy [40] have shown the equivalence of the Lorentz-Lorenz and Drude equations in expressing the frequency dependence of the refractive index and have shown that the Drude expression accounts for the local field by incorporating its effect into the value of the fundamental absorption frequency. However, eq (9) is a simplified version of the generalized Drude equation and is valid only at a single frequency. When written in the form of eq (9) it is implied that the change in the local field with density has been ignored.

and incorporated into a change in the fundamental absorption frequency in the Drude model. This greater change in the local field of the liquids arises from their greater compressibilities.

Ramachandran and Radhakrishnan [41, 6] have shown that the thermal properties of the index of refraction may be understood by considering the change of index with temperature to consist of three independent contributions which they label P, Q, and R. P represents the change arising only from a change in the number of scattering centers and is a pure density effect, Q represents the change in polarizability resulting from the density change, and R consists of the effect of temperature alone on the polarizability. Recognizing that $d\mu/dT=P+Q+R$, the values they derived using the Drude equation are as follows:

$$P=-\gamma\left(\frac{\mu^2-1}{2\mu}\right) \tag{13}$$

$$Q=-\gamma\left(\rho\frac{d\mu}{d\rho}-\frac{\mu^2-1}{2\mu}\right) \tag{14}$$

$$R=\frac{d\mu}{dT}+\gamma\rho\frac{d\mu}{d\rho} \tag{15}$$

where $\gamma=-\frac{1}{\rho}\left(\frac{d\rho}{dT}\right)_P$. Values of $\rho d\mu/d\rho$ they used [41, 6] were evaluated from the elasto-optic constants (eq (3)). The quantities P, Q, and R have been re-evaluated using the same data that Krishnan and Roy used except that experimental values of $\rho\Delta\mu/\Delta\rho$ have been substituted for $\rho d\mu/d\rho$. [There is one further change; it appears that the earlier results were calculated using an erroneous value for the volume expansivity of diamond, 1.3×10^{-5}/°C [41, 6] compared to the correct value, 0.31×10^{-5}/°C [42, 9].] The results are given in table 4. The present data agree reasonably well with the earlier results in most instances, there being slight changes in Q and R resulting from the present values of $\Delta\mu/\Delta\rho$. There is a large change, however, in the results for diamond.

It is also possible to calculate R, which is defined as $(d\mu/dT)_V$, from constant volume data. For a given material the calculations involve finding a temperature at 1 atm where the specific volume is the same as that at 25 °C and an elevated pressure; the refractive indices which pertain for the two different situations may then be used to find R. Such calculations have been made using values of γ and $(d\mu/dT)_P$ as a function of temperature. The original sources for the values of γ and $(d\mu/dT)_P$ for the different solids have been identified in the list of references.[4] Much of the necessary information may be found in the compilation made by Krishnan [6]. The values are given in the column headed R (experimental) in table 4. It can be seen that there is reasonably good agreement between corresponding values of R in the two columns.

[4] BSC 517/645 is known to have the same nominal composition as the glass designated as BSC-2 in reference [8].

TABLE 4. *Analysis of change in refractive index and polarizability for cubic crystals and glasses*

Material	μ_D	$\gamma\times10^5$	$d\mu/dT\times10^5$	$P\times10^5$	$Q\times10^5$	$R\times10^5$	$R\times10^5$ (experimental)	$\left(\frac{V}{\alpha}\frac{\partial\alpha}{\partial V}\right)_T$	$\left(\frac{V}{\alpha}\frac{\partial\alpha}{\partial V}-1\right)_T$	$\left(\frac{V}{\alpha}\frac{\partial\alpha}{\partial V}-1\right)_T\gamma\times10^5$	$\left(\frac{1}{\alpha}\frac{\partial\alpha}{\partial T}\right)_V\times10^5$	$\left(\frac{1}{\alpha}\frac{\partial\alpha}{\partial T}\right)_V\times10^5$ (experimental)
		°C^{-1}	°C^{-1}	°C^{-1}	°C^{-1}	°C^{-1}	°C^{-1}			°C^{-1}	°C^{-1}	°C^{-1}
KBr	1.559	12.0	−3.6	−5.5	1.3	0.6	0.4	0.2	−0.8	−9.4	1.6	0.9
NaCl	1.544	12.0	−3.8	−5.4	2.0	−0.4	−.3	.4	−.7	−7.8	−.7	−.7
LiF	1.392	10.2	−1.3	−3.4	3.4	−1.3	−1.3	1.0	0.0	0.0	−3.8	−3.9
MgO	1.736	3.9	1.6	−2.3	3.5	0.4	0.6	1.5	.5	2.6	0.7	1.0
Diamond	2.417	0.31	1.0	−0.3	0.8	.5	.6	1.7	.7	0.2	.8	0.6
Fused SiO_2	1.458	.15	0.92	−.06	.01	.97	1.0	0.2	−.8	−.1	2.5	2.6
BSC 517/645	1.517	2.0	.17	−.9	.2	.8	.7	.2	−.8	−1.5	1.9	1.5
Plate glass	1.518	1.9	.27	−.8	.2	.9	----------	.3	−.7	−1.4	2.0	----------

For the present purposes where volume and temperature may both be considered as independent variables it appears more desirable to change the analysis slightly as follows: Starting with the Drude relationship (eq (9)) and considering the polarizability α_2 to be a function of V and T, it can be shown that

$$d\mu/\mu=\frac{(\mu^2-1)}{2\mu^2}\left[\frac{1}{\alpha}\left(\frac{\partial\alpha}{\partial T}\right)_V dT+\left(\frac{V}{\alpha}\left(\frac{\partial\alpha}{\partial V}\right)_T-1\right)\frac{dV}{V}\right]. \tag{16}$$

(In eq (16) and the treatment that follows α_2 is written simply as α.) In this expression $\frac{1}{\alpha}\left(\frac{\partial\alpha}{\partial T}\right)_V$ is the pure temperature coefficient of polarizability, $\frac{V}{\alpha}\left(\frac{\partial\alpha}{\partial V}\right)_T$ is the pure volume coefficient of polarizability and the term $\left(\frac{V}{\alpha}\left(\frac{\partial\alpha}{\partial V}\right)_T-1\right)$ represents the total contribution of volume to the change in index. At present the term $\frac{V}{\alpha}\left(\frac{\partial\alpha}{\partial V}\right)_T$ can be evaluated from the constant temperature experiments. To obtain $\frac{1}{\alpha}\left(\frac{\partial\alpha}{\partial T}\right)_V$ the volume is taken to be a function of P and T. Then $dV=\left(\frac{\partial V}{\partial T}\right)_p dT+\left(\frac{\partial V}{\partial P}\right)_T dP$ and using

$\frac{1}{V}\left(\frac{dV}{dT}\right)_P=\gamma$ and $-\frac{1}{V}\left(\frac{dV}{dP}\right)_T=\beta$ eq (16) can be recast in the form

$$\frac{d\mu}{\mu}=\frac{\mu^2-1}{2\mu^2}\left[\frac{1}{\alpha}\left(\frac{\partial\alpha}{\partial T}\right)_V dT+(\gamma dT-\beta dP)\left(\frac{V}{\alpha}\left(\frac{\partial\alpha}{\partial V}\right)_T-1\right)\right]. \quad (17)$$

The value of $V/\alpha(\partial\alpha/\partial V)_T$ determined from eq (16) can be combined with available data on γ and on the temperature variation of index at constant pressure to derive values for $\frac{1}{\alpha}\left(\frac{\partial\alpha}{\partial T}\right)_V$. If the Lorentz-Lorenz equation is used the same expression will be obtained except that the factor $\frac{(\mu^2-1)(\mu^2+2)}{6\mu^2}$ replaces $\frac{\mu^2-1}{2\mu^2}$. This represents only a different scaling factor and in no way affects the relative magnitudes of the terms in the brackets which are of primary interest.

The calculated values of the terms of interest in eq (17) are given in table 4. The volume coefficient of polarizability is seen to be positive in all materials as expected. The positive sign means a decreased polarizability on compression and an increased polarizability on heating arising from the thermal expansion. In the alkali halides the numerical values of the coefficient increase as the anion packing increases. Values for MgO and diamond are the largest in the table, a result consistent with the large interatomic interactions presumed to occur in these materials. The small values for the glasses are to be expected from the smaller interatomic interactions expected for such open structures. The smallest value in the table applies to fused SiO_2 which has the most "open" structure. (The figures in table 4 have been rounded off and this conclusion is not obvious from the data given.) The total volume contribution is given in the next column and these values are generally negative except for diamond and MgO. It is noteworthy that in every case the volume coefficient of polarizability represents an appreciable portion of the total volume effect. It must be concluded that any relationship between index and density which ignores the effect of this contribution to the index can, at best, be only approximately correct. The next column tabulates the total volume term multiplied by the expansivity to permit comparison on an equal basis with values for the temperature coefficients of polarizability given in the next to last column. The temperature coefficients vary in both sign and size with the value apparently decreasing with packing in the alkali halides and being rather large positively in the glasses. There are insufficient data, however, to verify that these conclusions are typical. $\left(\frac{1}{\alpha}\frac{\partial\alpha}{\partial T}\right)_v$ may also be found by substituting values of $(d\mu/dT)_v$ in eq (16). These values are shown in the last column of table 4. Again it may be seen that there is fairly good agreement between corresponding values in the two columns of figures.

With the data given in table 4 it is instructive to consider the change in index resulting from two separate experiments, first an isothermal compression and second an isobaric temperature change. An isothermal compression produces an increase in index in KBr, NaCl, and all the glasses because the predominant effect is an increase in the number of scattering centers per unit volume. The decrease in polarizability with decreasing volume is less than the density effect in these materials. In LiF the index undergoes no change (to 1 kbar) because the density increase and the polarizability decrease exactly balance. In both MgO and diamond the index decreases on compression, the polarizability decrease overbalancing the density increase.

It is of interest to consider the effect of pressures higher than the 1 kbar used here. It appears likely that the volume coefficient of polarizability will increase as the volume decreases because the interatomic interactions should increase in magnitude. In the absence of other effects, this requires that at some elevated pressure the indices of the solids which increased with pressure at low pressures will pass through a maximum value and then decrease at still higher pressures. Further the decrease in index should accelerate at still higher pressures. The pressures required to produce these changes are not obvious but plans are being made to extend these measurements to 10 kb. In this range it appears very probable that a decrease might be expected for LiF. For the other alkali halides a reversal or a decrease in the rate of change of index with density might be expected.

An isobaric temperature increase results in a decrease in indices for KBr, NaCl, and LiF but an increase in indices for MgO, diamond and all the glasses. Although the resultant effects are similar for members in each of the two groups, there are various causes, and it is necessary to consider the details of the process. In KBr the volume expansion causes a decrease in index because the number of scattering centers per unit volume decreases. This effect is great enough to overbalance the increased polarizabilities arising from the increased volume and temperature. In NaCl the temperature coefficient acts in conjunction with the density effect to decrease the index. In LiF there is no total volume contribution and the decrease in index arises solely from the temperature coefficient of polarizability. In both MgO and diamond the index increases because the positive temperature and volume coefficients of polarizability overbalance the negative contribution from the decrease in the number of scatterers with the volume coefficient playing the major role. All the glasses show an increase in index because the comparatively large temperature coefficient of polarizability outweighs the negative effect of the total contribution of change in volume which is nearly as large.

The glasses require further consideration because it is known [8] that the index-temperature relationships of most optical glasses exhibit a minimum in index. The glass BSC–517/645 has such a minimum near −80 °C and although data on plate glass do not appear to be available a minimum may reasonably be expected at some temperature below 25 °C. On the other hand the index of refraction of fused SiO_2 is known to decrease monotonically with decreasing temperature [51,16] despite the reversal of its coefficient of thermal expansion. A reasonably sound explanation of these effects requires data on the two terms $\frac{v}{\alpha}\frac{\partial^2\alpha}{\partial V\partial T}$ and $\frac{1}{\alpha}\frac{\partial^2\alpha}{\partial T^2}$ which are apparently not available at this time but certain conclusions may be of interest until such data are obtained. It might be expected that for normal materials the polarizability arising from pure thermal agitation should decrease at higher temperatures because of increased interaction. However, it is not apparent whether $\frac{\partial\alpha}{\partial T}$ increases or decreases. Data by Radhakrishnan on LiF [49] show that $d\mu/dT$ becomes increasingly negative at higher temperatures. At room temperature this crystal shows a zero volume contribution, and, if it is assumed that this contribution is negligibly small at elevated temperatures, it may be concluded that $\frac{1}{\alpha}\left(\frac{\partial^2\alpha}{\partial T^2}\right)$ is negative. The glasses, however, are not normal solids so that it is not certain that they exhibit a similar behavior. It is known that $\frac{1}{V_0}\left(\frac{\partial^2 V}{\partial T^2}\right)_p$ is positive for the glasses and it is to be expected that $\frac{V}{\alpha}\left(\frac{\partial\alpha}{\partial V}\right)_T$ would increase somewhat at low temperatures because of the closer packing.

In table 4 it is observed that for BSC 517/645 and plate glass that the total volume contributions and the temperature coefficients of polarizability are of opposite signs but nearly equal in absolute values. If either one or both of those quantities changes slightly in the proper direction on lowering the temperature it is clear that the sign of $d\mu/dT$ will reverse. Since this reversal occurs below room temperature in BSC 517/645 and is expected in a similar temperature range for plate glass, it is probable that the temperature coefficient of polarizability decreases with decreasing temperature in these glasses in contrast with the opposite behavior observed in LiF. The situation in fused SiO_2 is somewhat different in that $\frac{1}{\alpha}\left(\frac{\partial\alpha}{\partial T}\right)_v$ is at least ten times as great as the total volume effect although they are of opposite sign. In this situation a small change in either quantity will be insufficient to reverse the sign of $d\mu/dT$. In addition when the expansivity of fused SiO_2 becomes negative both the volume term and $\frac{1}{\alpha}\frac{\partial\alpha}{\partial T}$ are positive and cannot cancel. It may be noted that the interpretation here is similar to that advanced by Prod'homme [52] for the anomalous temperature-index behavior in optical glasses but is somewhat more detailed. It appears that the positive value of $d\mu/dT$ in optical glasses arises from the comparatively large temperature coefficient of polarizability coupled with the low coefficient of thermal expansion. Since these quantities are not common to all glasses [52] it appears that they must be attributed to the silica network.

The authors are indebted to Harry B. Williams of the National Bureau of Standards for his great help in the preparation of specimens. The authors also thank Edward N. Farabaugh and William S. Brower of the National Bureau of Standards for their help in the orientation of the uniaxial crystals.

6. References

[1] E. Burstein and P. L. Smith, Proc. Ind. Acad. Sci **A28,** 377 (1948).
[2] H. Mueller, Phys. Rev. **47,** 947 (1935).
[3] H. Mueller, Physics **47,** No. 6, 179 (1935).
[4] H. N. Ritland, J. Am. Ceram. Soc. **38,** 86 (1955).
[5] C. Weir, S. Spinner, I. Malitson, and W. Rodney, J. Res. NBS **58** No. 4, 189 (1957) RP2751.
[6] R. S. Krishnan, Progress in Crystal Physics, Volume I (Interscience Publishers, New York, London, 1958).
[7] M. A. Jeppensen, J. Opt. Soc. Am. **48** No. 9, 629 (1958).
[8] (Thermal expansion and du/dT data on BSC 517/645)—F. A. Molby, J. Opt. Soc. Am. **39,** No. 7, 600 (1949).
[9] (du/dT data on diamond)—G. N. Ramachandran, Proc. Ind. Acad. Sci. **A25,** 266 (1947).
[10] R. M. Waxler and C. E. Weir, J. Res. NBS **67A** (Phys. and Chem.) No. 2, 163 (1963).
[11] (Refractive index and du/dT data on KBr)—R. J. Spindler and W. S. Rodney, J. Res. NBS **49** No. 4, 253 (1952) RP2301.
[12] (Refractive index data on NaCl)—F. Kohlrausch, Praktische Physik **II** B. G. Teubner, Leipzig, 528 (1943).
[13] (Refractive index data on LiF)—L. W. Tilton and E. K. Plyler, J. Res. NBS **47** No. 1, 25 (1951) RP2223.
[14] (Refractive index data on diamond)—F. Peter, Z. Phys. **15,** 358 (1923).
[15] (Refractive index data on MgO)—R. E. Stephens and I. H. Malitson, J. Res. NBS **49** No. 4, 249 (1952) RP2360.
[16] (Refractive index data on quartz, and thermal expansion and du/dT data on fused silica)—R. B. Sosman, The Properties of Silica, (Chem. Cat. Co. N.Y., 1927).
[17] (Refractive index data on Al_2O_3)—R. W. Kebler, Optical Properties of Synthetic Sapphire (Linde Co., N.Y.).
[18] (Refractive index data on fused silica)—J. B. Austin, Physics **3** 240 (1932).
[19] (Refractive index data on BSC 517/645)—R. E. Stephens and W. S. Rodney, J. Res. NBS, **52** No. 6, 303 (1954) RP2504.
[20] (Refractive index data on plate glass)—E. Hamilton, R. Waxler and J. M. Nivert, Jr., Optical Glass Technology Development, NBS Report No. 5440 (1957).
[21] (Compression data on KBr, NaCl and LiF)—P. W. Bridgman, The Physics of High Pressure (G. Bell & Sons, Ltd., London 1949).
[22] (Compression data on quartz)—P. W. Bridgman, Am. J. Sci. Fifth series **15** No. 88, 287 (1928).
[23] (Compression data on Al_2O_3)—P. W. Bridgman, Proc. Am. Acad. Arts Sci. **68,** 27 (1932).
[24] (Compression data on fused silica)—P. W. Bridgman, Am. J. Sci. **10,** 359 (1925).
[25] (Compression data on diamond and plate glass)—L. H. Adams and E. D. Williamson, J. Frank Inst. **195,** 475 (1923).

[26] (Compression data on MgO)—C. E. Weir, J. Res. NBS **56** No. 4, 187 (1956) RP2666.
[27] S. Spinner, J. Am. Cer. Soc. **37** [5], 229 (1954).
[28] F. A. Jenkins and H. E. White, Fundamentals of Optics (McGraw-Hill Book Company, Inc., New York, Toronto, London, 1950).
[29] E. S. Jog, Jour. Ind. Inst. Sci. **39A,** 101 (1957).
[30] R. M. Waxler, C. E. Weir, and H. W. Schamp, Jr., J. Res. NBS **68A** (Phys. and Chem.) No. 5, 489 (1964).
[31] F. Pockels, Ann. Phys. **37,** 151 (1889).
[32] D. F. Gibbs and G. J. Hill, Phil. Mag. **8,** 367 (1963).
[33] C. Schaefer and H. Nassenstein, Z. Naturforsch. [A] **8,** 90 (1953).
[34] K. Vedam, Proc. Ind. Acad. Sci. [A] **31,** 450 (1950).
[35] F. Pockels, Ann. Phys. Chem. **37** (4), 269 (1889).
[36] R. M. Waxler and A. Napolitano, J. Res. NBS **59** No. 2, 121 (1957) RP2779.
[37] R. M. Waxler, Glass Ind. **34,** 258 (1953).
[38] S. Spinner, personal communication.
[39] F. Pockels, Ann. d. Phys. **7,** 745 (1902).
[40] K. S. Krishnan and S. K. Roy, Phil. Mag. **43,** 1000 (1952).
[41] G. N. Ramachandran and T. Radhakrishnan, Phil. Mag. **43,** 317 (1952).
[42] (Thermal expansion data on diamond)—R. S. Krishnan, Proc. Indian Acad. Sci. **A24,** 33 (1946).
[43] (Thermal expansion data on KBr)—R. Srinivasan, J. Indian Inst. Sci. **A37,** 232 (1955).
[44] (Thermal expansion data on NaCl)—R. M. Buffington and W. M. Latimer, J. Amer. Chem. Soc. **48,** 2305 (1926).
[45] (Thermal expansion data on LiF)—A. Eucken and W. Dannöhl, Z. Electrochem. **40,** 814 (1934).
[46] (Thermal expansion data on MgO)—M. Durand, Physics **7,** 297 (1936).
[47] (Thermal expansion data on fused silica)—K. Scheel and W. Heuse, Verh. Deutsch. Physik. Ges. **16** 1 (1914).
[48] (du/dT data on NaCl)—F. J. Micheli, Arch. Sc. Phys. Nat. **13,** 217 (1902).
[49] (du/dT data on LiF)—T. Radhakrishnan, Proc. Indian Acad. Sci. **A31,** 224 (1950).
[50] (du/dT data on MgO)—T. Radhakrishnan, Proc. Indian Acad. Sci. **A33,** 22 (1951).
[51] (du/dT data on fused silica)—F. Rinne, Neues Jahrb. Mineral. Beil. Bd. **39,** 388 (1914).
[52] L. Prod'homme, Phys. and Chem. of Glasses **1** No. 4, 119 (1960)

(Paper 69A4–352)

JOURNAL OF RESEARCH of the National Bureau of Standards—A. Physics and Chemistry
Vol. 69A, No. 4, July–August 1965

Crystallization Kinetics and Polymorphic Transformations in Polybutene-1

J. Powers, J. D. Hoffman, J. J. Weeks, and F. A. Quinn, Jr.

(April 1, 1965)

When subcooled from the melt to any temperature between about 90 to 110 °C, polybutene-1 transforms at a readily measurable rate to a crystalline phase denoted "form 2," which is typically spherulitic. The kinetics of this process have been measured by optical and dilatometric techniques. The results are consistent with the concepts that the initiation is heterogeneous, that the initiation is followed by spherical growth (Avrami $n=3$), and that the growth rate is nucleation controlled. Values are obtained for the surface free energies and related quantities that are consistent with crystallization by chain folding: $\sigma=7.2$ erg/cm^2 or 7.2 mJ/m^2, $\sigma_e=15.5$ erg/cm^2 or 15.5 mJ/m^2, and work of chain folding $q=1.7\times10^{-13}$ erg/fold. (For comparison, q is 2.1×10^{-13} erg/fold for polyethylene.) The work of chain folding of polybutene-1 is also compared with that of polychlorotrifluoroethylene, and it is shown that an increase of q is connected with an increase of equilibrium melting temperature. Crystal form 2 subsequently converts slowly near room temperature to a crystalline phase denoted "form 1" of different helicity and density, and the rate of this crystal-crystal transformation is also studied. The Avrami parameter for the form 2→form 1 process is $n=2$. The process appears to be nucleation controlled. It is shown that form 1 is, everywhere below its melting point, the stable form. The equilibrium melting temperature for form 2 is estimated to be about 128 °C, and for form 1 about 141 °C. A degree of crystallinity scale based on specific volume is established. The degree of crystallinity of form 2 is about 52 percent, and after conversion to form 1, the crystallinity is about 77 percent.

1. Introduction

Many polymers exhibit two or more polymorphic crystalline forms. The existence of three crystalline forms of polytetrafluoroethylene [1, 2, 3],[1] which under conditions approaching equilibrium are bounded by sharp phase transitions near 20 and 30 °C, is perhaps the most familiar example. In the particular case just cited, the phase transitions are first-order crystal-crystal transitions, the transition temperatures having a truly thermodynamic significance in the same sense as does the melting point. Another example of a first-order crystal-crystal transition is the familiar rotational transition that occurs in the n-paraffins with chains containing 22 to 44 carbon atoms.

A change of phase of quite a different class than that described above can occur in polymers and molecular crystals generally. For purposes of clarity, these are denoted "transformations" in this paper. These phase changes occur under conditions departing considerably from equilibrium, and take place over an extended temperature range. A typical example is the formation of a crystalline phase from the subcooled liquid phase over a range of temperature. In this paper, the rate of transformation of the subcooled liquid phase of polybutene-1 to a crystalline form designated "form 2" is studied in detail in the range of 90 to 110 °C. This process occurs with the formation of typical spherulites. A crystal-crystal transformation in the same general class also occurs in polybutene-1. In this transformation, form 2 crystal converts to form 1 crystal at variable but measurable rates between 10 and 60 °C. This crystal-crystal transformation is studied. As noted below, this transformation involves a change in the characteristics of the helix conformation. The melting points of the two crystalline forms are investigated. Natta [4] has given a general discussion of the origin of different crystalline phases in polymeric systems.

Earlier investigations of the transformation of form 2 to form 1 have revealed a number of facts of interest. The form 2 → form 1 transformation rate is accelerated by uniaxial orientation or the application of hydrostatic pressure [5, 6]. X-ray diffraction data indicate that the polybutene-1 chain in form 2 assumes the conformation of an 11_3 helix [7] and in form 1 a 3_1 helix [8]. A third crystalline form [5, 9] has been found on precipitating polybutene-1 from solution. This latter form is reported to be stable over the period of at least several months if a temperature of roughly 100 °C is not exceeded [10]. The helicity of the polybutene-1 chain in this form has not yet been reported.

Volume dilatometry was used to study both the isothermal rate of formation of form 2 from the subcooled liquid, and the kinetics of the ensuing transformation of form 2 to form 1. Approximate melting points of the form 2 and form 1 polymorphs were also determined dilatometrically. Dilatometric data were complemented by nucleation and growth-rate measurements carried out on a hot stage microscope. Microscopical data help to elucidate the type of nucleation mechanism, the morphology of polycrystalline entities, and the rate of growth of polycrystalline aggregates as the subcooled polymer

[1] Figures in brackets indicate the literature references at the end of this paper.

liquid transforms to the crystalline form 2 at a given temperature below the polymer melting point.

2. Experimental Procedure

2.1 Sample

The material used in this study was furnished by the Phillips Petroleum Company and was labeled Butene-1 (11272–38–1). Part of the material was used as received. A second portion was placed in a soxhlet extractor and left in contact with boiling ether (T_b=35 °C) for 28 days. The initial weight of the latter material was 6.00 g; the weight of the residue after extraction was 5.89 g and that of the extracted material 0.11 g.

The intrinsic viscosities of the two samples were measured in *n*-nonane at 80 °C. Molecular weights were calculated from intrinsic viscosity data using the Krigbaum-Kurz-Smith relation [11]. (Professor Krigbaum has informed us of an error in the equations as published. The negative exponent in eqs (10) and (11) of reference [11] should read 5 rather than 3. The corrected form of eq (11) is $[\eta]=5.85\times10^{-5}M_w^{0.80}$.) Intrinsic viscosity data and results are given in table 1.

TABLE 1. *Intrinsic viscosity data and molecular weights*

Polybutene-1	$[\eta]$, dl/g	M_w
As received	1.785	399,000
Ether-extracted	1.849	412,000

2.2. Dilatometry

Small amounts of sample (approximately 0.5 g) were vacuum molded and then sealed in glass dilatometers with mercury as the confining liquid. The dilatometers were similar to those described by Bekkedahl [12] although constructed on a smaller scale to achieve more rapid thermal equilibrium. Tru-bore tubing (1 mm i.d.) was used in constructing the dilatometers and a correction was applied for variation in bore diameter.

Three types of dilatometer runs were made. In the first type, the samples were crystallized under specified conditions to obtain either form 1 or form 2, and the material warmed quite slowly. Here the objective was to obtain reasonably reliable melting points for the two forms. In the second type of dilatometer run, the objective was to obtain specific volume versus temperature data on forms 1 and 2 under conditions such that the degree of crystallinity did not change appreciably with temperature. This was accomplished by making the crystal form required, and measuring the specific volume curve using fairly rapid warming. In the third type of run, crystallization was carried out isothermally, and the decrease of specific volume studied as a function of time. In this case the objective was to establish the shape of the isotherms and the kinetics of the bulk crystallization process.

The melting point of form 1 for a specimen crystallized near room temperature for a period of 1 week to several months lies in the range T_m=128° to T_m=132 °C when the melting is carried out at a moderate rate. A run of this general type is shown in figure 1. A higher melting point for form 1 is easily attained. If in the warming run the specimen is held overnight just below the melting temperature, a melting point as high as T_m=137 °C is found.

Form 2 is produced when the polymer is crystallized from the melt in the vicinity of 90 to 100 °C. For a specimen crystallized 4,000 min at 100 °C, fairly rapid melting gave T_m 120 °C. When the specimen crystallized at a higher temperature (112 °C), a melting point of 122 °C was found.

It has been established that the equilibrium melting temperature of a polymer, T_m^0, is somewhat above the highest melting point actually observed even in a very slow melting run. This occurs because the lamellar crystals are thin. A full discussion has been given in a recent review [13]. It has been found that T_m^0 is usually roughly 6 °C above the melting point found in a moderately slow warming run of the type used here.[2] Accordingly, we would estimate that T_m^0 is 128 ±2 °C for form 2. By similar reasoning, it is estimated that T_m^0 is 141 ±2 °C for form 1.

The specific volume data used for the degree of crystallinity calculations are shown in figure 1. Form 2 was produced by subcooling the melt to 100 °C, and allowing the sample to remain at that temperature for 3 days. The sample was then quenched to 25 °C, and the specific volume data obtained with fairly rapid heating. Prolonged storage below 40 °C was avoided in order to prevent a significant conversion of form 2 to form 1. Similarly, prolonged storage at higher temperatures had to be avoided to prevent additional conversion of subcooled liquid to form 2. Form 1 was produced by subcooling a specimen from the melt to room temperature and storing for 1 week. This allowed the sequences liquid→form 2 and form 2→form 1 to take place. The specific volume data were then obtained with fairly rapid warming. The data are shown in figure 1.

2.3. Hot Stage Microscopy

A thermistor was attached to a standard Kofler hot stage, and the sample temperature was monitored by measuring the resistance of the thermistor with a Wheatstone bridge circuit. The thermistor was calibrated by a previous direct measurement of the temperature inside a duplicate sample using a copper-constantan thermocouple and a precision potentiometer. The temperature was known to within ±0.2 °C.

The samples were first melted by heating to between 160 and 180 °C on a Kofler hot bench and then rapidly transferred to the surface of the hot

[2] If very slow warming is used, the observed melting point approaches to within about 4 °C of T_m^0.

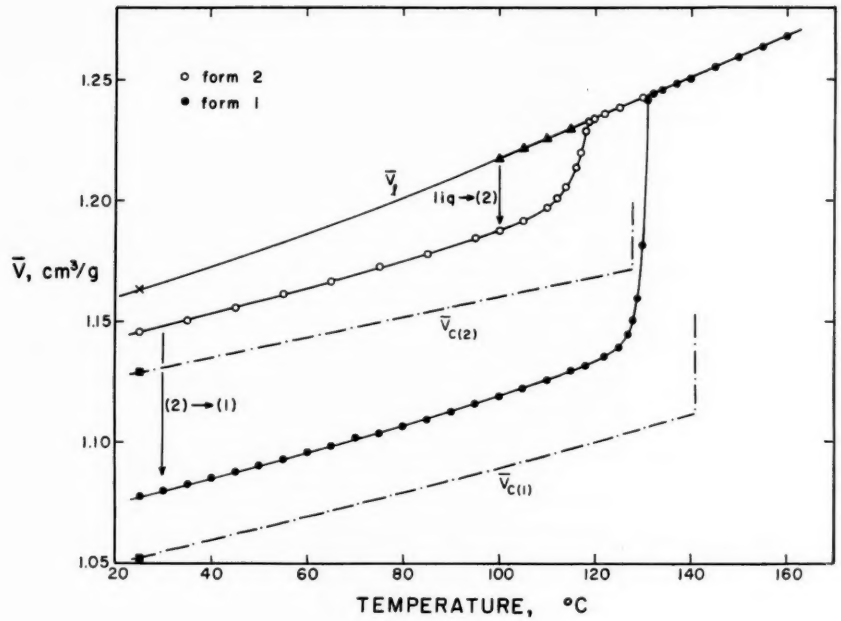

FIGURE 1. *Specific volume-temperature curves for two polybutene-1 polymorphs ("as received" material).*

Form 1 crystallized at 25 °C, form 2 at 100 °C. Data obtained under conditions of fairly rapid warming.
▲, Points obtained on liquidus curve by subcooling.
■, X-ray specific volume of pure crystal of form 1 and form 2 at 25 °C.
X, Derived value of subcooled liquidus at 25 °C.
— · —, Estimated value of pure crystal specific volume for forms 1 and 2, ($\bar{V}_{c(1)}$ and $\bar{V}_{c(2)}$)

stage. The process of crystallization was characterized by photomicrographs taken at time intervals appropriate for the particular temperature of the transformation.

The diameter of each spherulite was measured along two orthogonal directions with a comparator whose precision was 1 μ. Magnification was computed from measurements of a micrometer slide whose smallest division was 0.01 mm. The slide was photographed with the same objective-ocular combination as was used for the spherulites.

3. Results

3.1. Dilatometric Observations of Rate Effects

The isothermal crystallization time plots (fig. 2) at various temperatures show two ranges of different behavior. The upper temperature range (90 to 110 °C) displays a marked rate-dependence on temperature, while the lower range (10 to 60 °C) displays considerably less dependence. Comparison of crystallization half-time data (table 2) affords a quantitative means of characterizing the two regions. The half times for the "as received" polybutene-1 samples range from 3.5 min at 90 °C to 2200 min at 110 °C for the upper range, while for the lower

TABLE 2. *Comparison of isothermal crystallization rate half-times ($t_{1/2}$) for "as received" and for ether-extracted polybutene-1 as a function of temperature*

Temperature	$t_{1/2}$ minutes	
	As received	Ether-extracted
°C	Phase transformation liquid→form 2	
110	2200	1400
105	170	100
100	26	18
95	8	6
90	3.5	3
	Form 2→form 1	
40	3900	3750
35	2400	2600
30	1750	------
20	1400	1600
10	1475	------

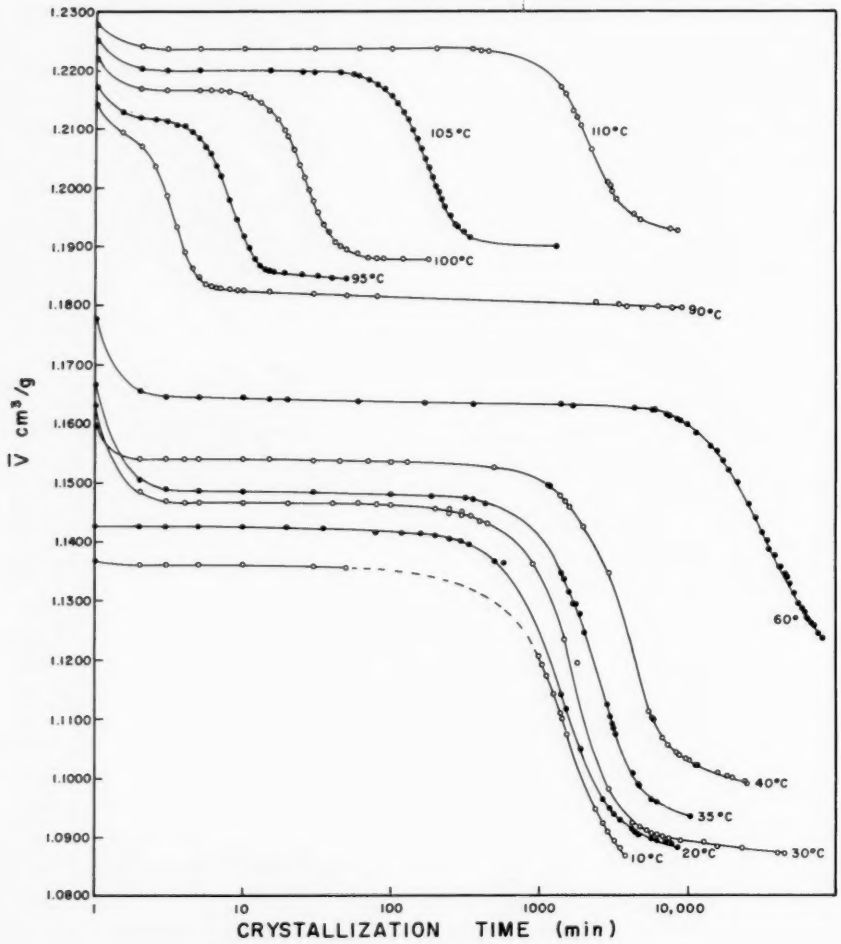

FIGURE 2. *Isothermal specific volume-time plots for "as received" polybutene-1.*

(a) Upper curves (90–110 °C) supercooled liquid→form 2.
(b) Lower curves (10–60 °C) form 2→form 1.

region the half-times are 1400 min at 20 °C to 3900 min at 40 °C. The corresponding half times for the ether-extracted sample are 3 min at 90 °C to 1400 min at 110 °C for the upper region, and for the lower region, 1600 min at 20 °C and 3750 min at 40 °C.

It has already been noted that polybutene-1 exhibits two melting points (fig. 1). Which melting point is found depends on the temperature range in which the sample is crystallized. If crystallized in the upper range (90 to 110 °C), the material melts between 118 and 122 °C, and if crystallized and stored in the lower range (10 to 40 °C), the sample melts between 128 and 132 °C for relatively slow heating rates.[3] Thus, in line with Boor and Mitchell's [14] report of similar melting points, the lower melting form is identified as Natta's form 2 and the higher melting form as his form 1. Since the specific volumes (fig. 2) on the induction portions of the isothermal crystallization curves have the same values as those of the liquidus line (fig. 1) in the range 90 to 110 °C, the transformation in this range therefore represents a subcooled liquid→crystal (form 2) change. For the lower region (10 to 60 °C) the specific volumes on the induction part of the crystallization curve have values lower than those of the liquidus curve in the corresponding

[3] For a given crystal form, a higher melting point is obtained the higher the transformation temperature.

region (fig. 1).[4] The lower region change represents a crystal→crystal transformation with form 2 changing into the more stable form 1. This point will be discussed further in section 4.3.

3.2. Degree of Crystallinity

The degree of crystallinity of form 1 was calculated from

$$\chi_1 = \frac{\overline{V}_l - \overline{V}_s}{\overline{V}_l - \overline{V}_{c(1)}} \quad (1)$$

where $\overline{V}_l$ represents the specific volume of the liquid phase, $\overline{V}_s$ the specific volume of the sample, and $\overline{V}_{c(1)}$ the specific volume of the pure form 1 crystal phase (see fig. 1). In a similar manner, the degree of crystallinity of form 2 was calculated from

$$\chi_2 = \frac{\overline{V}_l - \overline{V}_s}{\overline{V}_l - \overline{V}_{c(2)}} \quad (2)$$

where $\overline{V}_{c(2)}$ represents the specific volume of the pure form (2) crystal. As has been noted many times, for example in [15], these expressions depend on the assumption that the volumes of the liquid and crystalline phases are additive.

In the present case the known quantities in eqs (1) and (2) are $\overline{V}_s$ at any desired temperature, $\overline{V}_{c(1)}$ and $\overline{V}_{c(2)}$ at 25 °C from x-ray data, and $\overline{V}_l$ at 100 °C. The situation is then that at 25 °C, $\overline{V}_s$ and $\overline{V}_{c(1)}$ or $\overline{V}_{c(2)}$ are known, but $\overline{V}_l$ is not, while at 100 °C, $\overline{V}_s$ and $\overline{V}_l$ are known, but $\overline{V}_{c(1)}$ or $\overline{V}_{c(2)}$ are not. The value of $\overline{V}_l$ at 25 °C might be obtained by downward extrapolation of the liquidus data, but this procedure is rather inaccurate because the supercooled liquidus often shows curvature. Accordingly, we proceeded by developing a simple method to obtain $\overline{V}_{c(2)}$ at 100 °C. Given this, χ_2 and $\overline{V}_l^{25}$ can readily be calculated using eq (2). Then χ_1 can be obtained using eq (1) with the value of $\overline{V}_l^{25}$ obtained from the form 1 calculation, and the known values of $\overline{V}_{c(1)}^{25}$ and $\overline{V}_s$ for form 1.

The method for obtaining $\overline{V}_{c(2)}^{100}$ for form 2 is now given. On the basis of the additivity of the volumes of the liquid and crystalline phases [15], it is readily shown that

$$(\overline{V}_l^{100} - \overline{V}_s^{100})\Delta T\alpha_l^{100} - (\overline{V}_l^{100} - \overline{V}_s^{100})(\overline{V}_c^{100} - \overline{V}_c^{25}) = \Delta T(\alpha_l^{100} - \alpha_s^{100})\overline{V}_l^{100} - \Delta T(\alpha_l^{100} - \alpha_s^{100})\overline{V}_c^{100} \quad (3)$$

where $\overline{V}_c^{100}$ refers to $\overline{V}_{c(2)}^{100}$ and $\alpha = d\overline{V}/dT$. It is assumed that there is no curvature in $\overline{V}_{c(2)}$ between 25 and 100 °C. The quantity ΔT is 75 °C in the present case, but other temperature intervals could be chosen. In eq (3), the quantities α_l^{100} and α_s^{100} are known, as are all the other quantities except $\overline{V}_{c(2)}^{100}$. Given $\overline{V}_{c(2)}^{100}$ as calculated by eq (3), it is a simple matter to calculate χ_2 at 100 °C using eq (2). Then assuming χ_2 is constant with temperature, $\overline{V}_l$ can be calculated at 25 °C using eq (2).

The above method should only be applied where the $\overline{V}_s$ data are nearly linear in the temperature range chosen if the sample is thought to be highly crystalline. This condition is not met by the data on form 1. The data on form 1 imply more curvature in $\overline{V}_{c(1)}$ than is allowable for this method to be accurately applicable.

The x-ray data used to estimate the densities of pure form 1 and form 2 are collected in table 3.

TABLE 3. *Crystallographic data for polybutene-1 polymorphs*

Polymorph	Crystal unit cell	Unit cell parameters, Å			Crystal density	Chain conformation
		a	*b*	*c*		
					g/cm³	
Form 1	Rhombohedral [17,18]	17.7	17.7	6.50	0.9507	3_1
Form 2	Tetragonal [a] [19]	[b] 14.89	14.89	20.87	[c] 0.886	11_3
	Tetragonal [a] [7]	14.85	14.85	20.6	0.90	11_3

[a] Unit cell contains four polymer chains.
[b] The thickness of a monomolecular layer is 7.44$_3$ Å on the (100) growth plane.
[c] Recalculated.

The results of the degree of crystallinity calculations are shown in table 4. The probable error in the degree of crystallinity is estimated to be about 4 percent.

The liquidus value obtained at 25 °C is slightly above (about 0.009 cm³/g) that obtained by a linear extrapolation of the actual liquidus data in the 100 to 160 °C range. This is normal behavior. The $d\overline{V}/dT$ values obtained for the pure crystal for forms 1 and 2 are in the usual range for high polymers. Note that $\alpha_{c(1)}$ depends on temperature.

The results listed in table 4 may be interpreted as follows. The subcooled liquid is converted to form 2 to a maximum observable extent of about 52 percent. The conversion is slow at high temperatures, but below 90 °C the transformation becomes so fast that the maximum conversion rate cannot be measured. Hence form 2 appears straightaway to practically its full extent in a sample quenched from the melt to room temperature. Form 2 then proceeds to slowly convert to form 1 at a rate which is a maximum near room temperature. After the form 2→form 1 transformation has essentially stopped, the mass fraction that is crystalline is about 77 percent. This together with other evidence implies that practically all of form 2 converts into form 1, and further implies that some small amount of the remanent subcooled liquid crystallizes during the form 2→form 1 transformation.

The above conclusions are consistent with infrared and x-ray diffraction data that initially show only absorption phenomena characteristic of form 2 after polybutene-1 is cooled from above its melting point to room temperature, and only form 1 after prolonged storage at the same temperature.

[4] The method by which the supercooled liquidus curve was established at low temperature is discussed subsequently.

TABLE 4. *Degree of crystallinity*

Form 2	
Input data	$\bar{V}_l^{100}=1.2175$ cm³/g
	$\bar{V}_c^{100}=1.1878$ cm³/g
	$\bar{V}_c^{25}=1.1455$ cm³/g
	$\bar{V}_l^{25}=1.1289$ cm³/g ($\rho=0.886$ g/cm³, x ray)
	$\Delta T=75$ °C
	$\alpha_l^{100}=8.07\times10^{-4}$ cm³ g⁻¹ deg⁻¹
	$\alpha_c^{100}=6.05\times10^{-4}$ cm³ g⁻¹ deg⁻¹
Results	$\bar{V}_c^{100}=1.1602$ cm³/g
	$\chi_2=0.518$
	$\bar{V}_l^{25}=1.1634$
	$\alpha_{c(2)}=4.17\times10^{-4}$ cm³ g⁻¹ deg⁻¹
Form 1	
Input data	$\bar{V}_l^{25}=1.1634$ cm³/g
	$\bar{V}_c^{25}=1.0772$ cm³/g
	$\bar{V}_c^{25}=1.0518$ cm³/g ($\rho=0.9507$ g/cm³, x ray)
Results	$\chi_1=0.772$
	$\alpha_{c(1)}=4.51\times10^{-4}+8.16\times10^{-7}\ T$ (°C)

Boor and Mitchell [14] interpret their torsional damping data as indicating that but little crystallization of liquid occurs during the form 2→form 1 transformation. Our results imply that some amorphous material does in fact crystallize during the 2→1 process. Zannetti, Manaresi, and Buzzoni [5] have studied the polymorphic behavior of polybutene-1 as a function of temperature and pressure by means of x-ray diffraction and density techniques. Their density data are stated to imply a degree of crystallinity of between 40 and 50 percent for form 1. Wilski and Grewer [16] find using their specific volume data that form 1 exhibits a degree of crystallinity of $\chi_1=0.76$, which is very close to that found in the present study.

Wilski and Grewer's calorimetric data [16] may be interpreted to mean that χ_2 is close to 0.49 (see footnote in table 7), which is in good agreement with our value of 0.52. Their specific volume data for form 2, when recomputed using our $\bar{V}_{c(2)}$ and $\bar{V}_l$ values, indicate that χ_2 is 0.47. Wilski and Grewer assumed in their paper that the degree of crystallinity of form 2 was the same as that of form 1, i.e., 0.76. Our interpretation of their calorimetric data, and our dilatometric data, indicates that χ_2 is actually nearer to 0.5.

By crystallizing polybutene-1 under 800 bars pressure, we have succeeded in attaining a degree of crystallinity of over 80 percent by the dilatometric method (form 1). This is comparable to the degree of crystallinity obtained by the dilatometric method for well annealed samples of polyethylene, which commonly yield χ values near 0.80 to 0.85 (see for example reference [13]). In the case of polybutene, the true degree of crystallinity is probably considerably higher than 0.8, because voids artificially lower χ. For example, a careful analysis of heat capacity data, which is insensitive to the effect of voids, yields a χ value in excess of 0.95 for a well-annealed polyethylene specimen identical to that which gives $\chi=0.80$ by the dilatometric method [13]. The implication is that the polybutene-1 studied here may be regarded as a highly crystalline polymer that does not exhibit any serious degree of atacticity.

3.3. Avrami Parameter

The Avrami equation is commonly used to fit and to interpret isothermal crystallization-time plots and may be represented as [20]

$$\frac{h_t-h_\infty}{h_0-h_\infty}=\exp\ (-Kt)^n, \tag{4}$$

where h_t represents the mercury height at time t, h_0 the height during the induction period, h_∞ the height after the isotherm has leveled off, and K is a parameter which includes growth rate, nucleation rate and temperature terms. The parameter n is a dimensionless number ranging between 1 and 4. The value of n can under appropriate circumstances be interpreted as signifying the type of initiation and the dimensionality of the developing crystalline phase.

The parameter n was calculated from the differentiated form of eq (5)

$$n=\frac{t(dh_t/dt)}{(h_\infty-h_t)\left\{\ln\left[\dfrac{h_0-h_\infty}{h_t-h_\infty}\right]\right\}}. \tag{5}$$

The average magnitude of n was not appreciably affected by the choice of h_∞. Results are shown in table 5. The estimated uncertainties noted in table 5 are average deviations from the mean values of n.

3.4. Seeding Experiment

Large numbers of form 1 nuclei were prepared by heating a form 1 specimen to a temperature near the melting point so that the specific volume was just below the liquidus. Then the specimen was cooled to 100 °C where form 2 ordinarily grows from the melt and the crystallization was allowed to proceed. The melting curve of the specimen was then obtained. It was found that the newly formed crystals melted in the same range as form 2 obtained without seeding.

TABLE 5. *Avrami parameter for polybutene-1 transformations*

Temperature	Subcooled liquid→form 2	n
°C		
110		2.9±0.3
105		3.2±0.2
100		3.3±0.4
95		3.8±0.4
	Form 2→form 1	
40		1.8±0.2
35		2.2±0.3
30		2.2±0.6
20		1.5±0.5
10		2.0±0.3

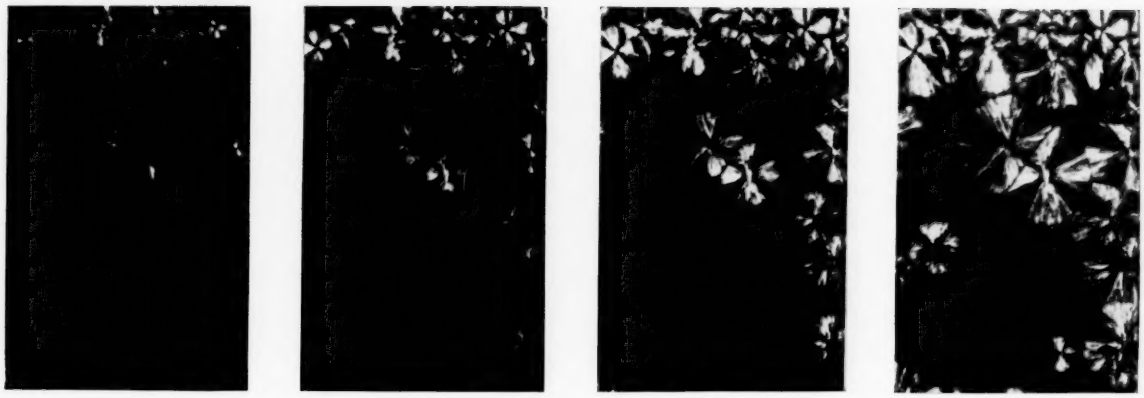

FIGURE 3. *Photomicrographs showing growth sequence for polybutene-1 spherulites crystallized at 90.2 °C.*
Specimen cooled from $T_1 = 160$ °C. Magn. 108×. Crossed polaroids.

This result is to be expected from the results on the kinetics of crystallization: the growth rate of form 1 at 100 °C is by all accounts exceedingly slow, while form 2 nucleates itself and grows at a measurable rate at this temperature.

3.5. Microscopical Observations

Observations of spherulitic nucleation and growth rates were made over a temperature range of approximately 90 to 107 °C. Above 107 °C, crystallization occurred too slowly to be feasible in terms of time and temperature control of the equipment. Below 90 °C, crystallization occurred too rapidly to be followed. Thus, the development of spherulites could not be studied at low temperatures where the growth rate is diffusion controlled. Some isolated observations were made on spherulitic films formed at 105 °C and kept at room temperature for several months. These were compared with spherulites freshly prepared at the same temperature. No differences in optical appearance as regards texture or character of the birefringence could be discerned between the two sets of spherulites.

All spherulites observed displayed a coarse fibrillar texture with some tendency for random mixing of positively and negatively birefringent areas (figs. 3 and 4). Their appearance is thus similar to the mixed form polypropylene spherulites reported by Padden and Keith [21]. Spherulites nucleated and grown at 90 °C (fig. 3) displayed a more typical structure (i.e., the maltese cross is easily distinguished) than did those formed at 107 °C (fig. 4). No ringed or other types of spherulites with well developed optical patterns, however, were observed in this study. Since almost all spherulites first appeared over a narrow time interval, we conclude that the dominant mode of initiation is heterogeneous in origin. Some growth sequences (center left fig. 3, compare 5 min with 3 min photomicrograph) showed a few spherulites appearing at later times.

FIGURE 4. *Photomicrographs showing growth sequence for polybutene-1 spherulites crystallized at 106.7 °C.*
Specimen cooled from $T_1 = 160$ °C. Magn. 108×. Crossed polaroids.

These spherulites are almost certainly pseudohomogeneous as defined by Hoffman and Lauritzen [22].

Spherulite radius-time plots were prepared from the photomicrographs, and radial growth rates were calculated as $G = dr/dt$, where r is the radius. The results are shown in table 6. Except when the spherulites impinged, the radius-time plots were linear, showing that polybutene–1 exhibits typical lineal growth. Each G value is an average for several spherulites. The radius-time line generally intersected the time coordinate at a positive value, indicating the existence of a short induction time, τ_1. This is typical of spherulitic growth in many polymers.

The growth rate data in table 6 indicate that the spherulitic growth process has a negative temperature coefficient, i.e., the growth is slower the higher the growth temperature. This type of temperature

TABLE 6. *Polybutene-1 isothermal spherulite growth rate* [a]

(Supercooled liquid→form 2)

Growth temperature	Radial growth rate, $G=dr/dt$
°C	cm/sec
90.0	3.38×10^{-5}
90.2	3.02×10^{-5}
90.2	2.88×10^{-5}
96.0	1.98×10^{-5}
96.0	1.39×10^{-5}
100.0	0.604×10^{-5}
101.6	0.357×10^{-5}
101.6	0.328×10^{-5}
105.0	0.196×10^{-5}
106.7	0.106×10^{-5}

[a] The specimens were first heated to $T_1=160$ °C and then cooled to the growth temperature.

dependence implies that the growth step is nucleation rather than diffusion controlled.

4. Discussion

4.1. Subcooled Liquid→Form 2 Transformation

The liquid→form 2 process can readily be understood in terms of current concepts of spherulitic growth with chain folding. These concepts have been discussed in a recent review [13]. Surface free energies may be calculated from spherulitic growth data for the liquid→form 2 process by use of the eqation [13, 22, 23][5]

$$G=G_0 \exp(-\Delta H^*/RT) \exp[-K_g/T^2(\Delta T)] \quad (6)$$

where K_g is $4b_0\sigma\sigma_e(T_m^0)^2/(\Delta h_f)k$ and ΔH^* is the activation energy of the interfacial transport process. In the following calculation, ΔH^* is assigned an arbitrary value of 20 kcal, which is a sufficient approximation in the region where the growth rate has a strongly negative temperature coefficient. If the growth rate data had extended to the maximum or to lower temperatures, for which growth rates show a positive temperature coefficient, then the ΔH^* term would be better approximated by a WLF type expression (see Hoffman and Weeks [23]). In the expression for K_g, b_0 is the thickness of a coherent surface nucleus, σ the lateral surface free energy, σ_e the end surface free energy characteristic of the chain folds, T_m^0 the equilibrium melting temperature, Δh_f the heat of fusion and k Boltzmann's constant. When $\log G+\Delta H^*/2.3RT$ is plotted against $1/T^2\Delta T$ and a straight line is obtained, then growth is governed by coherent two-dimensional growth nuclei. The slope of the line is $K_g/2.303$. This type of plot is shown in figure 5 for the case $T_m^0=403$ °K. The value of K_g obtained from this plot and the corresponding value of $\sigma\sigma_e$ is given in table 7.

The value of K_g can also be estimated from the half-times for bulk crystallization given in table 2. In this case one plots $-\log t_{1/2}-(1/3)\log\nu_0+\Delta H^*/2.3RT$ against $1/T^2(\Delta T)$, the slope being $K_g/2.303$. A plot of this type is shown in figure 5 for the case $T_m^0=403$ °K. The half-times are corrected for the change in ν_0, the number of growth centers per unit volume, by the term $-(1/3)\log\nu_0$. The data have also been corrected for the induction period τ_i. This correction is small. The K_g value obtained from the dilatometric half-times is identical within experimental error to that obtained from the spherulite growth rate data (see table 7).

The rate data have been analyzed using $T_m^0=399$ °K, $T_m^0=401$ °K, and 403 °K to show the effect of varying T_m^0 on the results. The true value of T_m^0 probably lies between 400 and 402 °K.

The fit of the data to the theoretical expression shown in figure 5 is good for the dilatometric half-time data. In this case the same specimen was used in all the runs. The scatter is greater in the case of the radial growth data, probably because different specimens (from the same lot) were used in making a number of the runs. Nevertheless, the theory seems to provide a reasonable basis for analysis of the data within the estimated experimental error. The fit is almost equally good if T_m^0 is taken to be 401 °K. The fit is poor if T_m^0 is taken to be 398 °K or less.

Lateral surface free energy (σ) was calculated from the equation [23]

$$\sigma=0.10(b_0)(\Delta h_f). \quad (7)$$

Once values have been calculated for σ and $\sigma\sigma_e$, σ_e can be obtained by taking the ratio of $\sigma\sigma_e$ to σ. Results from these calculations are given in table 7.

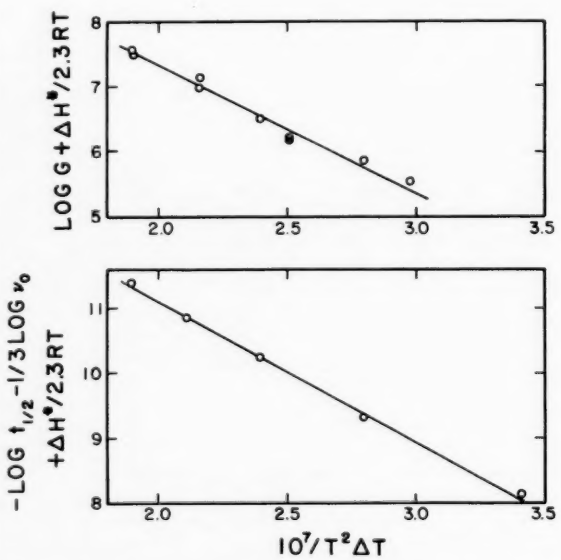

FIGURE 5. *Determination of* K_g *for supercooled liquid→form 2 transformation.*

Upper diagram: Spherulite growth rate data.
Lower diagram: Dilatometric half-time data.

[5] Sometimes the last term in eq (6) is written exp $[-K_g'/T(\Delta T)]$ with $K_g'=4b_0\sigma\sigma_e T_m^0/\Delta h_f k$. This leads to only a slightly different value of $\sigma\sigma_e$ (see references [22] and [23]).

TABLE 7. *Surface free energies and work of chain folding of form 2 polybutene-1*

(Subcooled liquid→form 2 transformation)

Input data

Quantity	Value	Source
Δh_f	1500 cal/mole=9.62 x 10^8 erg/cm³	Diluent method ,Danusso and Gianotti [10].[a]
ΔH^*	20 kcal/mole=83.7 kJ/mole	Hoffman and Weeks [22].
A_0	55.4 x 10^{-16} cm²	Table 3.
b_0	7.45 x 10^{-8} cm [b]	Table 3.
T^0_m	401 ±2 °K	See text.

Results

Quantity	Value			Source
	T^0_m=399 °K; (T_m+4°)	T^0_m=401 °K; (T_m+6°)	T^0_m=403 °K; (T_m+8°)	
K_g (°K)²	3.46 x 10^7	4.17 x 10^7	4.95 x 10^7	Dilatometric data, figure 5.
K_g (°K)²	3.23 x 10^7	3.79 x 10^7	4.42 x 10^7	Radial growth data, figure 5.
$\sigma\sigma_e$ erg²/cm⁴	39.7	110.4	128.6	From average of K_g.
σ mJ/m² or (erg/cm²)	7.16	7.16	7.16	
σ_e mJ/m² or (erg/cm²)	13.8	15.42	17.96	
q (erg/fold)	1.45 x 10^{-13}	1.71 x 10^{-13}	1.99 x 10^{-13}	
	(σ_e=15.5±2.5; q=1.7±0.3 x 10^{-13})			

[a] Wilski and Grewer [16] give the heat of fusion as 974 cal/mole as determined calorimetrically on the assumption that their specimen was 76 percent crystalline as determined from their dilatometric crystallinity scale. According to our χ_2 crystallinity scale, their sample was 0.47 percent crystalline, which leads to a corrected heat of fusion of Δh_f=1570 cal/mole, which is in good agreement with that obtained by Danusso and Gianotti. Wilski and Grewer give the actual heat of fusion of their form 2 specimen as 740 cal/mole. Combining this with Danusso and Gianotti's value Δh_f=1500 cal/mole gives χ_2=740/1500=0.493.

[b] Holland and Miller [26] have shown that growth occurs on the (100) plane in single crystals of form 2.

From the standpoint of the theory of chain folding, one polymer is most aptly compared to another through the work of chain folding, q. The value of the work of chain folding [13, 23], q, is calculated from

$$\sigma_e = q/2A_0 \qquad (8)$$

where A_0 is the cross-sectional area of the chain. The value of q for polybutene-1 is 1.7 x 10^{-13} erg/fold (table 7). In table 8, the values of q and other parameters of interest are compared for polybutene-1, polyethylene [13], and polychlorotrifluoroethylene [13]. The analyses given for polyethylene and polychlorotrifluoroethylene are based on highly reliable values of T^0_m. The value of q for polybutene-1 is seen to be similar to that of polyethylene, but smaller than that for polychlorotrifluoroethylene. We regard the value of q for polybutene-1 to be entirely reasonable, especially in view of its general similarity to that found for polyethylene. On the basis of molecular structure, one would expect the polybutene-1 chain to have a stiffness about like that of polyethylene, but less than polychlorotrifluoroethylene. The value of q for polyethylene is known on the basis of a number of fundamental considerations to represent the work of chain folding [13]. Thus, the crystallization of form 2 polybutene-1 is consistent with a mechanism involving chain folding. At the same time, the value σ_e=15.5 erg/cm² for polybutene-1 is seen to be reasonable in terms of the chain-fold model. Attempts to find a consistent pattern of behavior by directly comparing σ_e values amongst polymers of widely varying cross-sectional areas simply obscures the basic point that q is the more fundamental parameter for the purposes of comparison.

TABLE 8. *Chain fold parameters for various polymers*

	Polybutene-1 (form 2)	Polyethylene [13]	Polychlorotrifluoroethylene [13]
Δh_f (erg/cm³)	9.6 x 10^8	2.8 x 10^9	9.1 x 10^8
b_0 (cm)	7.45 x 10^{-8}	4.11 x 10^{-8}	5.6 x 10^{-8}
A_0 (cm²)	55.4 x 10^{-16}	18.3 x 10^{-16}	36.4 x 10^{-16}
$\sigma\sigma_e$ (erg²/cm⁴)	110	640	156
σ(erg/cm²)	7.2	11.2	3.9
σ_e (erg/cm²)	15.5	57	40
q (erg/fold)	1.7 x 10^{-13}	2.1 x 10^{-13}	2.9 x 10^{-13}
T^0_m (° K)	401	415	494

Note in table 8 that the value of q tends to be larger the higher the melting point. This is consistent with the well-known concept that an increase in chain stiffness raises T^0_m. A chain fold can be formed by raising about 5 bonds into *gauche* states [13]. The data in table 8 suggest that the equilibrium melting temperature increases with the *gauche* energy $\epsilon_g \approx q/5$ according to $T^0_m = \Delta H_f/\Delta S_f \cong [(q/5+C)/k \ln \Omega]$ where C is a constant dependent on van der Waals forces and Ω=3. A more detailed relationship between ϵ_g and T^0_m can be devised which involves appropriate weighting factors, but the oversimplified relationship noted above is sufficient to illustrate qualitatively why increasing q or ϵ_g tends to increase T^0_m.

It is significant that the above analysis in terms of the chain-folding mechanism is successful for a polymer that has a helical conformation in the crystalline state. It is also of interest to compare the above analysis with some that we have attempted (notably on certain "isotactic" specimens of poly-

propylene and polystyrene) where there were independent reasons for suspecting that there were some "wrong," i.e., atactic, sections in the polymer chain. In these cases plots such as those shown in figure 5 were nonlinear, and absurdly low average values of $\sigma\sigma_e$ and q were found. Some of this is probably due to underestimation of T_m^0, which is exceptionally difficult to ascertain with certainty in cases where "copolymer" type melting occurs. Similar nonlinearity and low $\sigma\sigma_e$ and q values are obtained when an analysis is carried out on *any* polymer using a low T_m^0 value. Also, eq (6) can hardly be expected to hold precisely in the partially atactic case because sequence selection problems were left out of consideration in its derivation. Evidently, a sufficient number of the chains in the polybutene-1 used here have long stereoregular sections that crystallize in a manner analogous to that of a flexible homopolymer such as polyethylene where questions of stereoirregularity do not enter. This behavior is consistent with the high degree of crystallinity attained by the specimen of polybutene-1 (see sec. 3.2).

The value of 3 calculated for the Avrami parameter n for the subcooled liquid → form 2 process in the 90 to 110 °C temperature range agrees with those calculated for polyethylene [20] and polypropylene [24]. This value is usually interpreted as indicating that either heterogeneous initiation followed by three-dimensional growth, or sporadic initiation followed by two-dimensional growth, transforms a polymer melt phase into a crystalline phase. The presence of heterogeneous nucleation is supported by photomicrographs (figs. 3 and 4) that show spherulites originating over a narrow time range at a given crystallization temperature. We therefore conclude that polybutene-1 transforms from the melt to the form 2 phase by heterogeneous nucleation followed by three-dimensional growth and the analysis of the dilatometric isotherms was carried out on this assumption. Homogeneous nucleation is in any event extremely improbable except at much larger supercoolings than those attained here.

4.2. Relative Thermodynamic Stability of Form 1 and Form 2

Between 0 °C and its melting point, form 1 is more stable than the lower melting form 2. Form 2 is metastable with respect to form 1 above about 60 °C. A sample crystallized as form 2 at 85 °C in a dilatometer showed no change in mercury level over the period of one year. Nearer to room temperature, form 2 converts to form 1 at an observable rate, and in this region form 2 may be classed as unstable with respect to form 1. On warming from room temperature, form 1 shows no tendency to approach the specific volume associated with form 2 either below or above the melting point of form 2. It is clear that the shift from metastability to instability for form 2 as the temperature falls is simply a matter of increasing rate of the form 2 → form 1 transformation as the temperature is lowered. In polybutene-1, above 0 °C, there is no thermodynamic first-order phase transition between form 1 and form 2 of the type exhibited by polytetrafluorethylene near 20 and 30 °C (see sec. 1).

4.3. Form 2→Form 1 Crystal-Crystal Transformation

As was mentioned earlier, form 2 has an 11_3 helical conformation, and form 1 has a 3_1 helical conformation. The conversion from the 11_3 conformation to the 3_1 conformation during the form 2→form 1 transformation clearly involves an increase of density. Such an increase of density is not surprising, and forms the basis upon which we were able to follow the course of the change. The present work confirms previous observations that the form 2→form 1 transformation is not accompanied by any noticeable change in the morphological features of the spherulites. From the above information, it is reasonable to postulate that the helix change involved in the form 2→form 1 transformation propagates through a given lamella and thereby does not demand any gross reorganization of one lamella with respect to another. The nucleation term impeding the change in helicity is quite large, completely forbidding it at high temperatures, and permitting only a relatively slow rate near room temperature.

The rate of the 2→1 process can be described in terms of the reciprocal of the half-time for the transformation. This is shown in figure 6, where similar data on the supercooled liquid→form 2 process are shown for purposes of comparison.

The subcooled liquid→form 2 transformation has already been analyzed in terms of growth governed by a coherent two-dimensional surface nucleus. The strongly negative temperature coefficient seen for the subcooled liquid→form 2 process in figure 6 is a result of the nucleation term $\exp[-K_g/T^2(\Delta T)]$ in eq (6). The interfacial transport term $\exp[-\Delta H^*/RT]$ would at some lower temperature eventually supervene and cause the rate to fall. Thus a maximum appears in G or $1/t_{1/2}$ for a nucleation-controlled process when the transport term is considered also (see for example [23]). The maximum was not seen for the supercooled liquid→form 2 process, because the rates became too rapid to measure as the temperature was lowered below about 90 °C.

The form 2→form 1 transformation exhibits the negative temperature coefficient and the maximum typical of competing nucleation-controlled and interfacial transport processes. If the form 2→form 1 transformation is in fact nucleation controlled, its much lower overall rate compared to the supercooled liquid→form 2 transformation could be attributed in part to a larger "K_g" value. It is clear, however, that an analysis of the form 2→form 1 transformation cannot be blindly patterned after the subcooled liquid→form 2 calculation. Much more information would be needed before a detailed theory of the form 2→form 1 transformation could be advanced.

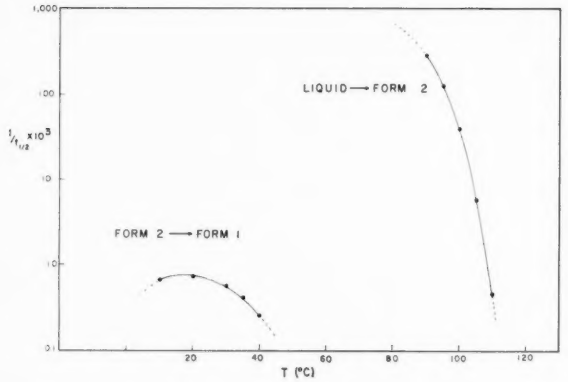

FIGURE 6. *Reciprocal of crystallization rate half-times versus temperature for polybutene-1.*

Boor and Mitchell [14] find a pronounced maximum in the rate of conversion of form 2 to form 1 between 15 and 20 °C which is in good agreement with the present results.

The value of the Avrami growth parameter for the form 2 → form 1 transformation is close to 2. This might be interpreted as being a result of either heterogeneous initiation followed by two-dimensional growth, or sporadic initiation followed by one-dimensional growth. Unlike the case of the supercooled liquid → form 2 transformation, where evidence of heterogeneous initiation was clearly apparent, the type of initiation cannot be positively identified. Boor and Mitchell [25] have observed that the addition of polypropylene or stearic acid accelerates the form 2 → form 1 transformation. This indicates that the process is subject to heterogeneous initiation. While heterogeneous initiation with two-dimensional growth seems the most likely explanation of the observed value of n, sporadic initiation followed by one-dimensional growth cannot be completely ruled out in the case of the uncontaminated polymer.

When observed by eye alone, a freshly prepared sample of polybutene-1 (form 2) gradually becomes more turbid over the period of one week. However, it has already been noted that optical microscopy does not reveal any concomitant change in morphology or general appearance in the spherulites. Both observations might be explained by postulating that the decrease in volume caused by the form 2 → form 1 transformation results in the formation of microvoids in the size range of 3000 to 6000 Å. Such microvoids would be too small to be resolved by an optical microscope, but would interact with visible light so as to render a polybutene-1 film turbid on visual inspection. The existence of such microvoids would naturally alter the crystallinity scale somewhat, but not to the extent of vitiating the conclusions we have based on such determinations.

The authors thank William Meyer for carrying out the viscosity measurements, and Mrs. Rosalind Newman for assisting with the spherulite studies. The financial support from the Advanced Research Projects Agency Program at the National Bureau of Standards on Crystal Growth and Defect Characterization is gratefully acknowledged.

5. References

[1] H. A. Rigby and C. W. Bunn, Nature **164,** 583 (1949).
[2] F. A. Quinn, Jr., D. E. Roberts, and R. N. Work, J. Appl. Phys., **22,** 1085 (1951).
[3] R. K. Kirby, J. Res. NBS **57,** 91 (1956).
[4] G. Natta, Makromol. Chemie **35,** 94 (1960).
[5] R. Zannetti, P. Manaresi, and G. C. Buzzoni, Chim. Ind. (Milan) **43,** 735 (1961).
[6] F. A. Quinn, Jr., and J. Powers, manuscript in preparation.
[7] A Turner-Jones, J. Polymer Sci. Part B, **1,** 455 (1963). See also R. L. Miller and L. E. Neilson, Appendix I in P. H. Geil, Polymer Single Crystals, Interscience, New York (1963).
[8] G. Natta, P. Corradini, and I. W. Bassi, Nuovo Cimento **15,** Suppl. 1, 52 (1960).
[9] C. Geacintov, R. S. Schotland, and R. B. Miles, J. Polymer Sci. Part B, **1,** 587 (1963); Part C, **6,** 197 (1964).
[10] F. Danusso and G. Gianotti, Makromol. Chem. **61,** 139 (1963).
[11] W. R. Krigbaum, J. E. Kurz, and P. Smith, J. Phys. Chem. **65,** 1984 (1961).
[12] N. Bekkedahl, J. Res. NBS **43,** 145 (1949).
[13] J. D. Hoffman, SPE Transactions **4,** 315 (1964).
[14] J. Boor, Jr., and J. C. Mitchell, J. Polymer Sci. Part A, **1,** 59 (1963).
[15] J. D. Hoffman and J. J. Weeks, J. Res NBS **60,** 465 (1958).
[16] H. Wilski and T. Grewer, J. Polymer Sci. **C6,** 33 (1964).
[17] G. Natta, P. Corradini, and I. W. Bassi, Makromol. Chem. **21,** 240 (1956.)
[18] G. Natta, L. Porri, P. Corradini, and D. Morero, Accad. Naz. Lincei, Rend., Classe Sci. Fis., Atti. **20,** 560 (1956).
[19] R. L. Miller in Crystalline Olefin Polymers, edited by R. Raff and K. W. Doak (Interscience, New York, 1963).
[20] W. Banks, M. Gordon, R. F. Roe, and A. Sharples, Polymer **4,** 61 (1963).
[21] F. J. Padden, Jr., and H. D. Keith, J. Appl. Phys. **30,** 1479 (1959).
[22] J. D. Hoffman and J. I. Lauritzen, Jr., J. Res. NBS **65A** (Phys. and Chem.) No. 4, 297 (1961).
[23] J. D. Hoffman and J. J. Weeks, J. Chem. Phys. **37,** 1723 (1962).
[24] L. Marker, P. M. Hay, G. P. Tilley, R. M. Early, and P. J. Sweeting, J. Polymer Sci. **38,** 33 (1959).
[25] J. Boor, Jr., and J. C. Mitchell, J. Polymer Sci. **62,** S70 (1962).
[26] V. F. Holland and R. L. Miller, J. Appl. Phys. **35,** 3241 (1964).

(Paper 69A4–353)

JOURNAL OF RESEARCH of the National Bureau of Standards—A. Physics and Chemistry
Vol. 69A, No. 4, July–August 1965

Compliance-Time-Temperature Relationships from Indentation Measurements on a Pure-Gum Rubber Vulcanizate

Frank L. Roth, George W. Bullman, and Lawrence A. Wood

(March 29, 1965)

Previous work on the calculation of shear compliance J (limit of the ratio of strain to stress at zero deformation) from observations of the indentation of a flat natural rubber surface by a rigid sphere has been extended over greater ranges of time, temperature, and state of vulcanization. The extreme ranges of time were 5 sec to 23.5 hr and of temperature −67 to +100 °C. The curves of JT against log t_{-60} (where t_{-60} is the equivalent time at −60 °C and T is in °K) were sigmoid with a region of maximum slope and continuing through a region of minimum slope extending over about 7 decades. In contrast with the predictions of the Williams, Landel, and Ferry equation, the empirically determined shift of abscissa necessary to give a single JT curve was found to be a linear function of T^{-1} with a slope corresponding to an "apparent activation energy" of 36.9 kcal (°K)$^{-1}$ (mole)$^{-1}$ (154.5 kJ (°K)$^{-1}$ (mole)$^{-1}$).

1. Introduction

The calculation of shear compliance J (limit of the ratio of strain to stress at zero deformation) from observations of the indentation of a flat rubber surface by a rigid sphere has been described in a previous publication [1].[1] Use was made of an instrument conforming to the requirements of ASTM Method D 1415–56T and equipped with a chamber for the maintenance of any constant temperature in the range from −100 to +100 °C. The present work was limited to studies with vulcanizates of a single recipe of natural rubber but covered more extensive ranges of time, temperature, and state of vulcanization than the previous work.

2. Experimental Arrangements

The shear compliance J was obtained from the displacement of a ball indentor 2.38 mm in diameter under the standard load increase from 30 to 564 g, as measured with a Wallace instrument [2, 3] having a scale graduated in International Rubber Hardness units. Details of the operation of the instrument and the calculation of the shear compliance J from the scale readings are given in the previous paper [1].

In the present work use was made of only a single recipe (ASTM Formula 1A, Method D 15–59T, formerly called ACS–1 Recipe) as follows: Natural rubber (NBS 385a) 100; Zinc oxide (NBS 370a) 6; Sulfur (NBS 371b) 3.5; Stearic acid (NBS 372c) 0.5; and Mercaptobenzothiazole (NBS 383) 0.5 parts by weight. The rubber was cured 10, 20, 40, or 80 min at 140°. This recipe has been used more extensively than any other in the testing of natural rubber.

3. Studies Over Extended Times

Values of JT (where T is the temperature in °K) were plotted against the logarithm of the time for each temperature. In the previous work the range of times at any temperature was about 2 decades. In the present work a few studies were undertaken to cover a range of time of about 4 decades (5 sec to 23.5 hr) at each of 3 temperatures. The three temperatures were chosen to give values of JT corresponding respectively to the region of early rise, the region around the first point of inflection, and the region of reduced slope. An arbitrary quantity was subtracted from each observed value of the logarithm of the time in order to bring the three curves together in the single curve of figure 1, corresponding to a temperature of −60 °C. The arbitrary quantities are shown as log a_{-60} in figure 1. For the purpose of orientation it is convenient to show a temperature scale (upper abscissa), which gives the temperature at which the 1-min compliance-temperature product has the value shown by the graph. The corresponding points are readily established at the temperatures of direct observation of the 1-min compliance. Discussion of the general relationship between equivalent time and temperature will be postponed until it can be covered more completely in the last section of this paper.

The figure shows two ranges of more than two decades each where the curve is determined by observations at two different temperatures and a shorter range where agreement is obtained among the results at all three temperatures. This is evi-

[1] Figures in brackets indicate the literature references at the end of this paper.

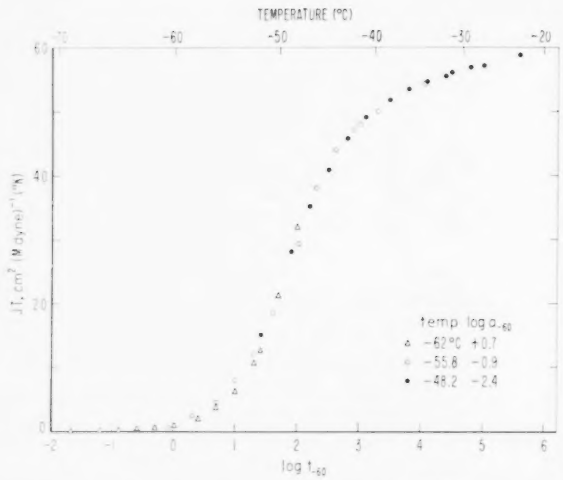

FIGURE 1. *Compliance-temperature product plotted against logarithm of equivalent time (in minutes) at −60 °C.*

Natural rubber vulcanizate ASTM-1A cured 80 min at 140 °C. Scale at top shows temperature at which 1-min compliance-temperature product has value shown by graph.

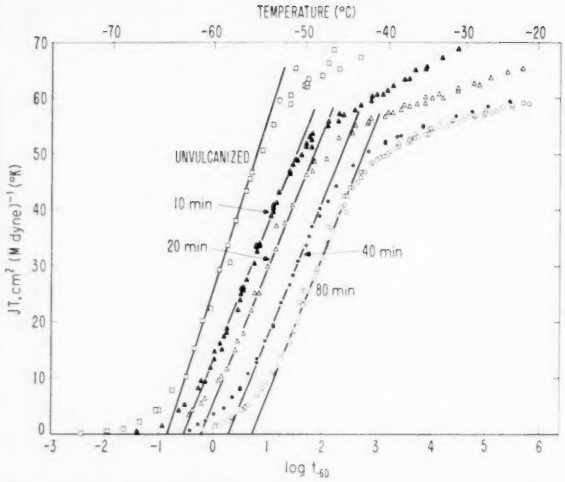

FIGURE 2. *Compliance-temperature product plotted against logarithm of equivalent time (in minutes) at −60 °C.*

Unvulcanized natural rubber NBS-385a and vulcanizates ASTM-1A cured 10, 20, 40, or 80 min at 140 °C. Scale at top shows temperature at which 1-min compliance-temperature product has value shown by graph. Straight lines represent tangents at point of maximum slope.

dence confirming the conclusion of many previous workers that for a given value of JT the slope does not depend on the temperature. This is equivalent to establishing (over the range investigated) the essential validity of the principle of the equivalence of temperature and time in determining the compliance in this region.

In the data shown in figure 1, because of the greater range of time, one can determine more exactly than in our previous work the empirical shifts in the time scale required to bring the JT curve for any temperature into coincidence with that corresponding to −60 °C.

4. Effects of Vulcanization on Compliance and Creep

The effect of varying times of vulcanization is shown in figure 2. The curve marked "Unvulcanized" represents observations on a sample of NBS Standard Sample 385a (Natural Rubber), which was used as the basic rubber in the vulcanizates. This had been milled only enough to permit molding as a disk about 35 mm in diameter and 9 mm in thickness—the same size as the vulcanized samples.

In most instances the values are the means of 3–5 runs near each of the 7–28 temperatures selected for each specimen. Observations were normally made over the range from 5 to 600 sec after the application of the load. With the unvulcanized sample, when JT exceeded about 60 cm² (M dyne)$^{-1}$ (°K), there was a much greater scatter in the values than with the vulcanizates.

The values of T_a, defined as the approximate temperature at which the 1-min value of JT is 0.5 cm² (M dyne)$^{-1}$ (°K) (a convenient small value, readily determined here), are given below, together with the corresponding values of time on the scale used in figure 2.

	Log t_{-60}	T_a
		°C
Unvulcanized rubber	−1.95	−70
Vulcanizate—10 min cure	−1.4	−68
Vulcanizate—20 min cure	−1.1	−69
Vulcanizate—40 min cure	−0.51	−63
Vulcanizate—80 min cure	−0.22	−61

Each value of T_a is probably about 2 deg above the corresponding glass transition temperature T_g determined from volume-temperature relations [1].

As vulcanization proceeds, the glass transition temperature of natural rubber is raised at the rate of about 2.5 °C for each percent of combined sulfur (up to about 4%), according to the mechanical and dielectric measurements of Payne [4] as well as the volume measurements of Martin and Mandelkern [5]. The changes in T_a given in the preceding table (assumed to be the same as the changes in T_g) have been used to calculate the changes in combined sulfur with time of vulcanization. The results are in good agreement with those obtained for this recipe by Gee and Morrell [6], whose direct measurements of combined sulfur showed a linear

increase at the rate of about 0.08 percent/min up to a time of about 30 min followed by an asymptotic approach to the expected limiting value of 3.5 percent for this recipe at longer times of cure.

The values of the maximum slope of each curve (in fig. 2), together with the logarithm of the corresponding time, and the corresponding values of JT are

	Slope $cm^2(M\ dyne)^{-1}$ (°K) $(decade)^{-1}$	Log t_{-60}	JT $cm^2(M\ dyne)^{-1}$ (°K)
Unvulcanized rubber	30. 1	0. 1	29. 2
Vulcanizate—10 min cure	24. 5	. 7	30. 1
Vulcanizate—20 min cure	24. 1	1. 0	29. 9
Vulcanizate—40 min cure	24. 2	1. 4	27. 0
Vulcanizate—80 min cure	24. 6	1. 8	27. 6

The maximum slopes for the vulcanizates do not vary significantly with time of cure, but are appreciably less than that for the unvulcanized rubber. Perhaps this difference is related to the fact that the latter did not contain any vulcanizing ingredients. These, especially the zinc oxide, would be expected to produce a certain stiffening (reduction of compliance) in addition to that resulting from vulcanization.

Aside from this unimportant difference in slopes, the major effect of increased vulcanization at equivalent creep times less than those corresponding to the maximum slopes is a simple change in the time scale. This is apparent from the fact that the curves are approximately parallel to each other in this region. The amount by which the curve for each vulcanizate is shifted along the log t_{-60} scale from the position corresponding to the unvulcanized rubber is shown below:

	Shift measured at JT=0.5 cm^2 $(M$ dyne$)^{-1}$(°K)	Shift measured at JT=29 cm^2 $(M$ dyne$)^{-1}$(°K)
10-min cure	0. 55	0. 56
20-min cure	. 85	. 89
40-min cure	1. 44	1. 49
80-min cure	1. 73	1. 90

The smaller value of JT in this comparison is the one used in the determination of T_a and the larger one was chosen to be close to the average value of JT at the point of maximum slope.

Above the region of maximum slope, increasing the time of cure has additional effects besides the change in time scale, and the curves no longer remain parallel. At the higher values of JT the shifts become greater than those just listed for each vulcanizate. In other words, the slope of the curve for a given value of JT, instead of remaining almost constant with varying times of cure as in the lower region, decreases with increasing cure time. This behavior continues at temperatures and times higher than those considered in figure 2. This decrease of compliance and creep with increasing vulcanization is an expected characteristic of rubber under normal conditions of vulcanization. This behavior is evident with the 10-, 20-, and 40-min cures in figure 2.

When the time of cure is extended to 80 min, however, the phenomenon of "reversion" begins to become apparent. As can be seen in figure 2, the difference in the shifts corresponding to the 40-min and the 80-min cures becomes less (rather than greater) at the higher temperatures and longer times of creep. This trend continues until the curves cross at a point beyond the range shown in figure 2 and it is clear that the longer vulcanization has led to an increased compliance and increased creep. The scission of chains is here considered to be predominant over cross-linking. The occurrence of reversion depends greatly on the nature of the accelerator and other vulcanizing ingredients. Gee and Morrell [6] and Stiehler and Roth [7] showed some years ago that for the recipe employed here, reversion becomes apparent for a cure time between 40 and 80 min at a temperature of 140 °C.

5. Compliance at Higher Temperature

Observations on the vulcanizate cured for 80 min were made over the temperature range from −60 to +100° in order to obtain the values of JT given in figure 3. The results showed random deviations from the solid line but individual points always lay within the band defined by the dashed lines. The random deviations arose from uncertainties in both coordinates, of course, but here the effect of the uncertainty in log t_{-60} was found to be strongly predominant, since it involved judgment in the estimation of the amount of shift necessary for coincidence of two curves, whereas no such estimation was required for the other coordinate. As would be expected, the uncertainty in the amount of horizontal shift was greatest in the intermediate region where the slope was small and was changing very slowly. Here it was most difficult to prove the validity of the principle of the equivalence of temperature and time, and to obtain accurate values of the amount of shift involved. However, there was no evidence of failure of the principle in this region and the horizontal projection of the band of uncertainty became narrower again as the slope of the JT curve increased once more at the highest values.

The JT curve in figure 3 may be divided into three portions—a sigmoid region of rapid rise, a region of nearly constant slope, and a region of final upturn. The first region is dominated by effects associated with the glass transition (as discussed in the preceding section), the second is the region of normal rubber elasticity, and the third region includes deformation mechanisms not available at lower temperatures and shorter times.

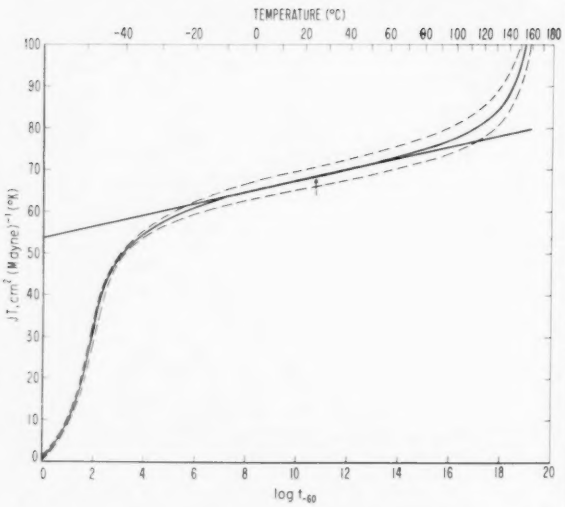

FIGURE 3. *Compliance-temperature product plotted against logarithm of equivalent time (in minutes) at −60 °C.*

Natural rubber vulcanizate ASTM-1A cured 80 min at 140 °C. Scale at top shows temperature at which 1-min compliance-temperature product has value shown by graph. All observed points fall between dashed lines. Straight line represents tangent at second point of inflection. Arrow indicates 1-min compliance-temperature product at 25 °C.

In figure 3 the intermediate region extends from about 7 to 13.6 on the log t_{-60} scale, and the straight line shown would represent the 25° data very well for times from 2×10^{-4} min (12 msec) to about 8000 min, or alternatively the 1-min creep data for temperatures from −10 to +60 °C. The ordinate value $JT]_{1,25}=68$ cm² $(M$ dyne$)^{-1}$(°K), corresponding to 1-min creep at 25 °C, designated by the vertical arrow at log $t_{-60}=10.7$ in figure 3, is near the center of the intermediate region for this vulcanizate.

In this region the viscoelastic behavior can be specified by reporting, for a given standard temperature and time, merely the values of JT and its derivative with respect to log t. In figure 3 the value of $JT]_{1,25}$, 68 cm² $(M$ dyne$)^{-1}$(°K), corresponds to a value of $J_{1,25}$ of 0.228 cm² $(M$ dyne$)^{-1}$ and a Young's Modulus of 13.4 kg/cm². From the slope of the straight line in figure 3 the derivative here is found to be 1.36 cm² $(M$ dyne$)^{-1}$(°K) decade^{-1}. From this one finds that $(1/JT)_{1,25}$ $(dJT/d \log t)_{1,25}=(1/J_{1,25}$ $(dJ/d \log t)_{1,25}=2.0$ percent per decade.

When the logarithm of the ordinate is plotted on the vertical axis instead of the ordinate itself the slope in this region is reduced by a factor of $(2.303\times 68)=157$. Almost all the previous workers have plotted the logarithm of the compliance (or modulus) as ordinate and thus have noted only a very small slope in this region. The name "rubbery plateau," often applied by those who use the logarithmic plot, does not seem to be appropriate for the region of minimum slope in figure 3. Of course the logarithmic ordinate has real advantages for representing small values of JT. When the numerical value of JT is less than 0.4342, the slope becomes greater than that found in the type of plot we have used.

This intermediate region includes the conditions of normal use of most rubber products, and the behavior of a vulcanizate in this region is of much more practical significance than the behavior in the other regions. The values of compliance and its derivative in this region are in good accord with those reported by Gent [8] and by other workers mentioned in our previous paper [1].

The upturn of the curve at the longest times in figure 3 is undoubtedly the effect noted by many previous observers [9, 10] and sometimes denoted as "secondary creep." Gent, in a recent detailed study [11] of secondary creep in different vulcanizing systems, ascribes it to oxidative scission of the network structure. Gent's work showed the primary creep to be essentially completely recoverable, while the extent of recovery of the secondary creep depended greatly on the vulcanizing system.

In our work we obtained considerable creep recovery upon release of the load under all conditions, even following observations at the highest temperatures (up to 100 °C) and longest times (up to 16 hr).

Observations reported here cover a range of values of equivalent time, almost 19 decades, which is greater than that given in any previous work with which we are familiar.

6. Relation Between Time Factor and Temperature

The curves presented in figures 1, 2, and 3 have been derived from observations at different temperatures by empirical shifts along the axis of log t. The magnitudes of all the observed shifts are given in table 1.

A plot of these values as a function of $1/T$, the reciprocal of the temperature in °K, is represented remarkably well by a straight line over the whole range of observation, as can be noted in figure 4. The equation of the line is

$$\log a_{-60}=8.07\times10^{3}T^{-1}-37.85. \qquad (1)$$

The intercept merely reflects the arbitrary choice of −60 °C as the reference temperature. The slope corresponds to an "apparent activation energy" of 36.9 kcal (°K)$^{-1}$ (mole)$^{-1}$ (154.5 kJ (°K)$^{-1}$ (mole)$^{-1}$), obtained by multiplying the slope by the factor $2.303R$, where R is the gas constant 1.9872 cal (°K)$^{-1}$ (mole)$^{-1}$=8.3143 J (°K)$^{-1}$ (mole)$^{-1}$. The same line represents the shifts for the unvulcanized rubber as well as the vulcanizates cured 10, 20, 40, and 80 min.

This very important and unexpected result indicates that the time scale of the molecular processes effective here changes with temperature in a manner not affected by vulcanization. The compliance itself and its derivatives are of course greatly altered by vulcanization, as shown in figure 2.

TABLE 1. *Shifts relative to time at −60 °C*

Temp.	Unvulcanized	Log a_{-60}
	T^{-1} (°K)$^{-1}$ ×10^{-3}	
°C		
−66.7	4.843	+1.35
−59.3	4.675	−0.10
−55.3	4.589	−.90
−50.9	4.498	−1.70
−25.0	4.029	−5.3
−15.8	3.885	−6.5
−12.5	3.836	−7.1
−9.7	3.795	−7.5
0.0	3.660	−9.1
+9.0	3.544	−9.3
10-minute cure		
−57.7	4.640	−0.45
−56.2	4.608	−.55
−55.5	4.593	−.80
−55.4	4.591	−.85
−54.7	4.577	−1.10
−54.0	4.562	−1.10
−53.4	4.550	−1.20
−44.2	4.367	−2.70
−43.4	4.352	−2.90
−29.9	4.110	−4.20
20-minute cure		
−59.0	4.669	−0.15
−56.4	4.613	−.70
−55.8	4.600	−.85
−43.2	4.348	−2.90
−42.0	4.325	−3.15
−35.3	4.203	−3.90
−26.7	4.057	−5.10
40-minute cure		
−55.4	4.591	−0.80
−55.0	4.583	−.95
−54.0	4.562	−1.10
−46.5	4.411	−2.55
−44.1	4.365	−2.85
−32.7	4.158	−4.45
80-minute cure		
−62.0	4.735	+0.7
−60.0	4.690	.00
−55.8	4.600	−.9
−55.7	4.598	−.65
−53.7	4.556	−1.12
−53.0	4.543	−1.18
−52.8	4.537	−1.28
−52.1	4.523	−1.20
−52.0	4.521	−1.53
−48.2	4.444	−2.4
−45.0	4.382	−2.65
−44.2	4.367	−2.75
−34.8	4.195	−4.00
−33.9	4.179	−4.20
−31.5	4.137	−4.50
−30.0	4.112	−4.70
−25.4	4.035	−5.3
−15.8	3.885	−6.3
−12.5	3.836	−7.1
−9.7	3.795	−7.5
0.0	3.660	−8.7
+9.0	3.544	−9.3
+25.3	3.352	−10.7
+40.0	3.193	−12.1
+70.0	2.914	−14.4
+85.0	2.792	−15.4
+100.0	2.680	−16.5

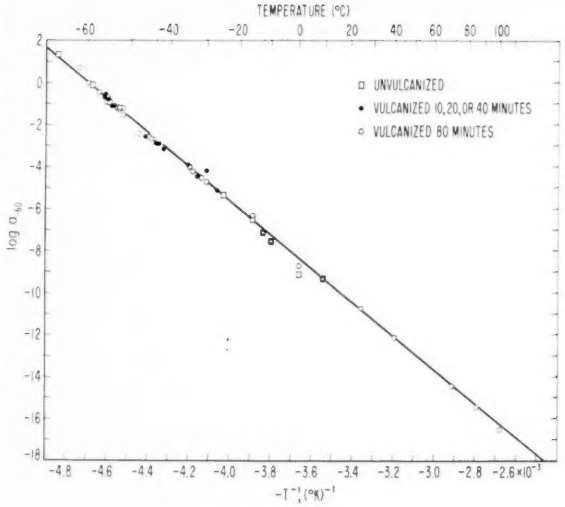

FIGURE 4. *Shift in time scale required to produce coincidence of JT values with those observed at −60 °C, plotted against reciprocal of temperature of observation in °K.*

Scale at top shows temperature in °C. Straight line shown corresponds to "apparent activation energy" of 36.9 kcal (°K)$^{-1}$ (mole)$^{-1}$ (154.5 kJ (°K)$^{-1}$ (mole)$^{-1}$). Data from table 1.

In our previous work [1] we reported similar results at temperatures above −40 °C with an activation energy value of about 38 kcal/mole, based on a much smaller number of observations. At the lowest temperatures (−40 to −60°) in the previous work, there appeared to be a deviation from the straight line in the direction of a considerable increase in the apparent activation energy. This was not found in the present investigation, which devoted particular attention to this region. We can offer no explanation for the discrepancy; we regard the present results as the more reliable.

The range of temperature over which the activation energy appears to remain constant is much greater than any range that has been reported in previous studies of the deformation of natural rubber vulcanizates. However, numerical values near 37 kcal/mole have been found by a number of workers in the region between 0 and −50 °C. In some instances larger values were found at lower temperatures (as in our previous work) and smaller values at higher temperatures; in others no change with temperature was observed over the range investigated.

Kobeko and coworkers [12], for example, report an activation energy of 39 kcal/mole from measurements of primary creep recovery between −70 and +12 °C. Alexandrov and Lazurkin [13] plotted log τ against T^{-1} over the range −51 to −23 °C, where τ is the time corresponding to a maximum in the mechanical loss factor tan δ. From the slope of this graph one calculates a value of 37.6 [14] or 39 kcal/mole [15].

The observations of dynamic modulus made by Zapas, Shufler, and DeWitt [16] on unvulcanized natural rubber have been presented by Ferry [17] in terms of apparent activation energy. From −50 to 0° the values are close to those found in the present work; a slight decrease is noted at higher temperatures, and a very considerable increase is observed as the temperature is lowered to −70°.

The data of Bueche [18] on the shift of creep compliances, for simple extension, of a pure-gum vulcanizate are well represented by a line corresponding to a constant activation energy of about 34 kcal/mole for temperatures from −46° to +50 °C. At lower temperatures higher values of activation energy are indicated.

Allen, Gee, and Read [19] find values decreasing from 37 kcal/mole at −48 °C to 10 kcal/mole at 20 °C for the activation energy determined from the stress relaxation of natural rubber vulcanizates. Hopkins [20] has discussed the differences in apparent activation energies for the deformation of natural rubber as measured by different observers.

In contrast with the results reported here, the equation of Williams, Landel, and Ferry [21, 22] (WLF equation) predicts a monotonic decrease of apparent activation energy with increasing temperature, from values of 60 to 70 kcal/mole at the glass transition temperature to 16 to 17 kcal/mole at temperatures 100° higher than T_g, when $-73° < T_g < -60$ °C. The data of Payne [4] on a pure-gum vulcanizate of natural rubber appear to conform to the WLF relation over a wide range of temperature. However, the apparent activation energies predicted by the equation and observed by Payne between −60 and −35 °C differ from the value found here by less than the experimental error.

Above −35 °C, where the discrepancy becomes appreciable, Payne's plots of the logarithms of the reduced storage and loss moduli G' and G'' against log t have become nearly horizontal and the shifts are very difficult to determine. We consider the sensitivity of the logarithmic plots above −35 °C to be inadequate to evaluate the shift with sufficient accuracy to determine whether or not there is a change of apparent activation energy with temperature in this region. This is not the case in the present work where the slope of the JT plot in this region is about 157 times that of the logarithmic plot, as already mentioned. Consequently the slope is readily determined at all temperatures above −35 °C. Below −60 °C the situation is reversed and the logarithmic plot is much more sensitive, since JT and its derivative have both become very small.

We shall not attempt to discuss here the nature of the molecular processes [8, 11] involved in the deformations studied in the present work. It may be pointed out, however, that the activation energy for viscous flow in liquids is usually found to be in the range 5 to 15 kcal/mole [23] and the value for natural rubber has been given as 8 to 10 kcal/mole [24]. Treloar [15] has already called attention to the large difference between this value and that calculated from the observations of Alexandrov and Lazurkin. One concludes that irrecoverable flow involving the translation of whole molecules is not the fundamental process here.

Several previous workers [22, 25] have regarded a constant activation energy as normal at the higher temperatures and the WLF relation as representing merely deviations caused by the approach to the glass transition. The WLF equation has often been regarded as valid for temperatures from that of the glass transition T_g to T_g+100 °C.

According to the present work in the case of natural rubber, either unvulcanized or in our pure-gum vulcanizate, this range of validity is found to be reduced to zero. We suggest the possibility that this behavior is associated with the fact that natural rubber approaches ideal rubber elasticity more closely than other systems that have been studied. It may be pointed out that in our previous work, extended regions of constant activation energy were found above T_g+20 °C for pure-gum vulcanizates of butyl rubber and styrene-butadiene rubber, but not for chloroprene rubber or nitrile rubber. The latter two are polar polymers having higher glass transition temperatures, and their behavior deviates more from ideal rubber elasticity. Likewise we have not been able to find regions of constant activation energy for vulcanizates containing carbon black. These too show behavior deviating more from ideal rubber elasticity than the pure-gum vulcanizates. In this instance even the validity of the shifting operation is somewhat questionable.

Further work of this type should be conducted on vulcanizates of natural rubber with other curing systems and on other types of rubber. It would be especially interesting to know whether conditions could be found in which the apparent activation energies for butyl rubber (20 kcal/mole) and styrene-butadiene rubber (22 kcal/mole) would remain constant below the temperature limits, −40 and −25 °C, respectively, found in our previous work.

7. References

[1] L. A. Wood and F. L. Roth, Creep of pure-gum rubber vulcanizates from indentation-time measurements. Proc. Fourth Rubber Technology Conference, London, England, May 1962. Paper No. 28, p. 328, Institution of the Rubber Industry, London 1963; Rubber Chem. Technol. **36,** 611 (1963).

[2] A. L. Soden, A practical manual of rubber hardness testing, India Rubber J. **120,** 13 (1951).

[3] J. M. Buist, Physical testing of rubber. Chapter in book The Applied Science of Rubber, ed W. J. S. Naunton, p. 736 (Edward Arnold Ltd., London, 1961).

[4] A. R. Payne, Temperature-frequency relationship of dielectric and mechanical properties of polymers. Chapter in book Rheology of Elastomers, ed by P. Mason and N. Wookey, p. 86 (Pergamon Press, London, 1958).

[5] G. M. Martin and L. Mandelkern, Glass formation in polymers: II The system rubber-sulfur, J. Res. NBS **62,** 141 (1959) RP2944.

[6] G. Gee and S. H. Morrell, Quantitative characterization of cure. IV. Definition and measurement of rate of cure for pure-gum natural-rubber compounds, Trans. Inst. Rubber Industry **28,** 102 (1952); Rubber Chem. and Technol. **25,** 454 (1952).

[7] R. D. Stiehler and F. L. Roth, Vulcanization characteristics of natural rubber, ASTM Special Technical Publication 136, p. 50 (1952); India Rubber World **127,** 783 (1953); Rubber Chem. Technol. **26,** 593 (1953).
[8] A. N. Gent, Relaxation processes in vulcanized rubber. I. Relation between stress relaxation, creep, recovery, and hysteresis, J. Appl. Polymer Sci. **6,** 433 (1962).
[9] S. D. Gehman, Creep, Recovery, and permanent set for GR–S and Hevea, J. Appl. Phys. **19,** 456 (1948); Rubber Chem. Technol. **22,** 105 (1949).
[10] G. M. Martin, F. L. Roth, and R. D. Stiehler, Behavior of pure-gum rubber vulcanizates in tension, Trans. Inst. Rubber Ind. **32,** 189 (1956); Rubber Chem. Technol. **30,** 876 (1957).
[11] A. N. Gent, Relaxation processes in vulcanized rubber II. Secondary relaxation due to network breakdown, J. Appl. Polymer Sci. **6,** 442 (1962).
[12] P. Kobeko, E. Kuvshinskii, and G. Gurevich, Elasticity of amorphous bodies, Bull. Acad. Sci. USSR **3,** 329 (1937) (in Russian); J. Tech. Phys. USSR **4,** 622 (1937) (in English). See H. Leaderman, Textile Research **11,** 171 (1941), and Reference [14], pages 32 and 80.
[13] A. P. Aleksandrov and Y. S. Lazurkin, A study of polymers; I. Highly elastic deformation of polymers, J. Tech. Phys. USSR **9,** 1249 (1939) (in Russian); Acta Physicochemica URSS **12,** 647 (1940) (in English); Rubber Chem. Technol. **13,** 886 (1940).
[14] H. Leaderman, Elastic and creep properties of filamentous materials and other high polymers, p. 80, Textile Foundation, Washington, D.C., 1943.
[15] L. R. G. Treloar, The physics of rubber elastic 2d Ed. (Oxford Univ. Press 1958).
[16] L. J. Zapas, S. L. Shufler, and T. W. DeWitt, Comparison of the dynamic properties of natural rubber and GR–S, J. Polymer Sci. **18,** 245 (1955).
[17] J. D. Ferry, Chapter in book ed by H. A. Stuart, Die Physik der Hochpolymeren, Vol. 4, p. 392 (in English) (Springer-Verlag, Berlin, 1956).
[18] F. Bueche, Mechanical properties of natural and synthetic rubbers, J. Polymer Sci. **25,** 305 (1957).
[19] G. Allen, G. Gee, and B. E. Read, Stress relaxation in elastomers by visco-elastic mechanisms; I. Natural rubber at high rates of strain and low temperatures, Trans. Faraday Soc. **55,** 1651 (1959).
[20] I. L. Hopkins, The Ferry reduction and the activation energy for viscous flow, J. Appl. Phys. **24,** 1300 (1953).
[21] M. L. Williams, R. F. Landel, and J. D. Ferry, The temperature dependence of relaxation mechanisms in amorphous polymers and other glass-forming liquids, J. Am. Chem. Soc. **77,** 3701 (1955).
[22] J. D. Ferry, Viscoelastic properties of polymers, p. 228, (John Wiley & Sons, Inc., New York, 1961).
[23] F. Bueche, Physical properties of polymers, p. 90, (Interscience Publishers, Inc., New York. 1962).
[24] Reference [15], p. 299.
[25] W. P. Slichter, Nuclear magnetic resonance studies of elastomers, Rubber Chem. Technol. **34,** 1574 (1961).

(Paper 69A4–354)

JOURNAL OF RESEARCH of the National Bureau of Standards—A. Physics and Chemistry
Vol. 69A, No. 4, July–August 1965

Distribution Function of the End-to-End Distances of Linear Polymers With Excluded Volume Effects

Jacob Mazur

(March 9, 1965)

The distribution function of the absolute values of chain lengths of a polymer molecule which displays the excluded volume effect cannot assume a Gaussian form. This fact follows directly from theoretical considerations based on the application of the Central Limit Theorem to the theory of Markov chains. In order to determine the exact shape of the polymer chain-end distribution function we calculated its various moments taken about the origin, and their dependence on the number of polymer segments, using a Monte Carlo technique for generating polymer chains on a lattice. The results obtained from the extrapolation of various combinations of these moments of the general form

$$\delta_n=\frac{\langle r_n^g\rangle}{\langle r_n^s\rangle^{g/s}}-1 \text{ for } n\to\infty$$

are used to determine the shape of the polymer distribution function. It is found that the chain-end distribution function can be approximated by the following form:

$$W(r)\,dr=\left[\Gamma\left(\frac{3}{t}\right)\right]^{-1} t\alpha^{3/t}r^2 \exp\,(-\alpha r^t)\,dr,$$

with $t=3.2$ and α being a parameter, determinable from the average mean square chain-end distances.

1. On the Incompatibility of Excluded Volume Effects With Gaussian Statistics

The distribution of end-to-end distances in a sufficiently long, freely jointed chain is invariably a Gaussian one. This fact follows directly from the Central Limit Theorem as it is applied to the sequence of mutually independent random variables with a common distribution. (That is, each of the random variables which form a chain has the same distribution; this kind of chain is sometimes designated as a homogeneous one [1].[1])

One can apply the Central Limit Theorem to random variables which form a homogeneous Markov chain, in order to demonstrate the fact that the Gaussian distribution law is approached in the limit for chains in which the position of a polymer unit depends on the position of the preceding one [2] as well. Real polymer chains with internal rotation around their bonds, whether free or hindered, will be accurately described by Markov chains. The classification of polymer chains as Markovian is broader than this. Thus, if one eliminates chain closures formed with a fixed number of steps (such as four-step closures on cubic lattices or six-step closures on diamond lattice), one still can apply the theory of Markov chains for these models, since the distribution of probabilities of a particular event is still determined uniquely by the preceding event, which, in this case, is a formation of a four-step or a six-step loop [3]. This description does not yet exhaust all possible cases of polymer chains which can be described by Markov chains. As has been pointed out by Montroll [4], for any polymer chain with forbidden conformations being restricted to nonself intersection of loops with l intervening steps, the distribution of intrachain distances of n steps will assume a limiting Gaussian form, provided that $n>>l$. For this reason any infinitely long polymer chain with finite-range correlations can be described as a Markov chain. The question as to whether every Markov chain will lead to a limiting Gaussian distribution is a more involved one. The restrictive conditions under which the Central Limit Theorem can be applied to a sequence of random variables forming a homogeneous Markov chain are usually satisfied for linear polymer chains as will be demonstrated. For example, one of the conditions is the nonperiodicity of the distribution of the individual segments. However, whenever a polymer chain satisfies the condition for the validity of the Central Limit Theorem, the distribution of the intramolecular distances becomes a Gaussian one, provided that the number of intervening steps is large enough.

We propose that the distribution function of polymer configurations with volume effect cannot be Gaussian even in the asymptotic case of an infinitely long chain. In other words, the application of Gaussian statistics is invalid for the case of mutually excluding random events, such as forbidden double occupancy of the same volume element of the

[1] Figures in brackets indicate the literature references at the end of this paper.

polymer chain. The proof of this statement is obtained from the following heuristic, rather than from rigorous mathematical analysis: An excluded volume effect implies an existence of long-range order in a polymer chain for the simple reason that the probability distribution function of a given polymer segment is no longer independent of the initial probability distribution. (In the terminology of the theory of cooperative phenomena, a system for which there exists a correlation between the distribution of any two statistical elements, no matter how widely they are separated by other elements, is characterized by the presence of a long-range order. Therefore, excluded volume effects, defined by mutual exclusions of double occupancies of volume elements on a lattice, imply a presence of long-range correlation in a polymer chain.)

Consider a matrix P of transition probabilities p_{ij}. The p_{ij} are the probabilities for a random variable having a certain value of α_i, given that the previous random variable has a value of α_j. From the theory of Markov chains we know that if the matrix P possesses a real nondegenerate root (or eigenvalue) λ_1, which has a value that is larger than the absolute value of any other root, then the probability distribution of a given random variable becomes independent of its initial distribution, provided that the number of steps is sufficiently large. In other words, the distribution of the polymer segments represented by the random variables becomes stationary, and there is no correlation between individual segments which are a long distance apart (no long-range order can exist). But we know from the Central Limit Theorem that this is precisely the condition for the Gaussian statistics to be descriptive of the distribution function of intramolecular separations. In order to complete our proof that the excluded volume effect is inconsistent with the Gaussian statistics one has to discuss the possibility of Markov chains with long range order. This long-range order will always be present whenever the largest root of the matrix of transition probabilities is a degenerate one [5]. Therefore, we will demonstrate that in regular polymer chains this degeneracy cannot occur as long as they are represented by Markov chains. For this purpose, the model of absorbing Markov chains is employed, since they encompass the most general type of a polymer chain in which certain chain conformations of finite number of steps are either biased or virtually excluded [3]. In absorbing Markov chains, the absorbing state represents a boundary which terminates the process of adding a step to the chain. Thus, the matrix of transition probabilities with absorbing states is stochastic. This matrix is decomposable since it can always be of the following form

$$P=\begin{pmatrix} A_{11} & A_{12} \\ 0 & A_{22} \end{pmatrix}. \qquad (1)$$

This matrix, being stochastic, has a largest eigenvalue equal to 1. The matrix of transient states A_{22}, raised to the nth power represents all real conformations of an n-step polymer chain. By definition, its largest eigenvalue must be less than 1 in absolute value. Thus, the states of a polymer chain are decomposed into the forbidden conformations, resulting from short-range volume exclusions, and the transient states. Since we are interested only in the latter states, we demonstrate that the largest eigenvalue of the matrix A_{22} is also positive and single. To do this, we employ the Frobenius theorem for matrices with nonnegative elements as follows [6].[2] Any square matrix with nonnegative elements has a characteristic root which is both larger in its absolute value than any other root and is nondegenerate, provided that such a matrix cannot be decomposed, that is, no permutation matrix T exists such that

$$TA_{22}T^{-1}=P$$

where P is the matrix of the general form (1). (A permutation matrix is obtained through permutation of columns of an identity matrix.) In order to show that the matrix of transition probabilities for a chain that reached its closure in a fixed number of steps in the case of a linear homogeneous polymer is a nondecomposable one, we demonstrate the following: (1) All superdiagonal terms of such a matrix are nonzero. This follows from the fact that the superdiagonal terms represent the shortest path for the random walk to form a closed configuration (or to reach its absorbing state, which is a "point of no return"). (2) In addition, each of the columns must have at least another nondiagonal, nonzero element. This is because at least two different chain conformations should result when a step is added at random to the end of the chain. In addition, the first column (which does not possess a superdiagonal term) should have at least one nonzero element other than the top or the bottom one. Otherwise, we will encounter a periodic boundary condition, since the same chain conformation will be repeated regularly, contrary to our model for a regular polymer chain. In our other publication [3], the two bottom rows of the matrix of transition probabilities are all filled up, so that the conditions for nondecomposability of the matrix of transition probabilities are satisfied. (In regular polymer chains, one should be able to reach any permissible chain conformation from any other chain conformation by a finite number of steps.)

Another way to prove the nondecomposability of the Markov matrix with zero elements is to raise it to some power. If this operation will result in matrix having no zero elements, its nondecomposability becomes obvious. In reference [3], the matrix of eq (16) raised to the power of l-2, will have all its original zeros replaced by positive elements. Thus,

[2] The Frobenius theorem, as quoted by most authors, deals with matrices with positive, nonzero elements [7]. This theorem has been applied in order to investigate the conditions for the absence of long-range order in certain physical models based on Markov chains, e.g., for Ising model of ferromagnet, order-disorder transitions in crystals, etc. However, there is a later Frobenius theorem [6] which deals with nonnegative matrices and which is applied here to polymer chains.

since there is no possibility, with simple polymer chains, to exhibit a degeneracy, or a long-range order, in their Markov-chain models, the Gaussian limiting law could obtain only when long-range excluded volume effects are absent in such chains. For example, the proof given by Montrol [4] who derived the Gaussian limiting law for any given function whose average is taken over the Markov chain, requires the existence of a single largest root of the matrix of transition probabilities. One can easily deduce from Montroll's derivation, that, if the largest root were degenerate, a Gaussian limiting law could not be obtained.[3]

In conclusion, we have demonstrated the following: (a) Polymers which are characterized by a chain of independent events or by homogeneous Markov chains invariably lead to Gaussian distribution of the probabilities of their lengths. This follows from the application of the Central Limit Theorem to random variables forming a statistical chain. (b) Chains which possess long-range correlation, such as an excluded volume, cannot have a Gaussian distribution for their intramolecular dimensions, even in the limiting case of an infinitely long chain. This follows from the fact that, for the distribution function of polymer dimensions to be Gaussian, the matrix of transition probabilities must be devoid of long-range order (i.e., its largest root must be nondegenerate).

Wall, Windwer, and Gans [8]; Verdier and Stockmayer [9], and Schatzki [10] have demonstrated, on the basis of Monte Carlo computations, that the distribution of end-to-end distances in a polymer chain is non-Gaussian. Similarly, Fisher and Hiley [11] have demonstrated the same thing using their chain-counting method. Thus, direct numerical computations of the distribution of polymer chain-end lengths and the theoretical considerations along the above given guidelines prove the invalidity of the application of Gaussian statistics to the polymer chains with excluded volume. It is of importance to find from numerical analysis the *form* of the distribution of polymer configurations with excluded volume effects, and this is the purpose of the present work.

2. Computational Part

It is clear from the above arguments that the excluded volume effect of a polymer chain cannot be given a theoretical treatment on the basis of theories of Markov chains. There are certain physical problems in which long-range order is accessible to theoretical treatment; e.g., critical phenomena associated with the conditions for the largest root of a Markov matrix of transition probabilities becoming a degenerate one. Unfortunately, a similar treatment of excluded volume as a long-range order does not seem to be possible in the case of a polymer chain. Here, again, numerical methods rather than a theoretical analysis seem to be the only practical way for determining statistical properties of polymer chains resulting from the presence of excluded volume. Monte Carlo methods do provide a solution to the problem of estimating the mean square end-to-end distance of a polymer chain as a function of the number of steps. If one, however, tries to apply directly the same Monte Carlo calculations in order to find the polymer chain-end distribution function, one will run into technical difficulties: The "tail part" of the distribution function will show a very large scatter of data, since there will be few configurations in that part; on the other hand, near the peak of the distribution function the distances are small and one will run into the so-called "lattice effect". This effect is related to the fact that only certain discrete intramolecular separations are possible. These distances do not possess the same degeneracy, since the number of lattice sites within a given distance r from a given lattice point is an irregular function of r which depends on the lattice structure. The inspection of Monte Carlo data presented by Wall, Windwer, and Gans, by Verdier and Stockmayer, and by Schatzki clearly demonstrates the technical difficulties in finding the distribution of polymer configurations, except for demonstrating their non-Gaussian behavior, which is to be expected. Schatzki carried his calculations one step further by expanding the distribution function of end-to-end separations in terms of Hermite polynomials; the lowest term reduces, however, to the Gaussian distribution function for the case of no excluded volume.

Our effort will be less ambitious. By going to the case of an infinitely long chain we will establish the shape of the distribution function from certain combinations of the distance averages taken over it. By the shape of the distribution function we imply the particular term which determines its rate of decay as the distance of separation between polymer segments becomes large. If, in addition, we have another relationship that establishes the dependence of the mean-square dimension on the number of polymer segments, we can readily construct the entire polymer chain-end distribution function, which for most practical purposes should be accurate enough for the purpose of estimation of its various statistical properties.

The case of an infinitely long polymer molecule is of theoretical interest. We study this case by plotting the computed averages as functions of $1/n$, and extrapolating the resulting curve toward $1/n=0$. The limiting distribution function must incorporate excluded volume effects resulting from the presence of long-range correlations. As we know, incorporation of only finite-range correlations, e.g., nonself intersections of finite-sized loops in polymer chain will eventually lead to the Gaussian distribution of chain-end separations. Therefore, the true non-Gaussian form of the polymer distribution function is most evident in the asymptotic case of an infinitely long chain. Moreover, the effects of the finite size

[3] A simple statement that the Gaussian distribution is always obtained for finite Markov chains would serve our purpose, but it will be criticized as an oversimplification. We, therefore, prefer to present this more detailed proof, that such is the case with simple, linear polymer chains. Our only assumption is that all polymer chains can be described as special cases of the general class of absorbing chains, which were first introduced by us in reference [3].

of the excluded volume per segment and of the lattice structure are then obliterated.

Fisher and Hiley calculated the mean fourth power of end-to-end distances, $\langle r_u^4 \rangle$, for nonself intersecting random walks on simple cubic and plane-square lattices, using the chain-counting method [11]. From their values of $\langle r_n^4 \rangle$, they calculated the fractional variance of r_n^2, namely the quantity

$$\delta_n = \langle (r_n^2 - \langle r_n^2 \rangle)^2 \rangle / \langle r_n^2 \rangle^2 = \frac{\langle r_n^4 \rangle}{\langle r_n^2 \rangle^2} - 1. \qquad (2)$$

A plot of δ_n versus $1/n$ is easily extrapolated to the limit of $1/n=0$, in spite of the fact that the exact computations were carried only to the first 10 steps. For a cubic lattice, they obtained for the extrapolated fractional variance of r_n^2, $\delta_\infty = 0.453$ (for a Gaussian distribution, $\delta_\infty = 2/3$). We were more interested to notice the fact that, for a simple nonintersecting chain, δ_n reaches a limiting value rapidly; therefore, δ_n is practically independent of the number of steps.

A reasonable form for the polymer chain-end distribution function is of the form $W(r, n)dr = Ce^{-\alpha(n) r^t} dr$ where C is determined from the normalization condition imposed on $W(r, n)$, taken over a volume of a sphere.[4] If one defines

$$\langle r^p \rangle = \frac{\int_0^\infty r^p e^{-\alpha(n) r^t} 4\pi r^2 dr}{\int_0^\infty e^{-\alpha(n) r^t} 4\pi r^2 dr} \qquad (3)$$

then it is evident that, for any value of t, $\frac{\langle r^p \rangle}{\langle r^s \rangle^{p/s}}$ is independent of α, and therefore, is independent of the number of steps. However, the integrations in eq (3) should be taken not from $r=0$, but from $r=a$, where a corresponds to the distance of the nearest possible approach. However, no matter how large a is, in the asymptotic case of $n=\infty$, the asymptotic formula for δ_n should be independent of a. Therefore,

$$\delta_\infty(p, s) \equiv \frac{\langle r^p \rangle}{\langle r^s \rangle^{p/s}} - 1 = \frac{\Gamma\left(\frac{p+3}{t}\right)\left[\Gamma\left(\frac{3}{t}\right)\right]^{p/s-1}}{\left[\Gamma\left(\frac{s+3}{t}\right)\right]^{p/s}} - 1. \qquad (4)$$

In the case of $s=2$, $\delta_\infty(p, 2)$ is identical with the fractional variance of $r^{p/2}$, since then

$$\delta_\infty(p, 2) = \frac{\int_0^\infty (r^{p/2} - \langle r^{p/2} \rangle)^2 W(r, \alpha) dr}{\langle r^{p/2} \rangle^2}. \qquad (5)$$

One would therefore expect that, if $\langle r^4 \rangle$ and $\langle r^2 \rangle$ were calculated for a random walk on a cubic lattice with unit distances between any two lattice points being forbidden, the same value of $\delta_\infty(4, 2)$ would be obtained, as calculated by Fisher and Hiley for nonintersecting random walks on the same lattice. However, the limiting value of δ_∞ will be reached much slower than in the case of simple nonintersecting random walk. We therefore calculated $\langle r_n^4 \rangle$ as well as $\langle r_n^2 \rangle$ for a random walk on a cubic lattice with unit distances being forbidden. The special method for the Monte Carlo computations employed here and the computational details will be described elsewhere. In figure 1 the results of these computations are shown. A total number of 300,000 random walks were generated, and the computations were carried up to $n=60$. However, beyond $n=50$ the scatter of the data does not permit us to use the corresponding results.

In order to avoid crowding of data owing to the use of the reciprocal scale, the part of the curve for $22 < n < 40$ is redrawn in the insert on an enlarged scale. This way, the entire δ_n versus $1/n$ curve as well as the detailed data which are especially needed for the accuracy of their extrapolation towards $n=\infty$ are shown. On the right-hand side of figure 1 and of the subsequent figures the values of the parameter t are shown, that are calculated from the corresponding values of $\delta_\infty(p, s)$, as given by eq (4). Thus, the intercept of the extrapolated data of these figures with the $n=\infty$ axis leads to the correct value of the parameter t of eqs (3) and (4). The various values of the parameter t shown on the $n=\infty$ axis are presented in order to demonstrate the accuracy in this determination of the extrapolated value of t. An inspection of figure 1 not only points to the impossibility of approximating the Gaussian value of $t=2$, but to the fact that the parameter t can be accurately determined to within one-tenth of a unit.

As was to be expected, the limiting value for δ is almost identical with the one reported by Fisher and Hiley ($\delta_\infty = 0.443$ as compared to their $\delta_\infty = 0.453$).

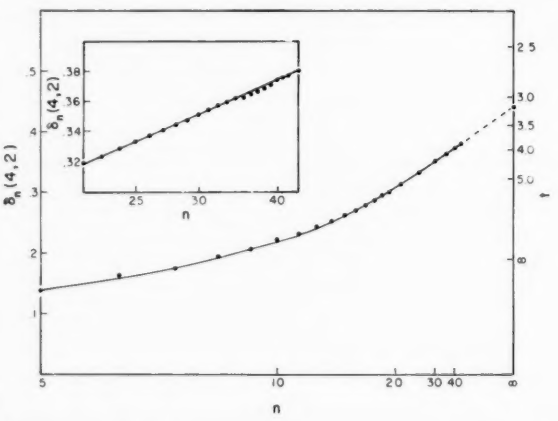

FIGURE 1. *Plot of* δ_n (4, 2), *the relative fractional variance of* r^2_n, *versus* 1/n, *for random walk on a simple cubic lattice with excluded unit distance approaches.*

[4] Recently, C. Domb [12] proposed a different form for $W(r, n)$. In the appendix of this paper these two choices for the chain-end distribution function are compared, and a more general form for $W(r, n)$, which involves two structural parameters, is introduced.

Moreover, the limiting value of δ is reached much slower now, owing to the fact that the distance of closest approach is considerably larger than it was for the case of simple nonintersecting chains with no other restriction being imposed on the closest possible approach between chain elements. For short chains δ_n is much less than its limiting value δ_∞, as is to be expected, considering the particular form for the distribution function. From the extrapolated value of $\delta_\infty(4,2)=0.443$, one finds that $t=3.2$. Therefore, for three-dimensional lattices with excluded volume, the normalized distribution function, $W(r, n)dr=3.0765\alpha^{0.9375}r^2 \exp(-\alpha r^{3.2})dr$. (For two dimensional lattices, t is considerably larger.) The parameter α is undetermined. However, it can be easily calculated from any given relationship between $\langle r^p\rangle$ and n. For example, one can replace α by

$$\alpha=\left[\frac{\Gamma\left(\frac{5}{3.2}\right)}{\Gamma\left(\frac{3}{3.2}\right)\langle r_n^2\rangle}\right]^{1.6} \tag{6}$$

if the relationship between $\langle r_n^2\rangle$ and n is given independently.

In order to reassure ourselves that the suggested form for the distribution function serves as a good approximation, we calculated, for the same lattice model, the following averages: $\langle r\rangle$, $\langle r^3\rangle$, $\langle r^6\rangle$, and $\langle r^8\rangle$. Thus, $\delta_\infty(p, s)$ is calculated for several combinations of p and s. In figures 2 through 5 the following fractional "averages" were computed. (If $s\neq 2$, $\delta(p, s)$ cannot be any more designated as a fractional variance.)

$$\frac{\langle r^2\rangle}{\langle r\rangle^2}-1 \quad (p=2, s=1),$$

$$\frac{\langle r^6\rangle}{\langle r^3\rangle^2}-1 \quad (p=6, s=3),$$

$$\frac{\langle r^6\rangle}{\langle r^2\rangle^3}-1 \quad (p=6, s=2),$$

$$\frac{\langle r^8\rangle}{\langle r^4\rangle^2}-1 \quad (p=8, s=4).$$

We notice that the results for $\delta_\infty(p, s)$, based on $t=3.2$ and computed from eq (4) agree all very well with the extrapolated results of figures 2 through 5.

For further verification of this fortuitously chosen distribution function we will investigate the dependence of $\delta_n(p, s)$ on n and on the distance of the nearest possible approach a, as follows:

A general expression for $\delta_n(p,s)$ is given in terms of incomplete Gamma Functions, $\Gamma(y, x)$,

$$\delta_n(p, s)=\frac{\Gamma\left(\frac{p+3}{t}, \alpha a^t\right)\left[\Gamma\left(\frac{3}{t}\right), \alpha a^t\right]^{p/s-1}}{\left[\Gamma\left(\frac{s+3}{t}, \alpha a^t\right)\right]^{p/s}} \tag{7}$$

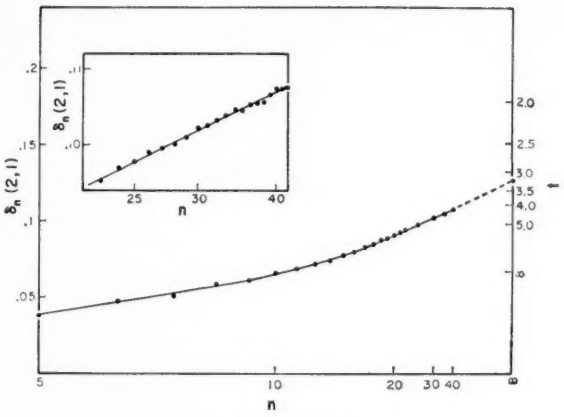

FIGURE 2. *Plot of* δ_n *(2, 1) versus* 1/n.

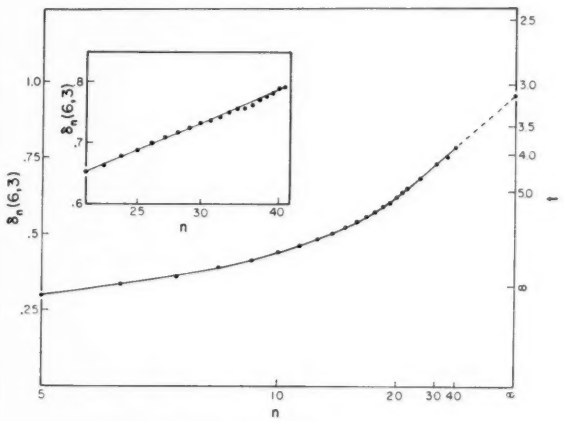

FIGURE 3. *Plot of* δ_n *(6, 3) versus* 1/n.

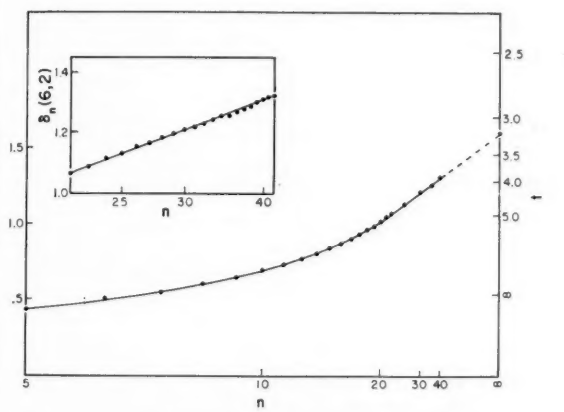

FIGURE 4. *Plot of* δ_n *(6, 2) versus* 1/n.

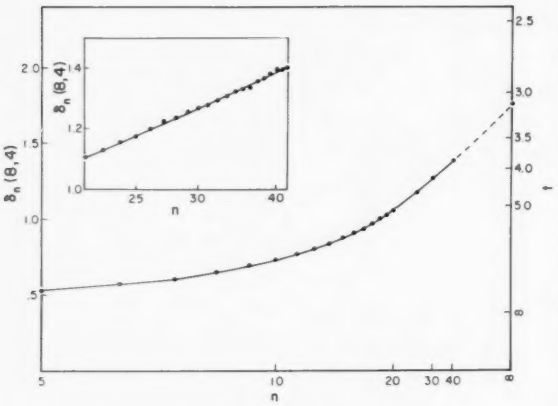

FIGURE 5. *Plot of* δ_n $(8, 4)$ *versus* 1/n.

with the following definition for $\Gamma(y, x)$,

$$\Gamma(y, x)=\int_x^\infty e^{-t}t^{y-1}dt.$$

The most convenient expansion for the incomplete Gamma Function with small x is: $\Gamma(y, x)=\Gamma(y)-y^{-1}x^y e^{-x}M(1, 1+y, x)$ where $M(1, 1+y, x)$ is a confluent hypergeometric function [13]. Since x, which is equal to αa^t, is invariably small (except when n is also small), $M(1, 1+y, x)$ can be approximated by the first two terms of Kummer's Function as $M(1, 1+y, x) \cong 1+\frac{x}{1+y}$. Therefore,

$$\delta_n(p, s)\cong\left\{\Gamma\left(\frac{p+3}{t}\right)-\left(\frac{t}{p+3}\right)\alpha^{\frac{p+3}{t}}a^{p+3}(1-\alpha a^t)\left(1+t\frac{\alpha a^t}{p+3}\right)\right\}\times\frac{\left[\Gamma\left(\frac{3}{t}\right)-\frac{t}{3}\alpha^{\frac{3}{t}}a^3(1-\alpha a^t)(1+t\alpha a^t)\right]^{p/s-1}}{\left[\Gamma\left(\frac{s+3}{t}\right)-\frac{t}{s+3}\alpha^{\frac{s+3}{t}}a^{s+3}(1-\alpha a^t)\left(1+\frac{\alpha a^t}{s+3}\right)\right]^{p/s}} \quad (8)$$

Next, eq (8) can be approximated as follows:

$$\delta_n(p, s)\cong\delta_\infty(p, s)[1-C_1(a\alpha^{1/t})^{p+3}][1-C_2(p/s-1)(a\alpha^{1/t})^3]\cdot[1+C_3p/s(a\alpha^{1/t})^{s+3}] \quad (9)$$

with

$$C_1=\left[\Gamma\left(\frac{p+3}{t}\right)\right]^{-1}\cdot\left(\frac{t}{p+3}\right),$$

$$C_2=\left[\Gamma\left(\frac{3}{t}\right)\right]^{-1}\frac{t}{3},$$

$$C_3=\left[\Gamma\left(\frac{s+3}{t}\right)\right]^{-1}\frac{t}{s+3}.$$

In eq (9), one notices that the deviation of $\delta_n(p, s)$ from its limiting value of δ_∞ comes primarily from the integral associated with the normalization condition. This is because the normalization integral, $4\pi\int_0^\infty r^2e^{-\alpha r^t}dr$ involves the lowest power of r. Therefore, for large n (i.e., for $\alpha a^t<<1$), the first-order correction to δ_∞ can be written as

$$\delta_n\cong\delta_\infty[1-C_2(p/s-1)(a\alpha^{1/t})^3]. \quad (10)$$

C_2 is here close to unity in its value. Thus, to a first approximation, δ_n/δ_∞ for a given value of s is a constant, independent of p, provided that n is large enough for the approximations leading to eqs (8) and (9) to be valid.

In order to examine the dependence of δ_n/δ_∞ on p, for given s, one has to consider the second dominant term in the expansion of eq (8), which is brought up by the denominator of this equation. To this approximation

$$\delta_n\cong\delta_\infty[1-C_2(p/s-1)(a\alpha^{1/t})^3][1+C_3p/s(a\alpha^{1/t})^{s+3}] \quad (11)$$

and, therefore, δ_n/δ_∞ is expected to decrease with increasing p for fixed values of s. The following table of $\delta_{40}/\delta_\infty$ for $s=2$ confirms this observation.

p	$\delta_{40}/\delta_\infty$
2	0. 865
4	. 852
6	. 832
8	. 809

Another qualitative check of our results can be made on the basis of data presented in figures 4 and 5. These two figures represent the same value of p but different values of s. From eq (10) it is obvious that increasing s will have an effect of slightly decreasing the corresponding value of δ_n/δ_∞. Here, again, we have $\delta_{40}/\delta_\infty=0.832$ for $s=2$, and $\delta_{40}/\delta_\infty=0.827$ for $s=3$, in qualitative agreement with these analytical considerations.

The dependence of δ_n on n for the asymptotic case of large n can be estimated from the following: If one assumes that $\langle r_n^2\rangle\sim An^\gamma$ (A and γ are numerical constants), then from $\alpha\propto\frac{1}{\langle r_n^2\rangle^{t/2}}$ one obtains that $\alpha\propto\frac{1}{n^{\gamma t/2}}$. Hence, $\delta_n/\delta_\infty\sim 1-0\left(\frac{1}{n^2}\right)$, for $\gamma=1.25$ and $t=3.2$, and the δ_n versus $1/n$ curves should not be straight lines but somewhat concave upward in the vicinity of $1/n=0$. Therefore, somewhat lower values for t than the extrapolated value of $t=3.2$ (based on linear extrapolation of data shown in the inserts in figs. 1 through 5) might be expected.

Another aspect worth noticing is the tremendous influence of a, the radius of closest approach, on the

shape of the curves in our figures. The correction term to $\delta_\infty(p, s)$ is proportional to at least the cube of the radius of closest approach. For this reason it is not surprising to find that in the case of excluded volume restricted to only self-intersections the limiting value of $\delta_n(p, s)$ is reached almost immediately, as n increases, as shown by Fisher and Hiley [11], while in our case with larger a, it is reached considerably slower.

3. Discussion

The polymer distribution function for the chain-end displacement to have its absolute value in the range between r and $r+dr$ is given by

$$W(r)dr=\frac{t\alpha^{3/t}r^2\exp(-\alpha r^t)dr}{\Gamma(3/t)}=\frac{t}{\Gamma(3/t)}\left[\frac{\Gamma(5/t)}{\Gamma(3/t)\langle r^2\rangle}\right]^{3/2}r^2 \exp\left[-\left(\frac{\Gamma(5/t)}{\Gamma(3/t)}\frac{r^2}{\langle r^2\rangle}\right)^{t/2}\right]dr. \quad (13)$$

For a Markov-type polymer chain, $t=2$, while for a nonself intersecting chain $t=3.2$. The latter value seems to be independent of the size of volume exclusion in the asymptotic case of an infinitely long chain. The comparison of these two representations of polymer chains is shown in figure 6, in which $W(r)$ is plotted versus $r/\langle r^2\rangle^{1/2}$ for a Gaussian chain ($t=2$) and for a nonself intersecting chain ($t=3.2$). For $\langle r^2\rangle$, the value of $\langle r^2\rangle=200l^2$ was taken; l, the length of a single polymer link is conveniently assumed to have a value of one.

The shapes of these two curves are consistent with the general trend of the effect of excluded volume on the shape of the distribution function, as pointed out by Verdier and Stockmayer [9]. Compared to the Gaussian distribution, the distribution function is deficient at low values of r. The tail part for large extension has a sharper cutoff, as is the case for a real polymer chain. To compensate for these effects, more polymer configurations are crowded around the mean distance. In figure 6, the position of $\langle r\rangle/\langle r^2\rangle^{1/2}$ is shown for both types of polymer chain-end distributions. In the case of a non-Gaussian chain the value of $\langle r\rangle$ agrees better with the most probable polymer configuration. This latter fact is open to experimental verification.

The fact that the polymer distribution function (or, rather, its shape) is so simply determined from certain combinations of its moments does not imply that the proposed form is the only one that could be correct. As a matter of fact, even if the single-term exponential form for the polymer distribution function were correct for the case for which it was obtained, namely, for an infinitely long polymer, this does not imply that the same function will correctly describe the entire range of polymer dimensions. It could well be that the exact polymer distribution function is built of several terms, which either converge to the form derived in this work as $n\to\infty$, or, this single-term expression for the distribution function is all that is eventually left. A straightforward procedure to determine the polyme distribution function would be to calculate as many moments as it is practically possible, within the storage capacities of digital computers. Then, one can derive enough terms of a moment-generating function in order to calculate the distribution function using an inversion formula. However, we would prefer rather to test first our single-term polymer distribution function with existing experimental data, whenever applicable, and, if there is a need to do so, to seek a more exact representation.

The two computational results, our eq (13) and another relation which determines the dependence of the parameter α (or, the mean square distance $\langle r_n^2\rangle$) on the number of steps n should complete the entire picture of the statistics of polymer end-to-end distances. Either one of these two relationships should be regarded as a compromise rather than as a rigorous expression.

In the case of a polymer which can be adequately described as Markovian (i.e., which is devoid of excluded volume effect which results from existence of long-range intramolecular correlations), the "polymer structure index" $\gamma=1$ and $t=2$. (γ is defined as $(\langle r_{n+1}^2\rangle/\langle r_n^2\rangle-1)n$ in the limit of $n\to\infty$, assuming that such limiting value exists.) Otherwise, γ can have any value between 1 and 2 (depending on the size of the excluded volume) and $t=3.2$. If our assumption that t does not depend on the kind of a lattice, only on its dimensionality, is correct, then it is this parameter which shows, that the two classes of random walks on a lattice, the intersecting and the nonself intersecting ones, represent two distinct topological structures. A transition from one class to another class would be impossible without first breaking through the chain bonds. However, the size of the excluded volume (or the range of hard-sphere potential energy for intramolecular repulsion) does not affect the topology (or the parameter t) of the chain.

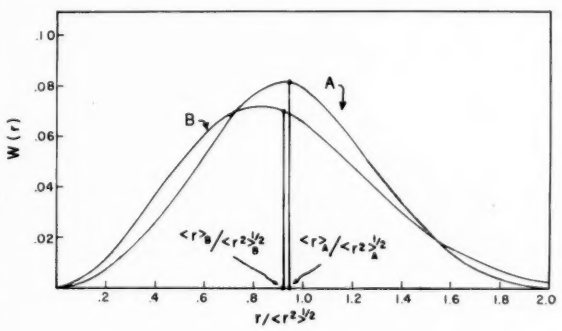

FIGURE 6. *The chain-end distribution function for random walk on a simple cubic lattice with excluded unit-distance approaches (curve A) and for unrestricted Gaussian-type random walk on the same lattice (curve B).*

In both cases $\langle r_n^2\rangle$ = 200×unit step length.

4. Appendix

Unless one considers very high moments, it is obvious that the so-called "fractional moments" δ_n are rather insensitive to the tail-part of the chain-end distribution function. For this reason, one could expect that other forms for the radial distribution functions of the general form

$$W(r)dr=Ar^l \exp(-\alpha r^t)dr \qquad \text{(A1)}$$

with $l \neq 2$, could lead to the correct results in terms of $\delta(p, s)$. Recently Professor Domb [12] indicated that for a simple nonintersecting random walk on a cubic lattice the general form for $W(r)$ is the above relation with $l=t$ and $t=2.5$. We checked this particular form for the distribution function, based on the proposition that $l=t$, with our data and found that for this model the value of $t=2.58$ leads to a good agreement between the computed values of $\delta(p, s)$ and these quantities as calculated from the moments of this distribution function. Moreover, if curve A of figure 6 is replaced by the distribution function with $l=t$, while retaining all other parameters, the resulting curve will overlap almost exactly curve A, except for its tail-part. The advantage of the radial distribution function with $l=t$ lies in the fact that $W(x)dx$, the distribution of a rectangular coordinate will then assume a simple single-term exponential function with the same exponent as in the radial function, namely

$$W(x)dx=A \exp[-\alpha|x|^t]dx \qquad \text{(A2)}$$

while in our case this simple form for $W(x)$ is not obtainable [14]. As a matter of fact, a rectangular coordinate chain-end distribution function will then be given by

$$W(x)dx=\frac{\alpha^{1/t}}{2\Gamma\left(\frac{3}{t}\right)}\int_{\alpha x^t}^{\infty} y^{\left(\frac{2}{t}-1\right)}e^{-y}dydx \qquad \text{(A3)}$$

assuming, as we did, that $l=2$. Of course, when $t=2$, either approach leads to the well-known one- and three-dimensional Gaussian distributions.

These considerations are illustrated in table 1 and figure 7. In table 1, the extrapolated values for $\delta(p, p/2)$ are shown, together with the data calculated from the following equation for $\delta(p, p/2)$ which is based on the general form for the chain-end distribution function given by eq (A1)

$$\delta\left(p, \frac{p}{2}\right)=\frac{\Gamma\left(\frac{p+l+1}{t}\right)\Gamma\left(\frac{l+1}{t}\right)}{\left[\Gamma\left(\frac{\frac{p}{2}+l+1}{t}\right)\right]^2}-1 \qquad \text{(A4)}$$

for the following cases:

(1) $l=2, t=3.2$
(2) $l=t=2.6$
(3) $l=2.1, t=3.0$.

For comparison, the values of $\delta(p, p/2)$ for Gaussian distribution are also presented.

TABLE 1. *Comparison of Monte Carlo computation of* δ(p,p/2) *with values obtained from eq (A4)*

	Monte Carlo computation	$l=2, t=3.2$	$l=t=2.6$	$l=2.1, t=3.0$	$l=t=2.0$ (Gaussian)
δ (2, 1)	0.126	0.127	0.120	0.127	0.178
δ (4, 2)	.442	.438	.433	.446	.667
δ (6, 3)	.958	.939	.967	.968	1.577
δ (8, 4)	1.735	1.696	1.816	1.770	3.200

The case of $l=2.1$ and $t=3.0$ was found from computations of eq (A4) performed on a high-speed computer, as representing the best fit of results based on eq (A4) and the numerical data based on the Monte Carlo computations. This is shown in figure 7, in which l is plotted versus t for each of the four "reduced" moments $\delta(p, p/2)$. Therefore, our data justify the a priori assumption that $l=2$.

In spite of this agreement, the justification for our radial distribution function with $l=2$ is more heuristic than rigorous, owing to the uncertainty in extrapolated data based on higher moments. Thus, the total volume of all volume elements at a distance r is $4\pi r^2 dr$, which is proportional to the number of possible positions between r and $r+dr$ on a lattice. And, indeed, Wall, Windwer, and Gans [8] found that the number of possible sites on a tetrahedral lattice is approximately proportional to r^2. Thus, our distribution function retains the volume element, multiplied by a single term which represents the exponential decay of the distribution.

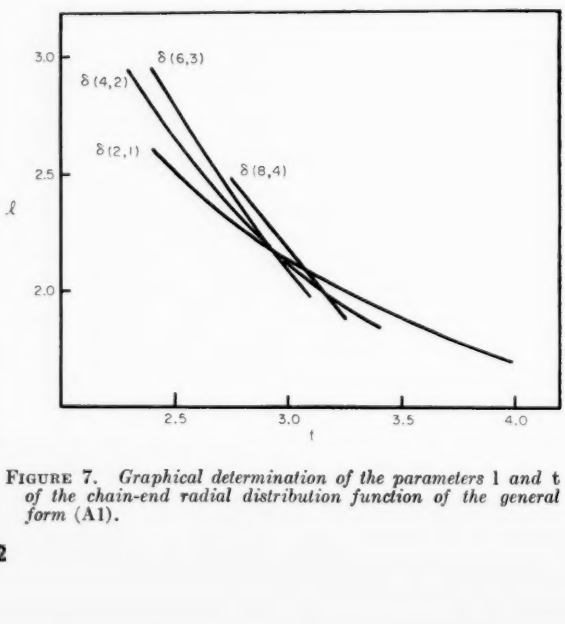

FIGURE 7. *Graphical determination of the parameters* l *and* t *of the chain-end radial distribution function of the general form* (A1).

However, the behavior of the distribution function as $r \to 0$ is hard to ascertain owing to the lattice effects. The indications on the basis of previous Monte Carlo calculations [8–10] are that $l > 2$ represents a better description near the origin, than the case with $l = 2$.

In the case of the general form of the distribution function of eq (A1) which involves two parameters, the Monte Carlo approach used here is not sensitive enough to determine a unique pair of the parameters l and t. This is because very few samples are generated in the tail-part of the distribution which, in turn, is particularly sensitive to the exponent-parameter t. One can improve the accuracy of our computations only if higher moments than the eighth moment are calculated. For this reason, one should generate enough samples for chains which are considerably longer than the ones generated by us, since the higher-order moments are more sensitive to the "lattice effects" than are the lower ones. We hope to undertake these computations in the future.

(Paper 69A4–355)

5. References

[1] M. Fisz, Probability Theory and Mathematical Statistics, ch. 6. (John Wiley & Sons, New York, N.Y., 1963.)

[2] M. Fisz, ch. 7, p. 264. At the end of this chapter there is an extensive bibliography for conditions for the validity of the Central Limit Theorem for Markov chains.

[3] J. Mazur, J. Chem. Phys. **41,** 2256 (1964).

[4] E. Montroll, Ann. of Math. Statist. **18,** 18 (1947).

[5] On long-range orders in lattices see, for example, G. F. Nqwell and E. Montroll, Rev. Modern Physics **25,** 353 (1953); J. Ashkin and W. E. Lamb, Physical Review **64,** 159 (1943).

[6] G. Frobenius, Sitzungsberichte, 451, 1912; also, G. Debreu and I. N. Herstein, **21,** 597 (1953).

[7] G. Frobenius, Sitzungsberichte, 514 (1909).

[8] F. T. Wall, S. Windwer, and P. J. Gans, J. Chem. Phys. **38,** 2220 (1963).

[9] P. H. Verdier and W. H. Stockmayer, J. Chem. Phys. **36,** 227 (1962).

[10] T. F. Schatzki, J. Poly. Sci. **57,** 337 (1962).

[11] M. E. Fisher and B. J. Hiley, J. Chem. Phys. **34,** 1253 (1961).

[12] C. Domb, private communication. (See ref. [15].)

[13] Handbook of Mathematical Functions, NBS Applied Mathematics Series, pp. 262 and 504.

[14] L. R. G. Treloar, Trans Faraday Soc. **42,** 77 (1946).

[15] The work mentioned in ref. 12 was in press at the time this manuscript was being prepared for print: C. Domb, J. Gillis, and G. Wilmers, Proc Phys. Soc. **85,** 625 (1965).

JOURNAL OF RESEARCH of the National Bureau of Standards—A. Physics and Chemistry
Vol. 69A, No. 4, July–August 1965

An Additivity Rule for the Vapor Pressure Lowering of Aqueous Solutions

R. A. Robinson and V. E. Bower

(March 30, 1965)

The question is discussed whether, and to what extent, the vapor pressure lowering of an aqueous solution containing two salts A and B can be compounded additively from the vapor pressure lowerings of a solution containing the salt A alone and another solution containing the salt B alone. In some instances the additivity of vapor pressure lowering is true within less than 0.5 percent; six systems have been examined and the greatest deviation from additivity amounts to 2.0 percent.

1. Introduction

It has been shown [1] [1] that in some instances the vapor pressure lowering of a solution of two salts is approximately an additive effect of the vapor pressure lowering due to each salt separately. If this could be established, vapor pressure data for many three-component systems containing water and two salts could be calculated from known data for aqueous solutions of single salts. Moreover, related properties of aqueous solutions of two salts, such as osmotic pressure, freezing point depression, boiling point elevation, could also be calculated. The rule, even if only approximately true, could have many practical applications.

The additivity rule can be illustrated as follows. In a study of the system water-sodium chloride-barium chloride [2] it was found that at 25 °C a solution 1.0073 m with respect to sodium chloride and 1.0448 m with respect to barium chloride was in vapor phase equilibrium with a solution containing sodium chloride only at a concentration 2.6185 m. The vapor pressure lowerings of solutions of sodium chloride at 25 °C have been tabulated [3] and it can be shown that a solution 2.6185 m in sodium chloride has a vapor pressure 2.181 mm Hg lower than that of pure water at the same temperature. The vapor pressure lowering of the mixed solution of sodium chloride and barium chloride must be the same, 2.181 mm Hg.

There are many ways by which we could attempt to predict this vapor pressure lowering. We could assume that the lowering was the sum of that due to a solution containing sodium chloride only at a concentration of 1.0073 m and that due to a solution of barium chloride only at a concentration of 1.0448 m. Since the vapor pressure lowering of the sodium chloride solution is 0.7929 mm Hg and that of the barium chloride solution is 1.232 mm Hg, the predicted value for the mixed solution is 2.025 mm Hg, which is not in good agreement with the observed value.

We might use relative molal vapor pressure lowering at total ionic concentrations equal to that of the mixed solution. The total ionic concentration of the mixed solution in $1.0073+1.5\times1.0448=2.5755$. At this concentration the relative molal vapor pressure lowering, $(p°-p)/(mp°)$, of a sodium chloride solution is 0.03500 and hence the predicted contribution of sodium chloride is 0.8374 mm Hg. Similarly, the relative molal vapor pressure lowering of a barium chloride solution at this total ionic concentration is 0.05421, so that the predicted contribution of barium chloride is 1.343 mm Hg, the total contribution being 2.282 mm Hg. Again, this does not agree well with the observed value.

A third possibility is to compare solutions of the same total ionic strength. The total ionic strength of the mixed solution is 4.1417; a solution containing sodium chloride only at this total ionic strength is 4.1417 m. Its relative molal vapor pressure lowering, $(p°-p)/(mp°)$, at this total ionic strength is 0.03734 and the vapor pressure lowering per mole of salt, $(p°-p)$, is 0.8869 mm Hg. The additivity rule requires that we use the vapor pressure lowering per mole of salt at the total ionic strength of the mixed solution. Hence the contribution to the vapor pressure lowering due to the 1.0073 moles of sodium chloride is 0.8934 mm Hg. A solution containing barium chloride only at a total ionic strength of 4.1417 is 1.3806 m in concentration. The vapor pressure lowering per mole of barium chloride at this concentration is 1.234 mm Hg or 1.289 mm Hg for

[1] Figures in brackets indicate the literature references at the end of this paper.

the 1.0448 moles of barium chloride in the mixed solution. If the vapor pressure lowering of the mixed solution is truly additive, a lowering of 2.182 mm Hg is predicted, which compares very well with the observed value of 2.181 mm Hg.

It is the purpose of this paper to consider data for this salt pair at other concentrations and data for other systems, especially those containing an alkali metal chloride and an alkaline earth metal chloride.

2. Vapor Pressure Lowerings of Single Salt Solutions

Values of the relative molal vapor pressure lowerings, $(p°-p)/(mp°)$ of both sodium chloride and potassium chloride solutions have been tabulated [3]. It will be convenient to tabulate similar data for solutions of calcium chloride and of barium chloride. The osmotic coefficients of solutions of barium chloride are known [2]; they are related to the vapor pressure of the solution by the expression:

$$-3m\varphi = 55.51 \ln (p/p°)$$

and, therefore values of $(p°-p)/(mp°)$ can be calculated. They are given in table 1. Values for calcium chloride solutions can be calculated from osmotic coefficient data for this salt [3]; they are also given in table 1.

TABLE 1. *Relative molal vapor pressure lowering of solutions of calcium chloride and of barium chloride at 25 °C*

m	$(p°-p)/(mp°)$	
	$CaCl_2$	$BaCl_2$
0.1	0.04605	0.04541
.2	.04637	.04510
.3	.04701	.04530
.4	.04793	.04570
.5	.04894	.04619
.6	.05001	.04676
.7	.05113	.04736
.8	.05232	.04800
.9	.05363	.04866
1.0	.05504	.04933
1.1	.05637	.05002
1.2	.05773	.05071
1.3	.05914	.05141
1.4	.06056	.05210
1.5	.06198	.05278
1.6	.06340	.05346
1.7	.06481	.05411
1.8	.06623	.05475
1.9	.06767	.05536
2.0	.06910	.05593

3. Solutions of Sodium Chloride and Potassium Chloride at 25 °C

The vapor pressures of a number of solutions containing both sodium chloride and potassium chloride have been determined [4]. Some of these data are used to study the additivity rule; the results are given in table 2. The first column gives the molality M_{NaCl}, of a solution containing sodium chloride only, in isopiestic (vapor phase) equilibrium with a solution of potassium chloride and sodium chloride with molalities given in the second and third columns. The fourth column gives the vapor pressure lowering observed in this isopiestic experiment and the fifth column that calculated by the additivity rule. The last column gives the percentage difference between the observed and calculated vapor pressure lowerings.

TABLE 2. *Vapor pressure lowerings of solutions of sodium chloride and potassium chloride at 25 °C*

M_{NaCl}	m_{KCl}	m_{NaCl}	$(p°-p)$mm Hg		Δ[a]
			obs.	calc.	
0.5012	0.3099	0.1995	0.3917	0.3923	0.2
1.0493	.5177	.5571	.8268	.8300	.6
1.6223	.8581	.8244	1.299	1.309	.8
2.3248	.9701	1.4490	1.913	1.933	1.1
3.3188	1.5328	1.9780	2.845	2.884	1.4
4.0043	2.1391	2.1700	3.532	3.592	1.7
4.4461	3.1963	1.7241	3.994	4.066	1.8
4.6857	1.6005	3.3522	4.247	4.318	1.7

[a] Δ is the percentage difference between observed and calculated vapor pressure lowerings.

4. Solutions of an Alkali Metal Chloride and Alkaline Earth Metal Chloride at 25 °C

Tables 3 through 6 give similar data for the following salt pairs:

$NaCl-CaCl_2$
$KCl-CaCl_2$
$NaCl-BaCl_2$
$KCl-BaCl_2$

TABLE 3. *Vapor pressure lowerings of solutions of sodium chloride and calcium chloride at 25 °C*

M_{NaCl}	m_{NaCl}	m_{CaCl_2}	$(p°-p)$mm Hg		Δ[a]
			obs.	calc.	
0.5339	0.2495	0.1968	0.4173	0.4150	0.6
1.0420	.4375	.3929	.8207	.8109	1.2
1.5186	.5078	.6248	1.211	1.194	1.4
2.7546	1.2728	.8300	2.307	2.265	2.0
3.4285	1.2284	1.1858	2.952	2.902	1.7
4.5821	2.1539	1.2356	4.137	4.047	2.2
5.4851	3.8795	0.7894	5.124	5.036	1.7

[a] Δ is the percentage difference between observed and calculated vapor pressure lowerings.

TABLE 4. *Vapor pressure lowerings of solutions of potassium chloride and calcium chloride at 25 °C*

M_{KCl}	m_{KCl}	m_{CaCl_2}	$(p°-p)$mm Hg		Δ[a]
			obs.	calc.	
1.5135	0.9350	0.3559	1.141	1.135	0.5
1.5240	.7744	.4569	1.149	1.143	.5
2.7872	1.9415	.4654	2.121	2.110	.5
2.7986	1.4805	.7194	2.130	2.126	.2
2.7986	1.0515	.9406	2.130	2.128	.1

[a] Δ is the percentage difference between observed and calculated vapor pressure lowerings.

TABLE 5. *Vapor pressure lowerings of solutions of sodium chloride and barium chloride at 25 °C*

M_{NaCl}	m_{NaCl}	m_{BaCl_2}	$(p°-p)$ mm Hg		△[a]
			obs.	calc.	
0.5044	0.2213	0.2037	0.3941	0.3926	0.4
1.2328	.6389	.4092	.9746	.9722	.2
1.5683	.2721	.8790	1.253	1.255	.2
2.0021	1.0496	.6303	1.626	1.622	.2
2.3615	1.1799	.7744	1.946	1.948	.1
2.7147	1.3969	.8514	2.270	2.272	.1
2.7147	0.6356	1.3458	2.270	2.276	.3

[a] △ is the percentage difference between observed and calculated vapor pressure lowerings.

TABLE 6. *Vapor pressure lowerings of solutions of potassium chloride and barium chloride at 25 °C*

M_{KCl}	m_{KCl}	m_{BaCl_2}	$(p°-p)$ mm Hg		△[a]
			obs.	calc.	
0.7899	0.4185	0.2603	0.5987	0.5982	0.1
1.0743	.5648	.3514	.8112	.8133	.3
1.5519	.2358	.8588	1.170	1.177	.6
2.2466	.8579	.8894	1.701	1.725	1.4
2.7188	.5746	1.3145	2.068	2.095	1.3
2.7763	1.5011	0.8090	2.112	2.055	2.0
2.8600	.9462	1.1832	2.178	2.216	1.7

[a] △ is the percentage difference between observed and calculated vapor pressure lowerings.

In each table the first column gives the molality of the single salt solution (sodium chloride or potassium chloride) in isopiestic equilibrium with the solution containing two salts at molalities given in the third and fourth columns. The next two columns give observed and calculated values of the vapor pressure lowering and the last column the percentage difference between observed and calculated values.

The data for the sodium chloride-barium chloride system are taken from a previous publication [2]; the data for the other systems are new.

5. System Containing Three Solutes

A few measurements have been made on the four component system water-sodium chloride-potassium chloride-barium chloride, with the results given in table 7.

TABLE 7. *Vapor pressure lowerings of solutions of sodium chloride, potassium chloride, and barium chloride at 25 °C*

M_{NaCl}	m_{NaCl}	m_{KCl}	m_{BaCl_2}	$(p°-p)$ mm Hg		△[a]
				obs.	calc.	
1.4218	0.4708	0.4708	0.3559	1.130	1.139	0.8
1.4174	.3110	.3110	.5654	1.126	1.134	.7
1.4174	.1740	.1740	.7449	1.126	1.133	.6
1.4174	.1127	.1127	.8250	1.126	1.133	.6
2.5903	1.1980	1.1980	.2126	2.155	2.177	1.0
2.5903	1.0281	1.0281	.4292	2.155	2.180	1.2
2.5567	0.5509	0.5509	1.0022	2.124	2.148	1.1
2.5567	.3521	.3521	1.2443	2.124	2.145	1.0

[a] △ is the percentage difference between observed and calculated vapor pressure owerings.

6. Summary

The validity of the additivity rule can be appreciated by considering the percentage difference between observed and calculated vapor pressure lowerings and especially the upper and lower limits of these percentage differences for each system. These are as follows:

	%
NaCl-KCl	0.2–1.8
NaCl-$CaCl_2$	.6–2.2
KCl-$CaCl_2$	.1–0.5
NaCl-$BaCl_2$	.1–0.4
KCl-$BaCl_2$	.1–2.0
NaCl-KCl-$BaCl_2$	.6–1.2

The agreement is very good in some instances, for example, the potassium chloride-calcium chloride system and the sodium chloride-barium chloride system. Even in the worst case the difference is only 2 percent. This is not tolerable in an investigation of the more detailed interactions of multicomponent salt solutions. It may, however, be of sufficient accuracy in other applications; a decision can only be made with the object of an application of this additivity rule in mind.

Grateful acknowledgment is made to the Office of Saline Water for a grant in partial support of this work.

7. References

[1] R. A. Robinson and R. H. Stokes, Trans. Faraday Soc. **41,** 752 (1945).
[2] R. A. Robinson and V. E. Bower, J. Res. NBS 69A (Phys and Chem) No. 1, 19–27 (1965).
[3] R. A. Robinson and R. H. Stokes, Electrolyte solutions, appendix 8.3, 2d. ed. (Butterworths Scientific Publications, London, 1959).
[4] R. A. Robinson, J. Phys. Chem. **65,** 662 (1961)

(Paper 69A4–356)

JOURNAL OF RESEARCH of the National Bureau of Standards—A. Physics and Chemistry
Vol. 69A, No. 4, July–August 1965

Franck-Condon Factors to High Vibrational Quantum Numbers V: O_2 Band Systems

R. W. Nicholls [1]

(March 12, 1965)

Franck-Condon factors arrays have been computed numerically and are displayed to highest known vibrational quantum numbers for the following O_2 band systems:

Herzberg I:	$(A^3\Sigma_u^+ - X^3\Sigma_g^-)$
Herzberg II:	$(c^1\Sigma_u^- - X^3\Sigma_g^-)$
Herzberg III:	$(D^3\Delta_u - X^3\Sigma_g^-)$
Chamberlain:	$(D^3\Delta_u - a^1\Delta_g)$
Broida-Gaydon:	$(A^3\Sigma_u^+ - b^1\Sigma_g^+)$
Noxon:	$(b^1\Sigma_g^+ - a^1\Delta_g)$
Atmospheric	$(b^1\Sigma_g^+ - X^3\Sigma_g^-)$
Infrared Atmoshperic:	$(a^1\Delta_g - X^3\Sigma_g^-)$

1. Introduction

The most important band systems of O_2, most of which have applications in aeronomy, are listed in table 1 with descriptive comments. They are also indicated in the simplified energy level diagram (figure 1). They cover the broad spectral region from the vacuum ultraviolet to the near infrared. Most of them are hard to excite in emission in simple discharges for one of two reasons. Either excitation from the ground state to the upper state concerned results in dissociation because of the relative position of the potentials, and the operation of the Franck-Condon principle (e.g., Schumann-Runge and Herzberg I systems) or even if the bound upper state can be excited from the ground state, the emission transitions from the upper state are often forbidden for dipole radiation (e.g., Herzberg II, Chamberlain, Broida-Gaydon, Atmospheric and Infrared Atmospheric), and the excited molecules are depopulated by collisions with other molecules or the walls before they can radiate. Special light sources have therefore been developed for emission studies [Feast, 1949, Broida and Gaydon 1954, Broida and Peyron 1960, Barth and Patapoff, 1962]. Further, the preponderance of forbidden transitions involving the ground state indicates the need for long path lengths and exposure times for absorption studies. [Herzberg and Herzberg, 1947, Babcock and Herzberg 1948, Ditchburn and Heddle, 1954, Ditchburn and Young, 1962]. The band systems are well documented in the compilations of Wallace [1962] and of Pearse and Gaydon [1963].

[1] Visiting Professor, Department of Aeronautics and Astronautics, Stanford University, Stanford, Calif., on leave from The University of Western Ontario, London, Canada. Now in Department of Physics, York University, Toronto.

TABLE 1. *Band systems of* O_2

Band system	Wavelength range (Å)	Reference
Schumann-Runge $(B^3\Sigma_u^- - X^3\Sigma_g^-)$	1751–5720	[1]
Herzberg I $(A^3\Sigma_u^+ - X^3\Sigma_g^-)$	2429–4881	[2]
Herzberg II $(c^1\Sigma_u^- - X^3\Sigma_g^-)$	2540–6541	[3]
Herzberg III $(D^3\Delta_u - X^3\Sigma_g^-)$	2570–2630	[3]
Broida-Gaydon $(A^3\Sigma_u^+ - b^1\Sigma_g^+)$	3596–5631	[4]
Chamberlain $(D^3\Delta_u - a^1\Delta_g)$	3696–4379	[5]
Atmospheric $(b^1\Sigma_g^+ - X^3\Sigma_g^-)$	5795–8645	[6]
Infrared atmospheric $(a^1\Delta_g - X^3\Sigma_g^-)$	10,600–15,800	[7]
Noxon $(b^1\Sigma_g^+ - a^1\Delta_g)$	19,100	[8]

References:
[1] Feast (1949).
[2] Herzberg (1952).
[3] Herzberg (1953).
[4] Broida and Gaydon (1954).
[5] Chamberlain (1958).
[6] Babcock and Herzberg (1948).
[7] Herzberg and Herzberg (1947).
[8] Noxon (1961).

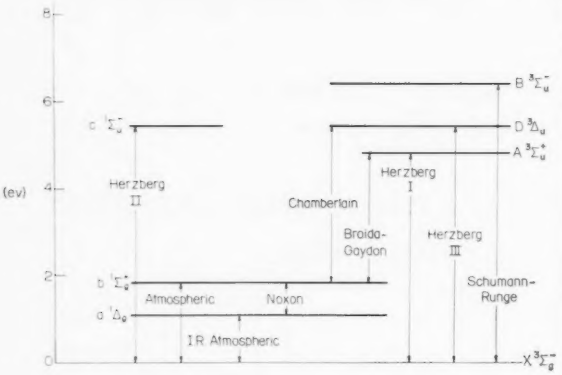

FIGURE 1. *Partial energy level diagram for* O_2.

The band strength $S_{v'v''}$ defined in eq (1) in terms of Franck-Condon factor $q_{v'v''}$ and the electronic transition moment $R_e(\bar{r}_{v'v''})$ determines, apart from powers of frequency, such important transition probability parameters as band absorption coefficient $k_{v'v''}$, band oscillator strength $f_{v'v''}$, band Einstein A and B coefficients $A_{v'v''}$, $B_{v'v''}$ and integrated emission intensity of the band $I_{v'v''}$, as indicated in eqs (2a–e). $\bar{r}_{v'v''}$ is the r-centroid of the band.

$$S_{v'v''}=R_e^2(\bar{r}_{v'v''})q_{v'v''} \tag{1}$$

$$B_{v'v''}\propto S_{v'v''} \tag{2a}$$

$$k_{v'v''}\propto \nu_{v'v''}S_{v'v''} \tag{2b}$$

$$f_{v'v''}\propto \nu_{v'v''}S_{v'v''} \tag{2c}$$

$$A_{v'v''}\propto \nu_{v'v''}^3 S_{v'v''} \tag{2d}$$

$$I_{v'v''}\propto \nu_{v'v''}^4 S_{v'v''} \tag{2e}$$

Thus, as is well known, and has been pointed out in earlier papers of this series [Nicholls, 1961], the Franck-Condon factors exert a proportional and dominating influence on the transition probability parameters and intensity distributions within a band system.

It is the purpose of this paper, which is one of a series treating astrophysically and aeronomically important band systems, to present tables of Franck-Condon factors to high quantum numbers for all the band systems of O_2 listed in table 1 except for the Schumann-Runge system, which has been treated previously [Nicholls, 1960].

2. Method

The straightforward method of computer-based calculation described in the first paper of the series [Nicholls, 1961] was used and the calculations were performed in the computation center of the National Bureau of Standards. Input data are ω_e, $\omega_e x_e$, r_e, and v_{max} for each of the electronic states involved, and μ_A for the molecular species in question. The notation is conventional [Herzberg, 1950]. The Morse model of molecular potentials is adopted and the computer program provides all needed Morse vibrational wavefunctions and their overlap integral squares, the Franck-Condon factors. The Morse potential is admittedly an empirical expedient, but for many of the systems treated here the range of vibrational quantum numbers involved is sufficiently small that it is probably realistic. Further, in many cases, the molecular constants needed for evaluation of a more realistic potential are not available (see sec. 4, discussion).

The input data employed in the calculations are summarized with references in table 2. These data were obtained from original papers with the exception of the D $^3\Delta_u$ and A $^3\Sigma_u^+$ states. Constants for the D $^3\Delta_u$ state were computed as follows: Herzberg's [1953] absorption measurements on the $v''=0$, $v'=6$ and $v''=0$, $v'=5$ bands provided B_v values for the $v'=5$ and 6 levels from which $\alpha_e=0.0262$ cm^{-1}, $B_e=0.9618$ cm^{-1}, and $r_e=1.4802$ Å were derived. Chamberlain's [1958] measured values of $\Delta G(5\frac{1}{2})$, $\Delta G(4\frac{1}{2})$, $\Delta G(3\frac{1}{2})$ led to the values of $\omega_e=791$ cm^{-1}, $\omega_e x_e=15$ cm^{-1}. Broida and Gaydon [1954] showed from emission measurements on the Herzberg I system that the vibrational numbering of the A $^3\Sigma_u^+$ state should be raised one unit above the values proposed by Herzberg [1952] from absorption studies. New ω_e, $\omega_e x_e$, and r_e values were therefore calculated for this state.

TABLE 2. *Basic data*

State	ω_e(cm^{-1})	$\omega_e x_e$(cm^{-1})	r_e(Å)	v_{max}	Reference
$X^3\Sigma_g^-$	1580.3613	12.073	1.207398	12	[1]
$A^3\Sigma_u^+$	802.795	14.635	1.514	12	[2, 3]
$D^3\Delta_u$	791	15	1.4802	6	[3, 4, 5]
$a^1\Delta_g$	1509.03	12.9	1.2155	5	[1]
$b^1\Sigma_g^+$	1432.687	13.95	1.22675	3	[1]
$c^1\Sigma_u^-$	650.49	17.036	1.597	6	[4]

$\mu_A=8.0000$ for all states

References:
[1] Herzberg (1950).
[2] Herzberg (1952).
[3] See comments in text.
[4] Herzberg (1953).
[5] Chamberlain (1958).

3. Results

Franck-Condon factor arrays are displayed in tables 3 through 10 for the band systems listed in table 1 with the exception of the Schumann-Runge system. The Condon loci [Nicholls, 1963; Murty, 1964] are indicated on the tables by setting entries for bands which lie on the local maxima of the Franck-Condon factor surfaces in bold-faced type. The large change in r_e which is associated with the

Herzberg I, II, III, Chamberlain and Broida-Gaydon systems, and which as was pointed out in the introduction makes them difficult to excite in conventional discharges, results in broad Condon loci well removed from (0, 0). The negative number in each entry is the power of ten by which it is multiplied.

4. Discussion

The Condon loci of tables 3 through 10 agree well with the v'-v'' positions of the commonly excited bands of each system [Pearse and Gaydon, 1963; Wallace, 1962].

TABLE 3. *Franck-Condon factors to high vibrational quantum numbers for the O_2 Herzberg I ($A^3\sum_u^+ - X^3\sum_g^+$) band system*

v' \ v''	0	1	2	3	4	5	6	7	8	9	10	11	12
0	2.4260−6	4.4311−5	3.8195−4	2.0682−3	7.9015−3	2.2677−2	5.0829−2	9.1339−2	**1.3404−1**	**1.6280−1**	**1.6531−1**	**1.4116−1**	**1.0235−1**
1	1.7963−5	2.8498−4	2.0854−3	9.3083−3	2.8188−2	6.0734−2	**9.4368−2**	**1.0346−1**	7.3138−2	2.3803−2	1.2404−5	2.7251−2	8.5565−2
2	7.1157−5	9.8205−4	6.0930−3	2.2262−2	5.2426−2	**8.0955−2**	7.7534−2	3.6282−2	1.2808−3	1.8045−2	**6.4243−2**	**7.4034−2**	3.3088−2
3	2.0058−4	2.4117−3	1.2665−2	3.7533−2	**6.6886−2**	6.8355−2	3.0189−2	1.6908−4	2.3655−2	**5.8664−2**	4.0520−2	2.3991−3	1.8152−2
4	4.5158−4	4.7377−3	2.1011−2	4.9907−2	6.4623−2	3.7362−2	1.8959−3	1.6340−2	**4.9053−2**	3.0215−2	1.0245−4	2.6875−2	**5.3812−2**
5	8.6424−4	7.9236−3	2.9593−2	**5.5466−2**	4.8946−2	1.0699−2	5.0153−3	**3.8195−2**	3.2349−2	8.4136−4	2.1383−2	**4.3836−2**	1.1637−2
6	1.4615−3	1.1729−2	3.6766−2	5.3252−2	2.8664−2	1.7439−4	2.1532−2	3.6878−2	6.4788−3	1.0003−2	**3.7852−2**	1.3644−2	4.6200−3
7	2.2417−3	1.5774−2	4.1336−2	4.4970−2	1.1800−2	3.9240−3	**3.2060−2**	1.9645−2	6.5648−4	2.8007−2	2.1810−2	3.3556−4	**2.8760−2**
8	3.1772−3	1.9640−2	**4.2823−2**	3.3623−2	2.2931−3	1.3620−2	3.0297−2	4.4361−3	1.1216−2	**2.8646−2**	2.9320−3	1.4582−2	2.8214−2
9	4.2188−3	2.2959−2	4.1422−2	2.2133−2	4.5604−5	2.1779−2	2.0519−2	4.6861−5	2.1899−2	1.5626−2	1.5959−3	**2.5866−2**	9.2906−3
10	5.3038−3	2.5470−2	3.7782−2	1.2527−2	2.6733−3	**2.4903−2**	9.7307−3	4.4418−3	**2.3701−2**	3.5597−3	1.1442−2	2.0832−2	1.2637−5
11	6.3645−3	2.7042−2	3.2741−2	5.7337−3	7.3200−3	2.3080−2	2.5272−3	1.1446−2	1.7762−2	3.7198−5	**1.9092−2**	8.6868−3	5.4809−3
12	7.3364−3	**2.7662−2**	2.7108−2	1.7830−3	**1.1771−2**	1.8219−2	2.6400−5	**1.6299−2**	9.4564−3	**3.5418−3**	1.8912−2	9.3510−4	1.4294−2

TABLE 4. *Franck-Condon factors to high vibrational quantum numbers for the O_2 Herzberg II ($c^1\sum_u^- - X^3\sum_g^-$) band system*

v' \ v''	0	1	2	3	4	5	6
0	4.9034−9	1.4332−7	1.9938−6	1.7584−5	1.1051−4	5.2734−4	1.9884−3
1	4.1810−8	1.1242−6	1.4242−5	1.1301−4	6.2969−4	2.6165−3	8.3984−3
2	1.8850−7	4.6808−6	5.4202−5	3.8821−4	1.9220−3	6.9550−3	1.8931−2
3	5.9754−7	1.3757−5	1.4616−4	9.4806−4	4.1804−3	1.3174−2	3.0257−2
4	1.4943−6	3.2023−5	3.1340−4	1.8477−3	7.2739−3	1.9960−2	3.8429−2
5	3.1363−6	6.2815−5	5.6860−4	3.0584−3	1.0779−2	2.5749−2	**4.1214−2**
6	5.7386−6	1.0787−4	9.0699−4	4.4689−3	1.4143−2	**2.9405−2**	3.8721−2

TABLE 5. *Franck-Condon factors to high vibrational quantum numbers for the O_2 Herzberg III ($D^3\Delta_u - X^3\sum_g^-$) band system*

v' \ v''	0	1	2	3	4	5	6
0	3.8288−5	5.0005−4	3.0975−3	1.2120−2	3.3656−2	7.0662−2	**1.1668−1**
1	2.4088−4	2.6265−3	1.3122−2	3.9516−2	7.9017−2	**1.0789−1**	9.7341−2
2	8.1643−4	7.4212−3	2.9636−2	6.6945−2	**9.0174−2**	6.6456−2	1.6013−2
3	1.9828−3	1.4999−2	4.7330−2	**7.7256−2**	6.1957−2	1.3511−2	4.8898−3
4	3.8726−3	2.4327−2	5.9784−2	6.6592−2	2.3978−2	8.7565−4	3.6053−2
5	6.4728−3	3.3690−2	**6.3271−2**	4.3737−2	2.3910−3	1.8602−2	**4.5742−2**
6	9.6233−3	**4.1397−2**	5.7949−2	2.0779−2	2.0654−3	**3.5565−2**	2.7272−2

TABLE 6. *Franck-Condon factors to high vibrational quantum numbers for the O_2 Broida-Gaydon ($A^3\sum_u^+ - b^1\sum_g^+$) band system*

v' \ v''	0	1	2	3
0	2.2109−5	3.5654−4	2.6485−3	1.2032−2
1	1.3876−4	1.8674−3	1.1145−2	3.8577−2
2	4.7218−4	5.3114−3	2.5349−2	6.5513−2
3	1.1574−3	1.0895−2	4.1317−2	**7.7474−2**
4	2.2911−3	1.8065−2	5.3976−2	7.0328−2
5	3.8947−3	2.5742−2	**5.9911−2**	5.0652−2
6	5.9050−3	3.2733−2	5.8463−2	2.8507−2
7	8.1905−3	3.8092−2	5.1199−2	1.1380−2
8	1.0582−2	4.1304−2	4.0705−2	2.1548−3
9	1.2903−2	**4.2286−2**	2.9494−2	4.6145−5
10	1.4998−2	4.1288−2	1.9398−2	2.5264−3
11	1.6748−2	3.8752−2	1.1403−2	6.9176−3
12	**1.8074−2**	3.5182−2	5.7788−3	1.1230−2

TABLE 7. *Franck-Condon factors to high vibrational quantum numbers for the O_2 Chamberlain ($D^3\Delta_u - a^1\Delta_g$) band system*

v' \ v''	0	1	2	3	4	5
0	8.8377−5	1.0910−3	6.3151−3	2.2808−2	5.7690−2	1.0874−1
1	5.1497−4	5.1932−3	2.3502−2	6.2355−2	**1.0543−1**	**1.1336−1**
2	1.6268−3	1.3371−2	4.6693−2	**8.7441−2**	8.7958−2	3.5630−2
3	3.7032−3	2.4739−2	6.5508−2	8.1288−2	3.7238−2	5.2831−6
4	6.8150−3	3.6873−2	**7.2326−2**	5.3304−2	4.0037−3	1.9620−2
5	1.0785−2	4.7068−2	6.6223−2	2.3231−2	2.8569−3	**4.2661−2**
6	1.5248−2	**5.3428−2**	5.1505−2	4.6199−3	**1.8481−2**	4.1175−2

TABLE 8. *Franck-Condon factors to high vibrational quantum numbers for the O_2 Atmospheric ($b^1\Sigma_g^+ - X^3\Sigma_g^-$) band system*

v' \ v''	0	1	2	3	4	5	6
0	**9.3000-1**	6.7294-2	2.6512-3	6.4085-5	9.3835-7	1.0341-8	3.7300-11
1	6.7276-2	**7.8980-1**	1.3396-1	8.6731-3	3.0158-4	5.9637-6	8.2523-8
2	2.6569-3	1.3360-1	**6.4718-1**	1.9695-1	1.8736-2	8.8087-4	2.2592-5
3	6.8742-5	8.9509-3	1.9530-1	**5.0723-1**	2.5298-1	3.3379-2	2.0431-3

TABLE 9. *Franck-Condon factors to high vibrational quantum numbers for the O_2 I–R Atmospheric ($a^1\Delta_g - X^3\Sigma_g^-$) band system*

v' \ v''	0	1	2	3	4	5	6
0	**9.8692-1**	1.2948-2	1.3605-4	2.4677-7	9.9011-10	1.5322-13	4.7034-13
1	1.3020-2	**9.5876-1**	2.7782-2	4.5133-4	1.2592-6	5.6454-9	1.1942-12
2	6.0566-5	2.8065-2	**9.2637-1**	4.4518-2	9.9828-4	3.9704-6	1.9449-8
3	6.0739-8	2.3808-4	4.5114-2	**8.8969-1**	6.3136-2	1.8396-3	9.9212-6
4	4.5740-8	3.5056-8	6.0928-4	6.4087-2	**8.4869-1**	8.3571-2	3.0493-3
5	2.2138-9	2.1350-7	6.0165-8	1.2732-3	8.4834-2	**8.0346-1**	1.0571-1

TABLE 10. *Franck-Condon factors to high vibrational quantum numbers for the Noxon ($b^1\Sigma_g^+ - a^1\Delta_g$) band system*

v' \ v''	0	1	2	3	4	5
0	**9.7645-1**	2.3320-2	2.3477-4	1.2155-6	7.7672-11	9.1536-11
1	2.3178-2	**9.2694-1**	4.9091-2	7.9620-4	5.7591-6	1.3075-9
2	3.6962-4	4.8450-2	**8.7223-1**	7.7152-2	1.7953-3	1.7072-5
3	5.0908-6	1.2698-3	7.5485-2	**8.1260-1**	1.0726-1	3.3637-3

Many of the band systems are important contributors to the spectrum of the airglow [Chamberlain, 1961]. Some $q_{v'v''}$-values on primary Condon loci were therefore included in a compilation [Nicholls, 1964a] of transition probability data of aeronomical importance presented at the symposium on Laboratory Studies on Aeronomy held by the International Association for Geomagnetism and Aeronomy, Berkeley, August 1963. Similar treatment was given to some of the data of the previous paper of this series [Nicholls, 1964b] which deals with NO band systems.

The sum rule

$$\sum_{v' \text{ or } v''} q_{v'v''} + \int_{\text{Continuum}} dq_{v'v''} = 1 \qquad (3)$$

appears to be satisfied by the contributions from the discrete bands for the Atmospheric, Infrared Atmospheric, and Noxon systems. However, in the case of the Herzberg I, II, III, Chamberlain and Broida-Gaydon systems, the contribution from the discrete bands is small, and a significant contribution can be expected from the photo-dissociation continuum, for, as was pointed out in section 1, dissociation is the most probable result of an upward transition in these cases according to the Franck-Condon principle. Studies have recently been made on the contribution of the Franck-Condon "density" in the continuum for the Schumann-Runge system [Jarmain and Nicholls, 1964] where it was found, for example, that 99.7 percent of the sum from $v'=0$ is in fact vested in the continuum. Realistic Klien-Dunham potentials were used and the work is currently being extended to the Herzberg I system.

One common criticism of Morse Franck-Condon factors is that they may be unrealistic for band systems for which the Morse potentials are not appropriate. The $B^3\Sigma_u^-$ upper state of the Schumann-Runge system is an example of such a case [Jarmain, 1963a, b; Nicholls and Jarmain, 1964]. For the band systems treated in this paper, however, the relatively low values of v_{max} involved in many cases, the general agreement between the position of the Condon loci and the occurrence of known bands, and the fact that no molecular constants beyond $\omega_e x_e$ are available in many cases suggest that the data in tables 3 through 10 are probably not too unrealistic.

Another more general point should be made about the realism of Franck-Condon factors and the potentials to which they are appropriate. This concerns the specific use to which $q_{v'v''}$ are put. In many applications they are used as parameters in the smoothing procedure [Fraser, 1954] briefly described below which ensures the cooperative use of *all* of the measured band intensities in the determination of absolute or relative arrays of the transition probability parameters $S_{v'v''}$, $k_{v'v''}$, $f_{v'v''}$, $A_{v'v''}$, $B_{v'v''}$. Such a procedure is superior to calculations of these quantities band by band because of the great difference of relative error from strong bands to weak bands. The smoothing procedure produces a common error range for the whole system. Equations (1) and (2e) lead to the well-known result:

$$I_{v'v''} = K N_{v'} \nu^4 R_e^2(\bar{r}_{v'v''}) q_{v'v''} \qquad (4)$$

where K is a constant of units and geometry and $N_{v'}$

is the population of the level v'. A plot of $(I_{v'v''}/q_{v'v''}\nu^4)^{1/2}$ versus $\bar{r}_{v'v''}$ (or $\nu_{v'v''}$ or $\lambda_{v'v''}$ to which it is monotonically related [Nicholls and Jarmain, 1956; Nicholls, 1965a] for as many v'' progressions ($v'=$ const.) as the measurements of $I_{v'v''}$ allow, delineates the relative variation of $R_e(r)$ with r for each $v'=$ const. segment. The segments are displaced relative to each other in ordinate because of the $N_v^{1/2}$ factor. Objective rescaling procedures [Turner and Nicholls, 1954, Hérbert and Nicholls, 1961] allow all of the segments to be placed on the same scale and provides the picture of the variation of $R_e(r)$ with r for the whole band system. A least mean squares fit to the resulting points using a simple empirical algebraic form is normally made. The object of this whole procedure is usually less to study $R_e(r)$ for its own sake than to produce a smoothed array of $S_{v'v''}$ (or one of the related transition probability parameters) by the use of equation (1) in which $R_e(\bar{r}_{v'v''})$ is now read band by band from the plot (or calculated from the empirical algebraic form), and the $q_{v'v''}$—values are those used in producing the plot.

The important quantities in all of this procedure are the end products, the smoothed arrays of $S_{v'v''}$[2] (or of $A_{v'v''}$, $B_{v'v''}$, $f_{v'v''}$, $k_{v'v''}$). They are almost independent (except in the magnitude of relative errors) of the model of potential appropriate to which the $q_{v'v''}$ and $\bar{r}_{v'v''}$ have been calculated because of the *two* compensating ways in which $q_{v'v''}$ has been used in the procedure, (a) once to make the original $(I_{v'v''}/q_{v'v''}\ 4_{v'v''})^{1/2}$ versus $\bar{r}_{v'v''}$ plots, and (b) once in the final application of eq (1) to the rescaled plot. $q_{v'v''}$ has been part of a smoothing process. In this type of application where $q_{v'v''}$ is used, compensatingly, twice, the strict realism of the potential to which it is appropriate is thus not as significant as is often claimed. However, in applications where $q_{v'v''}$, or a similiar function of vibrational wavefunctions, is used only once, the realism of the potential model becomes very important. Such cases are: (a) The study of $R_e(r)$ per se, (b) the need for a realistic $q_{v'v''}$ array as an approximation to an $S_{v'v''}$ array when no measured $I_{v'v''}$ are available, (c) the study of Condon loci and the position of strong bands [Murty, 1964], (d) the study of derived quantities of vibrational wave functions.

Over 85 arrays of Franck-Condon factors have been calculated using the programme referred to in section 2 for many radiative, excitation and ionization transitions, and about half of them have so far been published. It has been possible to use these arrays to provide the basis for interpolation of $q_{v'v''}$ for transitions which have not yet been treated [Nicholls, 1964c, 1965b). This is of particular practical importance where the need for $q_{v'v''}$—values is for order of magnitude estimates such as are required in identification problems. A theoretically justified transition parameter $t=\beta\Delta r_e$ which has a specific value for a band sysem is used as interpolation parameter in plots of $q_{v'v''}$ versus t. t varies between 0.02 and 4.7 for the transitions used to make the interpolation plots, and β is the harmonic mean of the coefficients of $(r-r_e)$ of the two Morse potentials.

[2] Relative arrays of $S_{v'v''}$ (and related quantities) are often placed on an absolute basis by comparison with an absolute measurement of one of them or its equivalent [Nicholls, 1964a].

The great assistance to this work of Miss R. Zucker of the NBS Computational Laboratory is gratefully acknowledged.

The work has been largely supported through research grants from the National Aeronautics and Space Administration (NsG–349) and The Air Force Office of Scientific Research (AF–AFOSR 62–236).

Some support from Contracts with the Air Force Cambridge Research Center (AF 19(628)—2820) and the Defence Research Board of Canada and grants from the National Research Council of Canada is also gratefully acknowledged.

5. References

H. D. Babcock and L. Herzberg (1948), Astrophys. J. **108,** 167.
C. A. Barth and M. Patapoff (1962), Astrophys. J. **136,** 1144.
H. P. Broida and A. G. Gaydon (1954), Proc. Roy. Soc. A **222,** 181.
H. P. Broida and M. Peyron (1960), J. Chem. Phys. **32,** 1068.
J. W. Chamberlain (1958), Astrophys. J. **128,** 713.
J. W. Chamberlain (1961), Physics of the Aurora and Airglow (Academic Press, New York).
R. W. Ditchburn and D. W. O. Heddle (1954), Proc. Roy. Soc. **226,** 509.
R. W. Ditchburn and P. A. Young (1962), J. Atmospheric Terrest. Phys. **24,** 127.
M. W. Feast (1949), Proc. Phys. Soc. **A62,** 114.
P. A. Fraser (1954), Can. J. Phys. **32,** 515, 1954.
G. R. Hébert and R. W. Nicholls (1961) Proc. Phys. Soc. **78,** 1024.
G. Herzberg (1950), Spectra of Diatomic Molecules (D. Van Nostrand, New York).
G. Herzberg (1952), Can. J. Phys. **30,** 185.
G. Herzberg (1953), Can. J. Phys. **31,** 657.
L. Herzberg and G. Herzberg (1947), Astrophys. J. **105,** 353.
W. R. Jarmain (1963a) Can. J. Phys. **41,** 414.
W. R. Jarmain (1963b), Can. J. Phys. **41,** 1926.
W. R. Jarmain and R. W. Nicholls (1964), Proc. Phys. Soc. **84,** 417.
Mary Murty (1964), M. Sc. Thesis, University of Western Ontario.
R. W. Nicholls (1960), Can. J. Phys. **38,** 1705.
R. W. Nicholls (1961), J. Res. NBS **65A,** (Phys. and Chem.) No. 5, 451.
R. W. Nicholls (1963), Nature **199,** 794, 1963.
R. W. Nicholls (1964a), Ann de Géophys **20,** 144.
R. W. Nicholls (1964b), J. Res. NBS **68A** (Phys. and Chem.) No. 5, 535.
R. W. Nicholls (1964c), Nature **204,** 373.
R. W. Nicholls (1965a), Proc. Phys. Soc. **85,** 159.
R. W. Nicholls (1965b), J. Quant. Spectrog. & Radiative Transfer (in press).
R. W. Nicholls and W. R. Jarmain (1956), Proc. Phys. Soc. **A69,** 713.
J. F. Noxon (1961), Can. J. Phys. **39,** 1110.
R. W. B. Pearse and A. G. Gaydon, The Identification of Molecular Spectra, 3d ed. (Chapman & Hall, London).
R. G. Turner and R. W. Nicholls (1954), Can. J. Phys. **32,** 475.
L. V. Wallace (1962), Astrophys. J. Supp. (No 68) **7,** 165.

(Paper 69A4–357)

JOURNAL OF RESEARCH of the National Bureau of Standards—A. Physics and Chemistry
Vol. 69A, No. 4, July–August 1965

An Absolute Temperature Scale From 4 °K to 20 °K Determined From Measurements With an Acoustical Thermometer*

H. H. Plumb and G. Cataland

(March 25, 1965)

At NBS an acoustical thermometer has been used to obtain values of temperature at every degree from 5 to 20 °K as a basis for a temperature scale. This scale has been compared with four other temperature scales in the region from 10 to 20 °K. Since the acoustical thermometer is an entirely new approach to precision thermometry in this range the comparison of its resulting scale with scales based upon gas thermometry from 12 to 20 °K is significant. Indications of inaccuracies in the equilibrium hydrogen vapor pressure scales, and also in the He^4 vapor pressure scale, are presented.

For a number of years the National Bureau of Standards has been engaged in a low temperature thermometry program, one objective of which is the establishment of a primary temperature scale which would include the region 4 to 14 °K. After consideration of the relative merits and disadvantages of conventional gas thermometry, it was decided that an investigation of temperature measurements derived from the speed of sound in helium gas should be initiated. In addition to the application in the range 4 to 14, the acoustical thermometer should also provide an independent check above 14 °K and below 4 °K. The "acoustical interferometer" appeared to be the best instrument for the experimentation.

A general discussion of the acoustical interferometer has been presented by J. L. and E. S. Stewart [1];[1] more specific application to low temperatures has been reported by Van Itterbeek and his coworkers [2–4]. While it is not the intention of the present paper [2] to discuss the acoustical interferometer as an operating instrument, it is necessary to mention that it involves a constant frequency and a variable path as opposed to a resonating column in which the path length is fixed and the frequency variable.[3]

When an experimental determination of the speed of sound in helium gas as a function of pressure at a constant temperature has been made, the data can be treated to yield values of absolute temperature by means of eq (1).

$$W^2=(C_p/C_v)_{p=0}R_MT/M_{He}(1+\alpha p+\beta p^2+\ldots) \quad (1)$$

where W is the speed of sound in helium gas; $(C_p/C_v)_{p=0}=5/3$; $R_M=8.314\times10^7$ (erg/°K mole); $M_{He}=4.0026$; p is the pressure; $\alpha=1/(RT)[2B+4/3(T)(dB/dT)+4/15(T^2)(d^2B/dT^2)]$; B is the second virial coefficient; and T, the absolute temperature.

In practice, values of the speed, W, are experimentally determined at pressures sufficiently low that the plot of W versus p is linear and can be extrapolated to zero pressure; the intercept is then the value of the speed of sound for an ideal gas, and eq (1) reduces to

$$W_0^2=(C_p/C_v)_{p=0}R_MT/M_{He}$$

where W_0 is the speed intercept at $p=0$. It is to be noted that the acoustical temperature determination eliminates troublesome corrections that are involved in gas thermometry, i.e., dead space corrections, gas adsorption and precise volume changes and pressure determinations.

One of the most critical parts of the thermometer is the portion of the apparatus which contains the sonically excited helium gas. This is at the temperature to be maintained constant and determined. To aid in accomplishing this, several secondary thermometers of high sensitivity (germanium resistors) were in intimate thermal contact with the region. One resistor served as a sensor for an automatic heater controlling unit while two other resistors indicated how well a constant temperature was being maintained and also served as secondary thermometers which were calibrated by the acoustical thermometer. All of this portion of the apparatus was suitably thermally insulated from the surrounding liquid helium or liquid hydrogen bath so that it could be isothermally floated in the temperature region of interest. While this portion of the acoustical thermometer was maintained constant in temperature the speed of sound in the helium 4 gas was measured as a function of pressure. (This is referred to as an isotherm in our work.)

During the hours that are spent on any given isotherm, germanium resistance values are systematically measured. In general five to seven

*This paper was presented at the 1964 meeting of the Thermometry Advisory Committee of the International Committee of Weights and Measures.

[1] Figures in brackets indicate the literature references at the end of this paper.

[2] The NBS acoustical interferometer has been cursorily described in the literature [5, 6] the details will appear later.

[3] Measurement of the sound speed in helium gas yielding absolute temperature determinations have also been conducted with the resonating tube. Some results have been reported by De Laet [7] and by Brodsky, Kremlevsky, and Savateev [8].

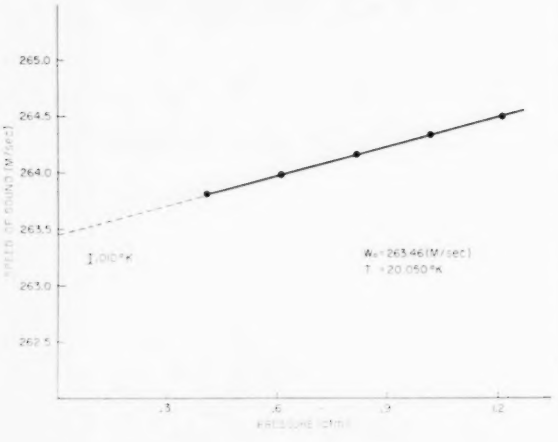

FIGURE 1. *20.050 °K Isotherm.*
The dashed line is the extrapolation of the isotherm to zero pressure.

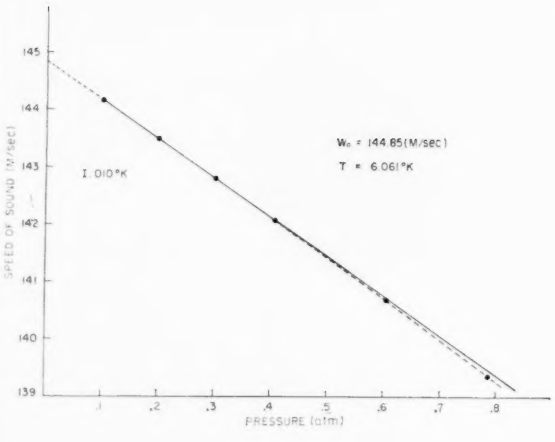

FIGURE 2. *6.061 °K Isotherm.*
At the lowest pressures the dashed line depicts the extrapolation to zero pressure. At the highest pressure, the dashed line indicates departure of the isotherm from a linear representation (the solid line).

pressure-speed points were measured to establish each isotherm. Figures 1 and 2, typical of the determined isotherms, indicate how the isotherm is extrapolated to zero pressure; the intercept affords a simple calculation of the isotherm temperature.

For the pressures employed in the temperature range of interest, all of the isotherms are linear within the limits of experimental reproducibility. At sufficiently large pressures, however, departures from linearity are to be expected. For example, in figure 2 the measurements indicate that the isotherm has noticeably departed from linearity at 0.6 atm and above, whereas in figure 1 a linear representation of the isotherm up to 1.2 atm appears satisfactory. We have generally observed that experimental reproducibility of points on an isotherm is ± 0.002 °K. If one conducts measurements at pressures sufficiently low that the isotherm can be represented by a straight line, an important check on the consistency of the isotherms is afforded by the smoothness of the plot of isotherm slopes as a function of the determined temperatures. The slopes naturally are related to the virial coefficients and will permit their determination.

Isotherms have been determined every degree from 5 to 20 °K and accordingly at each temperature several germanium resistors were calibrated. Because it was desirable to compare the acoustical thermometer scale with other existing scales in regions of overlap, several germanium resistors were calibrated by Riddle's group against the NBS (1955) provisional scale which is based on earlier gas thermometry [4] and preserved by a group of platinum resistors.

Every germanium resistor which was used has a history of at least one year in our laboratory and some have demonstrated a reproducible 4.2 °K calibration (against the He^4 vapor pressure scale, T_{58}) within 0.001 °K even when subjected to 100 thermal cyclings between room temperature and 4.2 °K. Of the two resistors which were calibrated against the NBS (1955) provisional scale, one was calibrated in May 1963 and the other in June 1964. Both resistors were compared to the acoustical thermometer scale in June 1964 by being mounted in the acoustical thermometer and brought to the acoustically determined temperatures at which the instrument germanium resistors had been calibrated. This has afforded a comparison of acoustically determined temperatures with those associated with the NBS (1955) provisional scale between 10 and 20 °K. And, since the NBS (1955) provisional scale has recently been compared with other scales, the acoustically determined temperatures can be related to these also. This has been done in figure 3.

Most of figure 3 has originated from the National Physical Laboratory and has been confirmed by PRMI.[5] It is to be noted that there is an excellent agreement between the acoustically determined temperature and both the NPL and NBS scale from 12 to 20 °K. Indeed, even the departure of the NPL scale from the NBS scale in the vicinity of 14 °K appears to be strongly supported. Unfortunately

[4] The NBS (1955) provisional scale was obtained by subtracting 0.010 °K from the NBS (1939) scale [9].

[5] The general plot was included in a paper submitted by C. R. Barber to the Thermometry Advisory Committee of the International Committee of Weights and Measures (Sept. 1964). At the same meeting a paper submitted by M. P. Orlova, D. I. Sharevskaja, and D. N. Astrov confirmed in detail the results of C. R. Barber.

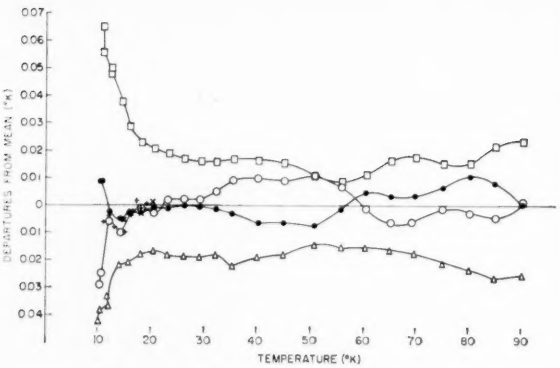

FIGURE 3. *Values of temperature determined with the acoustical thermometer are compared with temperature scales from Pennsylvania State University, Physical-technical Radio-technical Measurements Institute, The National Physical Laboratory, and the NBS (1955) provisional scale.*

△, PSU; □, PRMI; ●, NBS; ○, NPL; ×, +, acoustical thermometer.

it has not been convenient to compare our temperatures with the NBS scale at 10 °K. We are not in a position at present to state the accuracy of our temperature determinations but we have stated the experimental reproducibility of our isotherm measurements previously in this paper.

Our experience thus far, although it is limited, cautions us to doubt the accuracy of published hydrogen vapor-pressure scales. Our preliminary measurements indicate that the "accepted" equilibrium hydrogen boiling point may be 20 mdeg lower than its thermodynamic temperature; this possible inaccuracy may also exist throughout the hydrogen vapor pressure scale to some extent. Quite consonant with this conclusion is the possibility of error in the T_{58} He^4 vapor scale also. Preliminary measurements again indicate that the He^4 boiling point may be 0.006 °K too low; and that He^4 vapor pressure scale temperatures near 2 °K may be 0.003 °K low also.

It is expected that the values of acoustically determined temperatures described in this paper will result in a provisional scale which will be used by the National Bureau of Standards principally for calibrations of germanium resistance thermometers from 5 to 20 °K.

References

[1] J. L. Stewart and E. S. Stewart, J. Acoust. Soc. Am. **24,** 22–26 (1952).
[2] A. Van Itterbeek, Progress in Low Temperature Physics (Interscience Publishers, Inc., New York; Norths Holland Publishing Company, Amsterdam, 1955), **I,** p. 355.
[3] A. Van Itterbeek and G. Forrez, Physica **20,** 133 (1954).
[4] A. Van Itterbeek, J. Acoust. Soc. Am. **29,** 584–587 (1957).
[5] Temperature, Its Measurement and Control in Science and Industry, Proceedings of Fourth Symposium on Temperature, Columbus, Ohio, 1961 (Reinhold Publishing Corporation, New York, 1962), **III,** pt. 1, 129–132.
[6] G. Cataland and H. H. Plumb, J. Acoust. Soc. Am. **34,** 1145–1146 (1962).
[7] J. De Laet, Verhandel. Koninkl. Vlaam. Acad. Wetenschap, Belg. Kl Vetenschap nr. **66,** 3 (1960).
[8] A. D. Brodsky, V. P. Kremlevsky, and A. V. Savateev, Comite International des Poids et Mesures, Comite Consultatif de thermometrie 6e Session—1962, Annexe 27.
[9] H. J. Hoge and F. G. Brickwedde, J. Res. NBS **22,** 351–373 (1939) RP1188.

(Paper 69A4–358)

JOURNAL OF RESEARCH of the National Bureau of Standards—A. Physics and Chemistry
Vol. 69A, No. 4, July–August 1965

Publications of the National Bureau of Standards*

Selected Abstracts

International comparison of atomic frequency standards via VLF radio signals, A. H. Morgan, E. L. Crow, and B. E. Blair, *Radio Sci. J. Res. NBS/USNC-URSI, Vol.* **69D,** *No. 7, 905–914 (July 1965).*

A study was made of data obtained over an 18-month period (July 1961 to December 1962, inclusive) on the comparison of atomic frequency standards located in seven laboratories in the United States, Europe, and Canada, using the VLF signals of GBR (16 kc/s), Rugby, England and NBA (18 kc/s), Balboa, Canal Zone. Each laboratory observes the accumulated difference in phase over a 24-hr period (the same for all laboratories, or nearly so) between its own standard (either laboratory or commercially constructed) and the received VLF signal. A statistical analysis was designed to separate the observations at each laboratory into three components: (a) long-term mean differences among the atomic standards; (b) estimates of the standard deviations, $\hat{\alpha}_i$, at each receiving station; and (c) estimates of the transmitter standard deviations, $\hat{\tau}$. Each $\hat{\alpha}_i$ includes receiver fluctuations, propagation effects peculiar to the path, and measurement uncertainties; $\hat{\tau}$ includes the transmitter fluctuations and propagation effects common to all paths.

The study shows that $\hat{\alpha}_i$ at each receiver varied from a low of 0.39×10^{-10} units of fractional frequency (that is, 0.39 parts in 10^{-10} (GBR data) at LSRH to a high of 1.97×10^{-10} (GBR data) at NRC with an average for all stations of 1.01×10^{-10} measured against GBR and 0.99×10^{-10} when measured against NBA. Also, the average $\hat{\tau}$ for GBR is 1.26×10^{-10} and for NBA is 0.68×10^{-10}. Finally, it is shown that: (1) The means of the frequencies of the seven individual atomic standards laboratories agreed with the grand mean of these seven standards to within ±2 parts in 10^{10} for the 18-month period, and (2) The laboratory-type standards agreed with their grand mean to within ±1 part in 10^{10}.

Control of WWV and WWVH standard frequency broadcasts by VLF and LF signals, B. E. Blair and A. H. Morgan, *Radio Sci. J. Res. NBS/USNC-URSI, Vol.* **69D,** *No. 7, 915–920 (July 1965).*

Since 1961 the NBS VLF and LF signals have improved the calibration and frequency control of the WWV (Maryland) HF broadcasts. Similarly, better control of the WWVH (Hawaii) HF broadcasts was achieved in early 1963 by monitoring the NBS VLF broadcasts in terms of the WWVH control oscillator. In mid 1963 WWVL (20 kc/s) and WWVB (60 kc/s) were relocated from two sites near Boulder, Colo., to a single site near Fort Collins, Colo., and the transmitter power for both broadcasts was increased several fold. These higher powered broadcasts resulted in more precise control of both HF broadcasts. Through the VLF and LF signals the 24-hr average frequency values of WWV are related to the United States Frequency Standard (USFS) within a few parts in 10^{11}.

This paper describes the NBS low-frequency broadcasts, the method of using them to control and calibrate the HF broadcasts, and gives an analysis of the precision of frequency control obtained at WWV over a 21-month period. An appendix discusses the short-term phase stabilities and diurnal phase shifts observed in the low-frequency signals at WWV and WWVH, and examines the accuracy-limiting effects of propagation path characteristics and background noise levels in such received signals.

Measurements of the total electron content and the equivalent slab thickness of the midaltitude ionosphere, R. V. Bhonsle, A. V. da Rosa, and O. K. Garriott, *Radio Sci. J. Res. NBS/USNC-URSI, Vol.* **69D,** *No. 7, 929–937 (July 1965).*

The total electron content N_T and the equivalent slab thickness τ of the midlatitude ionosphere are determined from differential Doppler measurements on the radio transmissions from the Transit 4A satellite and the ionosonde data near Washington, D.C., and Ottawa. The trends of diurnal, seasonal, and sunspot cycle variations of N_T and τ at midday are described. It is found that in 1962 both N_T and τ were considerably decreased in magnitude as compared to the corresponding values near the peak of the sunspot cycle. The inferred mean electron-ion temperature is found to be generally in excess of the neutral gas temperature. The ratio T_e/T_g in the daytime is estimated to be 1.8 in summer and about 1.1 to 1.2 in winter, which may reflect corresponding changes in the ratio Q/N_e^2, where Q is the heat input to the electrons and N_e is the electron density. The relationship between τ and K_p appears to be rather ambiguous in contrast with the positive correlation between the neutral gas temperature and K_p.

Calibration of liquid-in-glass thermometers, J. F. Swindells, *NBS Mono. 90 (Feb. 12, 1965), 25 cents. Supersedes NBS Cir. 600.*

This Monograph, which supersedes Circular 600, contains information of general interest to both manufacturers and users of liquid-in-glass thermometers, as well as those who wish to calibrate thermometers or submit them to the National Bureau of Standards for calibration. Instructions are provided for applicants requesting calibration services, and the techniques and equipment used in the calibration procedures are described. Important elements of thermometer design are discussed, and factors affecting the use of common types of liquid-in-glass thermometers are included together with tables of tolerances and reasonably attainable accuracies. The calculation of corrections for the temperature of the emergent stem is given in detail for various types of thermometers and conditions of use.

Standard cells. Their construction, maintenance, and characteristics, W. J. Hamer, *NBS Mono. 84 (Jan. 15, 1965), 35 cents.*

This Monograph contains information on the construction, maintenance, and characteristics of standard cells. The effects of temperature, pressure, electric current, light, shock, and vibration on standard cells are discussed. A history of the realization and maintenance of the unit of electromotive force is also included. A record of international comparisons of the unit of electromotive force is presented as well as information in the constancy of the National Reference Group of Standard Cells.

Standard Reference Materials: Sources of information, J. L. Hague, T. W. Mears, and R. E. Michaelis, *NBS Misc. Publ. 260–4 (Feb. 1965), 20 cents.*

This annotated listing of sources of Standard Reference Materials is prepared with references to all types of materials used to standardize analytical, physico-chemical and engineering methods. The range of Standard Reference Materials included runs from high-purity substances and carefully analyzed metals, alloys and rocks to materials of indefinitely-known composition for standardizing a single phenomenon.

Report of the 49th National Conference on Weights and Measures 1964, *NBS Misc. Publ. 263, (Feb. 1, 1965), $1.00.*

A report of the proceedings of the fourth-ninth National Conference on Weights and Measures, held in Washington, D.C., June 15–19, 1965, and attended by State, county, and city weights and measures officials.

The Joule-Thomson process in cryogenic refrigeration systems, J. W. Dean and D. C. Mann, *NBS Tech Note 227 (Feb. 14, 1965), 30 cents.*

A comprehensive analysis of the Joule-Thomson process as applied to cryogenic refrigeration systems is presented. The descriptions of the process already in the literature are usually for specific applications. In contrast, performance characteristics are presented here for helium, para-hydrogen, and nitrogen operations over a large range of process parameters.

Nonlinear ambipolar diffusion of an isothermal plasma across a magnetic field, E. R. Mosburg and K. B. Persson, *Phys. Fluids* **7,** *1829–1833 (Nov. 1964).*
Solutions are presented of the first two moment equations, including non-linear terms, for the ambipolar diffusion of an isothermal plasma across a magnetic field. The two geometries considered are the plane parallel case and the infinite cylinder with axial symmetry. The Bohm criterion is automatically satisfied by the solutions. It is shown that the singularity in the space derivative of the ambipolar drift velocity at the plasma boundary cannot be removed by an axial magnetic field of any strength. Thus the plasma drift velocity and the plasma density remain monotonic functions of the position coordinate. It is also shown, under the assumptions of this theory, that the ambipolar space charge field is always directed outward and does not reverse direction in this isothermal approximation even for extremely high magnetic fields. One is forced to conclude that a realistic theory of ambipolar diffusion requires the consideration of the thermal gradients within the plasma.

Interacting of maxima in the absorption of soft x-ray, J. W. Cooper, *Phys. Rev. Letters* **13,** *No. 25, 762–764 (Dec. 21, 1964).*
The interpretation of recently observed maxima in photoelectric cross sections in the soft x-ray region is given in terms of a one-electron central field model. The observations, which represent a departure from the usual behavior of x-ray absorption cross sections, is shown to be consistent with the one-electron central field description.

Natural variations in the abundance ratio and the atomic weight of copper, W. R. Shields, S. S. Goldich, E. L. Garner, and T. J. Murphy, *J. Geophys. Res.* **70,** *No. 2, 479–491 (Jan. 15, 1965).*
The absolute ratio Cu^{63}/Cu^{65} was determined for 106 samples that include a variety of copper minerals. Relative to a reference copper sample with previously determined absolute ratio of 2.2440 ± 0.0021, variations range from -9.0 to $+3.3$ per mil. No significant variations were found for chalcopyrite, tetrahedrite, enargite, or in the Canyon Diablo and Bruderheim meteorites. Some samples of bornite and of chalcocite exhibit variations with enrichments in either Cu^{63} or in CU^{65}. Secondary oxides of copper show significant enrichment only in the heavy isotope. The relative variations previously reported by Walker, Cuttitta, and Senftle for samples from the Cougar mine, Colorado, are confirmed. A mean value of 2.2431 for 82 mineral samples probably is unduly weighted with the rarer secondary minerals that are enriched in CU^{65}. The ratio Cu^{63}/Cu^{65} for bulk or commercially processed copper is very near to the value of 2.2440, and the atomic weight of such copper is 63.5455 ± 0.0010. The causes of the natural variations in copper abundance ratios are not known.

Optical heterodyne detection of the forward stimulated Brillouin scattering, D. A. Jennings and H. Takuman, *Appl. Phys. Letters* **5,** *241–242 (Dec. 1964).*
The small frequency shift associated with the small angle forward Brillouin scattering in carbon disulfide when excited by the *Q*-switched ruby laser has been measured by using an optical heterodyne technique. The frequency shift was measured to be 123 Mc/sec for an off-axis angle of 0.0433 rad. The velocity of sound at 123 Mc/sec in carbon disulfide was calculated to be 1223 ± 24 m/sec from these measurements.

The calibration of the National Bureau of Standards' tritiated-toluene standard of radioactivity, S. B. Garfinkel, W. B. Mann, R. W. Medlock, and O. Yura, *Intern. J. Appl. Radiation Isotopes* **16,** *27–33 (1965).*
The difficulties encountered, and their solution, when calibrating a radioactivity standard of tritiated toluene by comparison with the NBS tritiated water standard by means of liquid scintillation counting, are described. Leaks in the seals of commercial vials, giving rise to uncontrolled oxygen quenching, were eliminated by modifying the seals. White plastic caps gave higher count rates than black plastic caps. A new and highly precise method of dilution was used. The ratio of the activities of the two standards was determined with a standard error of less than 0.1 percent.

Conductance of glass immersed in molten salts, K. H. Stern, *J. Electrochem. Soc.* **112,** *No. 2, 208–210 (Feb. 1965)*
The electrical conductivity of high SiO_2 glass was measured when immersed in a number of molten salts and salt mixtures between 800 and 900° C. Sodium and lithium ions diffuse into the glass, both from their own chlorides and from low concentrations in KCl. The glass comes to equilibrium with each melt composition, the time of equilibration depending on the particular ions in the melt. The activation energy of sodium and lithium ion conduction in glass is 75–84kj (18–20 kcal), with potassium it is variable between 105 (25 kcal) and 167 (40 kcal). The conductance method is not sufficiently precise to detect silver and cuprous ion diffusion into glass.

Magnetic properties of ilmenite-hematite solid solutions, C. F. Jefferson and R. G. West, *J. Am. Ceram. Soc.* **47,** *No. 11 544–548 (Nov. 1964).*
The magnetic and dielectric properties of some ilmenite-hematite solid solutions are reported. These properties are found to resemble those of the ferrites. Compositions were prepared that possess high electrical resistivities and low dielectric losses. The introduction of manganese into the system $(1-x)\ Ni_{1-y}\ Mn_y\ TiO_3 + x Fe_2O_3$ increases the room temperature magnetic moments and decreases the resistivities.

Properties of normal and para hydrogen, R. B. Stewart and H. M. Roger, *Book Technology and Uses of Liquid Hydrogen, ed. R. B. Scott, W. H. Denton, and C. M. Nichols, ch. 11, 379–404 (Pergamon Press Inc., New York, N.Y., 1964).*
The P-V-T, thermodynamic and transport properties of normal and para hydrogen for low temperatures are summarized in tables and graphs from selected references.

Thermodynamics of hydrogen solubility in cryogenic solvents at high pressures, M. Orentlicher and J. M. Prausnitz *Book, Chem. Eng. Sci.* **19,** *775–782 (1964).*
Solubility data for hydrogen in liquids at low temperature and high pressure have been reduced by a thermodynamic relation similar to the Krichevsky-Kasarnovsky equation but allowing for the variation of activity coefficient with hydrogen concentration. The parameters appearing in this relation have been partially correlated on the basis of a very simple solution model. The results show that under comparable conditions the solubility of hydrogen in simple inorganic solvents (argon, nitrogen, carbon monoxide) is considerably larger than that in light hydrocarbons (ethane, ethylene, propane, propylene) with methane falling in between these groups. Some possible explanations are suggested.

Surface integral form for three-body collision in the Boltzmann equation, M. S. Green, *Phys. Rev.* **136,** *No. 4A, A905–A910 (Nov. 16, 1964).*
A new form is given for the triple collision term in the generalized Boltzmann equation which is more similar to the well-known binary collision expression than those given heretofore. The form involved is a surface integral over a five-collision parameter space which is the generalization of the two-dimensional collision parameter space for binary collisions. For "soft" repulsive interactions, the expression involves both the asymptotic properties of three-body collisions before and after the collision and the dynamics of binary collisions during the collision process. For hard spheres, the expression involves only the asymptotic properties of ternary and binary collisions.

Food for tomorrow's billions, A. T. McPherson, *Proc. forum "Food in the Future: Concepts for Planning," Chicago, Ill., Oct. 8–9, 1964, pp. 51–73 (Dairy and Food Industries Supply Assoc., 1964).*

The problem of population and food is as old as the human race. The discovery of agriculture about 9,000 years ago made possible an enormous increase in the food supply and a corresponding increase in population. The world population has been increasing at an accelerating rate since 1650. Today over half of the people have a diet insufficient in quantity and inadequate in quality and the explosive increase in population is accentuating the shortage.

Direct synthesis of food is proposed as a means of quickly supplementing agricultural production of protein and fat which are especially needed in Asia and the Far East. The feasibility of synthesis is demonstrated by the successful production of nearly all non-food agricultural products, and the current manufacture of vitamins and amino acids for use both in animal feeding and for human consumption. The use of petroleum as a raw material for synthesis would require only a fraction of the quantity now used as fuel. The present world situation calls for a major new source of food at the earliest possible time. The early development of large scale synthesis affords a feasible means of meeting this need.

Stress-induced Martensitic transformations in 18Cr-8Ni steel, R. P. Reed and C. J. Gutner, *Trans. Met. Soc. AIME* **230,** *1713–1720 (Dec. 1964).*

A commercial 18Cr-8Ni iron alloy (AISI 304L) was examined in tension at 300, 76, 20, and 4° K. Continuous stress-strain recordings were made, x-ray anaylses at periodic stress (strain) intervals were obtained, and magnetic measurements were taken. From this data the percentage of martensitic products (BCC(α) and HCP(ϵ)) were computed as a function of stress (strain).

It was found that up to 15% ϵ phase forms at low temperatures. The amount of ϵ formed increases to about 5% strain, then decreases. This decrease indicates the additional transformation of ϵ to α'. The total amount of ϵ and α' was suppressed at constant stress (strain) at 4° K as compared to 76° K. It is proposed that the suppression of ϵ and α' is associated with the decreased mobility of extended dislocations at very low temperatures. The yield strength decreased as the temperature was depressed below room temperature and then increased rapidly near 4° K.

High resolution, low energy electron spectrometer, J. A. Simpson, *Rev. Sci. Instr.* **35,** *No. 12, 1698–1704 (Dec. 1964).*

An electron spectrograph consisting of an electron source, an electron monochromator, a gas cell, and an electron energy analyzer is described. The electron energy spread from the monochromator as seen by the analyzer is 0.005 eV at 3.35 eV primary energy. It is shown that space charge within the beam requires operation of the energy selectors at the lowest possible energy if high current together with high resolution are required.

Electron-impact studies of aromatic hydrocarbons. III. Azulene and napthalene, R. J. Van Brunt and M. E. Wacks, *J. Chem. Phys.* **41,** *No. 10, 3195–3199 (Nov. 15, 1964).*

The ionization-dissociation processes in azulene and naphthalene were studied. The appearance potentials of the major ions in their mass spectra were determined. The observed ionization energies of naphthalene (8.26 eV) and azulene (7.72 eV) and the heats of formation of these compounds provided an energetic scheme consistent with the measured appearance potentials of the secondary ions and the assumption of ionic intermediates common to both compounds. The occurrence of these common intermediate ions which lead to the observed fragmentation in these compounds was also demonstrated by the similarity of the mass spectra of these two compounds. Additional evidence was provided by observations made of the metastable ion transitions found in their mass spectra.

Electron-impact studies of aromatic hydrocarbons. II. Naphthacene, chrysene, triphenylene, and pyrene, M. E. Wacks, *J. Chem. Phys.* **41,** *No. 6, 1661–1666 (Sept. 15, 1964).*

The systematic survey of ionization-dissociation processes of fused-ring aromatic compounds initiated previously is continued. Mass spectra and appearance potentials of the singly and doubly charged molecule ions are reported. The observed ionization energies of naphthacene (6.95 eV), naphthaphene (7.53 eV), chrysene (8.01 eV), triphenylene (8.19 eV), and pyrene (7.72 eV) are compared with available spectroscopic data, with values obtained from molecular orbital calculations, with the available empirical and semi-empirical methods, and with other electron impact data.

Formation of NF from NF_2 by photolysis, D. E. Mann and and J. J. Comford, *Spectrochim. Acta* **21,** *197–198 (Pergamon Press Ltd., Northern Ireland, 1965).*

The NF radical has been produced along with NF_3 by photolysis of NF_2 isolated in a solid argon matrix at 4 °K. The results indicate that the F atoms formed by the photodecomposition $NF_2 \xrightarrow{h\nu} NF + F$ are able to diffuse easily through the matrix even at 4 °K, whereas the other principal species present, NF and NF_2, are comparatively immobile under these conditions.

Spectral properties of plants, D. M. Gates, H. J. Keegan, J. C. Schleter, and V. R. Weidner, *Appl. Opt.* **4,** *No. 1, 11–20 (Jan. 1965).*

The spectral photometric properties of plant leaves and stems have been obtained for ultraviolet, visible, and infrared frequencies. The spectral reflectance, transmittance, and absorptance for certain plants is given. The mechanism by which light and radiation interact with a leaf is discussed, including the presence of plant pigments. Examples are given concerning the amount of absorbed solar radiation for clear sky and overcast conditions. The spectral properties of desert plants are compared with those of more mesic plants. The evolution of the spectral properties of plant leaves during the early growing season is given as well as the colorimetric behavior during the autumn.

Other NBS Publications

Radio Sci. J. Res. NBS/USNC-URSI, Vol. 69D, No. 6 (June 1965), $1.00.

Cyclotron harmonic waves in warm plasma. F. W. Crawford.

Propagation of waves across a magnetoplasma-vacuum boundary. R. L. Gallawa.

Phase velocities and attenuation distances in the ionosphere. D. R. Croley, Jr., and B. S. Tanenbaum.

Ionospheric effects of electrostatic fields generated in the outer magnetosphere. G. C. Reid.

An experimental study of plasma sheath effects on antennas. G. Tyras, P. C. Bargeliotes, J. M. Hamm, and R. R. Schell.

An approach to improve re-entry communications by suitable orientations of antenna and static magnetic field. S. N. Samaddar.

Concerning the mechanism of reflection of electromagnetic waves from an inhomogeneous lossy plasma. J. R. Wait.

Selection of Papers Presented at 1964 World Conference on Radio Meteorology, Boulder, Colo., September 14–18, 1964

Angles in focus. D. Atlas.

An investigation of clear air stratification with radar and elevated instruments. D. R. Hay and K. Naito.

On inferring the refractive-index structure of the troposphere from electromagnetic scattering experiments. P. L. Smith, Jr.

The biexponential nature of tropospheric gaseous absorption of radio waves. E. J. Dutton and B. R. Bean.

Complete scattering parameters of polydispersed hydrometeor in the λ 0.1 to λ 10 cm range. D. Deirmendjian.

Radio Sci. J. Res. NBS/USNC-USRI, Vol. 69D, No. 7 (July 1965), $1.00.

International comparison of atomic frequency standards via VLF radio signals. A. H. Morgan, E. L. Crow, B. E. Blair. (See above abstracts.)

Control of WWV and WWVH standard frequency broadcasts by VLF and LF signals. B. E. Blair and A. H. Morgan. (See above abstracts.)

Measurements of the total electron content and the equiv-

alent slab thickness of the midlatitude ionosphere. R. V. Bhonsle, A. V. da Rosa, and O. K. Garriott. (See above abstracts.)

D-region absorption at 10 and 15 Mc/s during the total solar eclipse of July 20, 1963. G. M. Lerfald, J. K. Hargreaves, and J. M. Watts.

Effect of the eclipse of 20 July 1963 on VLF signals propagating over short paths. J. H. Crary and D. E. Schneible.

A comparison of radar auroral reflection data with acoustic wave theory. R. L. Leadabrand.

Electromagnetic properties of a plasma covered antenna. D. J. Jacavanco.

Influence of an inhomogeneous ground on the propagation of VLF radio waves in the earth-ionosphere waveguide. J. R. Wait.

Aspects of the terrestrial ELF noise spectrum when near the source or its antipode. L. G. Abraham, Jr.

Analysis of linear arrays focused in the Fresnel region. P. P. Lombardini, R. Doviak, and J. Goldhirsh.

Theory of coil antennas. T. Padhi.

Small prolate spheroidal antenna in a dissipative medium. R. H. Williams, R. D. Kelly, and W. T. Cowan.

Calculated curves for groundwave propagation over inhomogeneous earth with pronounced topographical features. K. Furutsu.

Technical highlights of the National Bureau of Standards, Annual Report 1964, NBS Misc. Publ. 264 (Dec. 1964) $1.00.

Pipe nipples: Brass, copper, steel, and wrought-iron, NBS CS5–56 (Jan. 15, 1965), 10 cents. Supersedes CS5–46.

Ponderosa pine windows, sash, and screens (using single glass and insulating glass), NBS CS163–64 (Mar. 17, 1964) 15 cents. Supersedes CS163–59 and CS 193–53.

Wood double-hung window units, NBS CS190–64 (Mar. 17, 1964), 10 cents. Supersedes CS190–59.

Wood awning window units, NBS CS204–64 (Mar. 17, 1964), 10 cents. Supersedes CS204–59.

Wood casement window units, NBS CS205–64 (Mar. 17, 1964), 10 cents. Supersedes 205–59.

Wood horizontal-sliding window units (All sash operating), NBS CS264–64 (Mar. 17, 1964), 10 cents.

Wood horizontal-sliding window units (One or more non-operating sash), NBS CS265–64 (Mar. 17, 1964), 10 cents.

Wood single-hung window units, NBS CS266–64 (Mar. 17, 1964), 10 cents.

Quarterly radio noise data September, October, November 1963, W. Q. Crichlow, R. T. Disney, and M. A. Jenkins, NBS Tech. Note 18–20 (Oct. 23, 1964), 50 cents.

Quarterly radio noise data December, January, February, 1963–64, W. Q. Crichlow, R. T. Disney, and M. A. Jenkins, NBS Tech. Note 18–21 (Jan. 25, 1965), 50 cents.

A tabulation of airy functions, H. T. Dougherty and M. E. Johnson, NBS Tech. Note 228 (Sept. 18, 1964), 20 cents.

Table of attenuation as a function of vane angle for rotary-vane attenuators ($A = -40 \log_{10} \cos \theta$), W. Larson, NBS Tech. Note 229 (Jan. 7, 1965), $1.25.

The response of microwave refractometer cavities to atmospheric variations, R. O. Gilmer, R. E. McGavin, and B. R. Bean, Proc. 1964 World Conf. Radio Meteorology and 11th Weather Radar Conf. pp. 244–247 (1964).

Resonance effects of electrostatic oscillations in the ionosphere, J. A. Fejer and W. Calvert, J. Geophys. Res. **69,** 5049–5062 (Dec. 1964).

Observatory report on JILA, L. M. Branscomb, Astron. J. **69,** 700–703 (Nov. 1964).

Laboratory studies of helium ion loss processes of interest in the ionosphere, E. E. Ferguson, F. C. Fehsenfeld, D. B. Dunkin, A. L. Schmeltekopf, and H. I. Schiff, Planetary Space Sci. **12,** 1169–1171 (Dec. 1964).

Complex Lorentz group with a real metric. I. Group structure, A. O. Barut, J. Math Phys. **5,** 1652–1656 (Nov. 1964).

Climatology of elevated super-refractive layers arising from atmospheric subsidence, B. A. Cahoon and L. P. Riggs, Proc. 1964 World Conf. Radio Meteorology and 11th Weather Radar Conf., pp. 52–55 (1964).

Annual report from the National Bureau of Standards, C. E. Moore, Astron, J. **68,** No. 9, 1–3 (Nov. 1964).

Nuclear magnetic moment of Pr^{141} from the hyperfine structure of doubly ionized praseodymium, J. Reader and J. Sugar, Phys. Rev. **137,** No. 4B, B784–B789 (Feb. 22, 1965).

Brightness temperature of the atmosphere using a biexponential model in the 6–45 GHz/s frequency range, E. J. Dutton, B. R. Bean, and E. R. Westwater, Proc. 1964 World Conf. Radio Meteorology and 11th Weather Radar Conf., pp. 212–215 (1964).

Characteristics of dosimeter films processed in phenidone-thiosulfate monobaths, M. Ehrlich, J. Phot. Sci. Engr. **9,** No. 1, 1–9 (Jan.–Feb. 1965).

The uses of oblique ionograms in frequency utilization, K. Davies, Telecommun. J. **31,** 281–287 (Oct. 1964).

Reversal of the diurnal phase variations of GBR (16 kilocycles per second) observed over a path of 720 kilometers, D. D. Crombie and H. L. Rath, J. Geophys. Res. **69,** No. 23, 5023–5027 (Dec. 1, 1964).

Triggered fuse for load protection, J. H. Rogers, Rev. Sci. Instr. **35,** No. 12, 1715 (Dec. 1964).

Safety in the use of liquid hydrogen, D. B. Chelton, Book, Technology and Uses of Liquid Hydrogen, ed. R. B. Scott, W. H. Denton, and C. M. Nicholls, ch. 10, 359–378 (Pergamon Press, Inc., New York, N.Y., 1964).

The calculation of electron energy distribution functions in the ionosphere, L. R. Megill and J. H. Cahn, J. Geophys. Res. **69,** No. 23, 5041–5048 (Dec. 1, 1964).

Solar flares with associated active dark filaments and their relation to 2800-Mc/s radio bursts, M. W. Haurwitz, Astrophys. J. **140,** No. 3, 1236–1246 (Oct. 1, 1964).

Mechanism of inactivation of bacteriophages by metals, N. Yamamoto, C. W. Hiatt, and W. Haller, Biochim. Biophys. Acta **91,** 257–261 (1964).

The performance of lenses made from inhomogeneous glasses, F. W. Rosberry, Appl. Opt. **4,** No. 1, 21–24 (Jan. 1965).

Early strength, flow and dimensional changes obtained on amalgam prepared with a standardized mechanical technic, H. J. Caul, W. S. Crowell, W. D. Kimmel, and G. C. Paffenbarger, J. Am. Dental Assoc. **69,** 742–748 (Dec. 1964).

Photochemical changes in thin layer chromatograms of polycyclic, aromatic hydrocarbons, M. N. Inscoe, Anal. Chem. **36,** No. 13, 2505–2506 (Dec. 1964).

Nucleation characteristics of static liquid nitrogen and liquid hydrogen, J. Hord, R. B. Jacobs, C. C. Robinson, and L. L. Sparks, J. Eng. Power **86,** 485–495 (Oct. 1964).

Degree of metamerism, I. Nimeroff and J. A. Yurow, J. Opt. Soc. Am. **55,** No. 2, 185–190 (Feb. 1965).

Is life possible on other planets? W. R. Bozman, Science and Children **2,** No. 4, 7 (Dec. 1964).

Investigation of plasma boundaries with electromagnetic surface waves, H. W. Wassink and A. J. Estin, J. Appl. Phys. **35,** No. 10, 2795–2800 (Oct. 1964).

Comments on a paper by R. L. Closs, "An experimental investigation of back scattering or radio waves from the equatorial electrojet," R. Cohen and D. T. Farley, Jr., Proc. Phys. Soc. **84,** Pt. 4, No. 540, 619–620 (J. W. Arrowsmith Ltd., London, England 1964).

Changes in living, J. P. Eberhard, Proc. Conf. The Environment of Change, Sterling Forest, Tuxedo, N.Y., June 14–17, 1964, pp. 62–67 (1964).

Metallized polymer film guard rings for dielectric measurements, A. H. Scott, Mater. Res. Std. Tech. Note 5, No. 2, 76–78 (Feb. 1965).

All-glass sorption vacuum trap, F. B. Haller, Rev. Sci. Instr. **35,** No. 10, 1356–1357 (Oct. 1964).

Liquefied gases, handling of; R. B. Scott, Encyclopaedic Dictionary of Physics, p. 1 (Pergamon Press, Inc., New York, N.Y., 1964).

Comparisons of tearing-strength tests for leather, T. J. Carter, J. Am. Leather Chemist Assoc. **LX,** No. 1, 4–14 (Jan. 1965).

Thermal insulation storage, transport and transfer of liquid hydrogen, R. B. Jacobs, Book, Technology and Uses of Liquid Hydrogen, ed. R. B. Scott, W. H. Denton, and

C. M. Nicholls, ch. 4, pp. 106–148 (Pergamon Press, Inc., New York, N.Y., 1964).

Low-temperature apparatus, constructional materials for, R. B. Scott, Encyclopaedic Dictionary of Physics, pp. 1–2 (Pergamon Press, Inc., New York, N.Y., 1964).

The influence of metastable oxygen molecules on ozone and airglow, H. I. Schiff and L. R. Megill, J. Geophys. Res. **69,** No. 23, 5120–5121 (Dec. 1, 1964).

Shape of the magnetospheric boundary under solar wind pressure, R. J. Slutz and J. R. Winkelman, J. Geophys. Res. **69,** No. 23, 4933–4948 (Dec. 1, 1964).

Standards—the foundation of industrial growth, R. D. Stiehler, Industrial Times **BI,** No. 22 (Bombay, India, Nov. 15, 1964).

Hyperfine structure of the $B^2\Sigma^+$ state of CN, H. E. Radford, Phys. Rev. **136,** No. 6A, A1571–A1575 (Dec. 14, 1964).

Research for architecture, J. P. Eberhard, Res. News **II,** No. 1, 10–19 (Jan. 1965).

**Publications for which a price is indicated are available by purchase from the Superintendent of Documents, U.S. Government Printing Office, Washington, D.C., 20402 (foreign postage, one-fourth additional). Reprints from outside journals and the NBS Journal of Research may often be obtained directly from the authors.*

U.S. GOVERNMENT PRINTING OFFICE : 1965

UNIVERSITY MICROFILMS
313 NORTH FIRST STREET
ANN ARBOR, MICHIGAN
SJR-A-OCT

UNITED STATES
GOVERNMENT PRINTING OFFICE
DIVISION OF PUBLIC DOCUMENTS
WASHINGTON, D.C. 20402
OFFICIAL BUSINESS

POSTAGE AND FEES PAID
U.S. GOVERNMENT PRINTING OFFICE

JOURNAL OF RESEARCH of the National Bureau of Standards Vol. 69A, No. 4 July–August 1965
A. Physics and Chemistry

Contents

	Page
Correlation of successive atomic steps in crystals by relaxation mode analysis. A. D. Franklin.	301
Reduction of crystallographic point groups to subgroups by homogeneous stress. H. S. Peiser and J. B. Wachtman, Jr.	309
Effect of hydrostatic pressure on the refractive indices of some solids. R. M. Waxler and C. E. Weir.	325
Crystallization kinetics and polymorphic transformations in polybutene-1. J. Powers, J. D. Hoffman, J. J. Weeks, and F. A. Quinn, Jr.	335
Compliance-time-temperature relationships from indentation measurements on a pure-gum rubber vulcanizate. Frank L. Roth, George W. Bullman, and Lawrence A. Wood.	347
Distribution function of the end-to-end distances of linear polymers with excluded volume effects. Jacob Mazur.	355
An additivity rule for the vapor pressure lowering of aqueous solutions. R. A. Robinson and V. E. Bower.	365
Franck-Condon factors to high vibrational quantum numbers V: O_2 band systems. R. W. Nicholls.	369
An absolute temperature scale from 4 °K to 20 °K determined from measurements with an acoustical thermometer. H. H. Plumb and G. Cataland.	375
Publications of the National Bureau of Standards.	379

Library of Congress Catalog Card Number: 62–37059

For sale by the Superintendent of Documents, U.S. Government Printing Office, Washington, D.C., 20402. Price 70 cents (single copy)
Subscription price: $4 a year; 75 cents additional for foreign mailing.
UNITED STATES GOVERNMENT PRINTING OFFICE, WASHINGTON : 1965